Scanning tunnelling spectroscopy on vortex cores in Bi2Sr2CaCu2O8+[delta souscrit]

Hoogenboom, Bart Wiebren

Université de Genève
Département de physique
de la matière condensée

Faculté des Sciences
Professeur Ø. Fischer

Scanning Tunnelling Spectroscopy on Vortex Cores in $Bi_2Sr_2CaCu_2O_{8+\delta}$

Thèse

présentée à la Faculté des sciences
de l'Université de Genève
pour obtenir le grade de docteur ès sciences,
mention physique

par
Bart Wiebren HOOGENBOOM
de
Bakkeveen (*Pays-Bas*)

Thèse n° 3381

Genève
Imprimerie Raymond Pot
2002

La Faculté des sciences, sur le préavis de Messieurs Ø. FSICHER, professeur ordinaire et directeur de thèse (Département de physique de la matière condensée), B. GIOVANNINI, professeur ordinaire (Département de physique de la matière condensée) et J. AARTS, docteur (Université de Leiden - Pays-Bas), autorise l'impression de la présente thèse, sans exprimer d'opinion sur les propositions qui y sont énoncées.

Genève, le 18 septembre 2002

Thèse - 3381 -

Le Doyen, Jacques **WEBER**

Contents

Résumé en français **1**

1 Introduction **13**

1.1 Superconductivity 13

1.2 Vortices 14

1.3 High-temperature superconductivity 15

1.4 Scanning tunneling microscopy / spectroscopy 18

1.5 Scope of this thesis 20

References 21

2 The Low-Temperature Scanning Tunnelling Microscope **23**

2.1 Introduction 23

2.2 Technical background 24

2.2.1 STM 24

2.2.2 Low temperature, magnetic field, and UHV 25

2.3 STM unit 26

2.3.1 STM head 26

2.3.2 STM control electronics 27

2.3.3 STM unit: outlook 28

2.4 The low-temperature STM 29

2.4.1 General set-up 29

2.4.2 *In situ* sample and tip exchange 31

2.5 The low-temperature STM in UHV 31

2.5.1 General set-up 31

2.5.2 ^{4}He insert 32

2.5.3 STM manipulation platform 37

2.5.4 UHV chamber 37

2.5.5 Vibration isolation . . . 38
2.5.6 System assembly: outlook . . . 38
2.6 Summary . . . 40
Manufacturers and distributors . . . 41
References . . . 43

3 Theoretical Aspects of Tunnelling Spectroscopy 45
3.1 Tunnelling theory . . . 45
3.2 Tunnelling in the STM configuration . . . 47
3.3 Tunnelling spectroscopy . . . 48
References . . . 51

4 Short Lifetime of Sup-Gap Quasiparticles and k-Independent Tunnelling Matrix Elements in High-T_c Superconductors 53
4.1 Introduction . . . 53
4.2 Model . . . 54
4.3 Results . . . 57
4.4 Discussion . . . 60
4.5 Conclusion . . . 63
References . . . 65

5 Sample Preparation and Homogeneity 69
5.1 Introduction . . . 69
5.2 Sample preparation . . . 70
5.3 Results and discussion . . . 71
5.4 Conclusion . . . 74
References . . . 75

6 Shape and Motion of Vortex Cores 77
6.1 Introduction . . . 77
6.2 Experimental details . . . 78
6.3 Results . . . 79
6.3.1 Vortex distribution . . . 79
6.3.2 Vortex shape . . . 81
6.3.3 Vortex motion . . . 81
6.3.4 Temperature dependence . . . 83

6.4 Discussion 83
6.4.1 Experimental considerations 83
6.4.2 Delocalisation 84
6.4.3 Thermal fluctuations versus quantum tunnelling 84
6.5 Conclusion 87
References 89

7 Low-Energy Quasiparticle States in Vortex Cores 91
7.1 Introduction 91
7.2 Results and discussion 92
7.3 Conclusion 96
References 97

8 Linear and Field-Independent Relation between Vortex Core States and Gap 99
8.1 Introduction 99
8.2 Experimental details 100
8.3 Results 100
8.4 Discussion 103
8.5 Conclusion 105
References 107

9 Conclusion and Perspectives 109
References 111

Acknowledgements - Remerciements 113

List of Publications 115

Abbreviations

ARPES	Angle-resolved photoemission spectroscopy
BCS	Bardeen-Cooper-Schrieffer
BSCCO	$Bi_2Sr_2CaCu_2O_{8+\delta}$
DOS	Density of states
HBCCO	$Hg_2Ba_2Ca_2Cu_3O_{10}$
HTS	High-temperature superconductor
HV	High vacuum
LBCO	$La_{2-\delta}Ba_\delta CuO_4$
LDOS	Local density of states
LT	Low temperature
NIS	Normal metal - Insulator - Superconductor
SIS	Superconductor - Insulator - Superconductor
STM	Scanning tunnelling microscope
STS	Scanning tunnelling spectroscopy
UHV	Ultra-high vacuum
VT	Variable temperature
YBCO	$YBa_2Cu_3O_{7-\delta}$
ZBCP	Zero-bias conductance peak
2D	Two-dimensional
3D	Three-dimensional

Résumé:
Etude des coeurs de vortex dans $Bi_2Sr_2CaCu_2O_{8+\delta}$ par spectroscopie à effet tunnel

Introduction

De nombreux phénomènes intéressants en physique de la matière condensée trouvent leur origine dans l'interaction des électrons. Certains d'entre eux étaient déjà connus bien avant qu'on les relie à des comportements électroniques des matériaux. Par exemple, d'anciennes peuplades grecques proche de la ville de Magnesia avaient déjà connaissance de l'existence du magnétisme. C'est seulement au siècle dernier que l'on a pu comprendre que l'origine du magnétisme était liée au moment magnétique des électrons, appelé le "spin" [1]. La mécanique quantique est la théorie à la base de la description du comportement des électrons et de leurs interactions donnant lieu aux différents ordres magnétiques [2].

En 1911, le Néerlandais Kamerlingh Onnes découvrit un autre phénomène macroscopique lié à l'interaction des électrons, appelé la supraconductivité [3]. La supraconductivité – la disparition de toute résistance électrique dans un matériau – provient d'une attraction entre électrons leur permettant de former des paires [4], tandis que le magnétisme est le résultat d'une répulsion entre eux (selon les règles de Hund) [5]. Par conséquent, la supraconductivité et le magnétisme éprouvent des difficultés à coexister.

Il existe cependant certains matériaux, les supraconducteurs de "type II", dans lesquels il peut y avoir simultanément de la supraconductivité et du magnétisme lorsqu'on les plonge dans un champ magnétique. Le champ magnétique extérieur pénètre en effet le supraconducteur en formant des tubes, appelés "vortex" (ou lignes de flux) [6]. La supraconductivité est supprimée dans les coeurs des vortex, et continue à exister en dehors. L'étude de ce phénomène représente une partie importante de cette thèse.

Une autre propriété particulière des électrons est leur capacité de traverser une barrière mince même si leur quantité d'énergie n'est pas suffisante pour la surmonter: c'est l'effet tunnel. Ce phénomène quantique [7] a été largement exploité dans des expériences tunnel à deux électrodes rigides, dans le but d'étudier le mécanisme responsable de la supraconductivité [8].

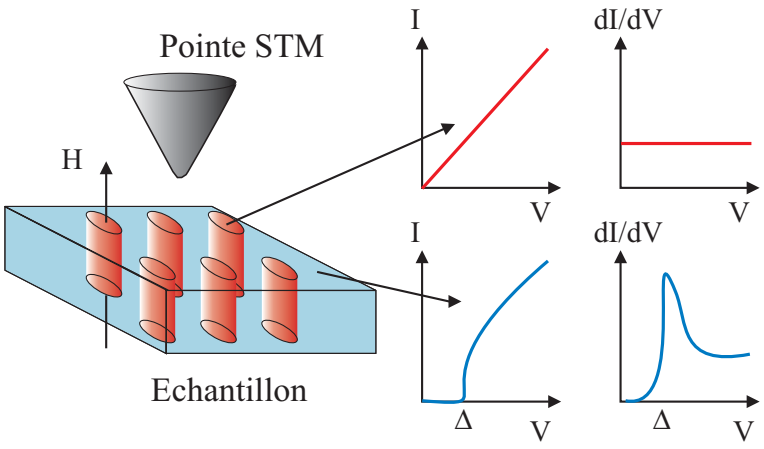

Figure 1: Le STM permet de mesurer les propriétés électroniques à différents endroits sur la surface d'un supraconducteur. Dans le cas d'un supraconducteur de type II, l'application d'un champ magnétique introduit des vortex dans l'échantillon représentés par les tubes. La technique permet de mettre en évidence une densité d'états (DOS) de quasi-particules différente à l'intérieur de l'extérieur des vortex, comme le montrent les spectres $\mathrm{d}I/\mathrm{d}V$.

En 1981, à Zürich, Binnig et Rohrer réalisèrent pour la première fois une jonction tunnel entre une électrode conductrice et une pointe métallique mobile. Dans cette configuration, les électrodes sont séparées par une barrière de vide de seulement quelques Ångströms (Å) d'épaisseur et la pointe peut être positionnée n'importe où sur la surface avec une grande précision. La séparation entre les deux électrodes est régulée en fonction du courant tunnel circulant. L'invention de cet instrument, le microscope à effet tunnel (STM*), leur a valu le prix Nobel de physique en 1986 [9, 10]. Le STM permet non seulement de visualiser directement des atomes, mais également de sonder les propriétés électroniques à la surface avec une très grande résolution en espace et en énergie, c'est la spectroscopie tunnel. Les spectres $\mathrm{d}I/\mathrm{d}V$ (dérivée du courant tunnel par rapport à la tension entre la pointe et la surface) représentent la densité d'états des quasi-particules dans un matériau.

Le STM, ainsi qu'un instrument dérivé le microscope à effet atomique (AFM) [11], sont devenus des instruments clés dans les nanosciences. Ils permettent notamment d'étudier et de manipuler la matière (y-compris les tissus vivants) à une échelle nanométrique.

La figure 1 illustre une des applications du STM à savoir la spectroscopie des coeurs de vortex dans les supraconducteurs. Le STM peut sonder les propriétés électroniques d'un matériau très localement et mettre en évidence les différences entre un coeur de vortex et l'état supraconducteur. Ceci fut réalisé pour la première fois par Hess et ses collaborateurs [12], qui visualisèrent de cette manière le réseau de vortex d'Abrikosov dans le supraconducteur $NbSe_2$.

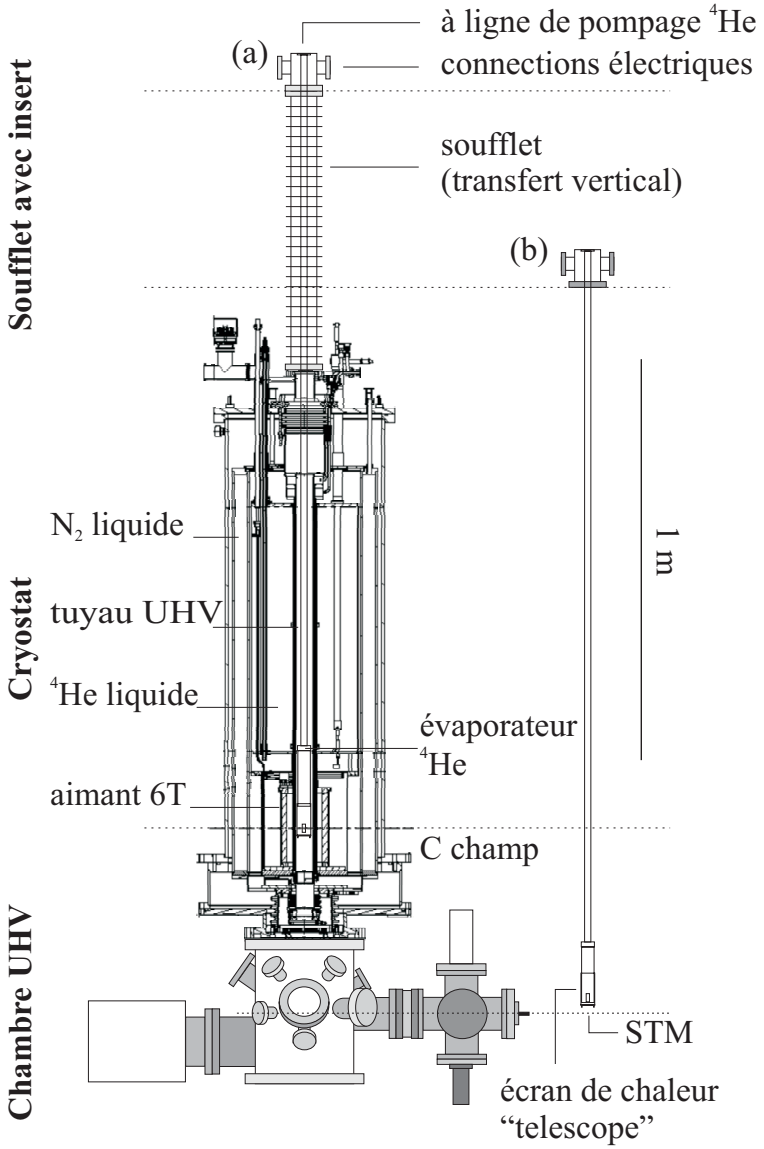

Figure 2: Schéma du nouveau système à basse température. Le cryostat se charge par le bas, depuis la chambre UHV. La canne rigide à laquelle est rattachée le STM se trouve au centre du cryostat. Elle est supportée par un soufflet avec moteur vertical qui permet de déplacer le STM de la position de mesure (a) vers la position de manipulation (b). L'espace UHV s'étend de la chambre UHV en bas jusqu'aux connections électriques en haut de la canne. Un capillaire (pas dessiné) relie l'évaporateur sur la canne au bain d'hélium principal.

Le STM à basse température

La spectroscopie tunnel a une résolution en énergie qui est limitée par la température. Ainsi, il est nécessaire d'effectuer des mesures à basse température (de l'ordre de 1 Kelvin) pour étudier l'attraction entre les électrons et les excitations dans un coeur de vortex.

D'autre part, le STM ne donne accès qu'aux caractéristiques de la surface du matériau étudié et non de l'intérieur du solide. Pour les matériaux étudiés dans cette thèse, la préparation de la surface revêt une importance particulière. Il faut en effet éviter que la surface soit contaminée ou dégradée. La technique pour travailler avec une surface propre, qui n'a pas été exposée à l'air et à l'humidité, est de "cliver" les échantillons dans une chambre à ultra-haut vide (UHV).

Les mesures présentées dans cette thèse ont été réalisées avec un STM à basse température (refroidi dans un gaz d'échange), avec possibilité de clivage *in-situ*. Ce système a été développé par Renner et ses collaborateurs [13, 14] et a été récemment adapté pour permettre l'échange d'échantillons et de pointes sans ouvrir la chambre UHV. De plus, le bruit des mesures a été amélioré avec une nouvelle électronique de contrôle.

Parallèlement, le lancement d'un nouveau système à basse température a démarré (voir chapitre 2) sur la base d'un STM développé dans le cadre de la thèse de Kugler [15, 16]. Ce système purement UHV permet des mesures à température variable (sans gaz d'échange) avec possibilité d'appliquer un champ magnétique. L'amélioration principale de ce nouveau système réside dans la simplicité du design de la canne qui supporte le STM dans le cryostat. Elle est rigide, ce qui élimine tout bruit lié au mouvement des fils des connections électriques *in-situ*, et ce qui évite des problèmes dus au mécanisme de translation fonctionnant dans l'UHV.

Les principaux éléments de ce nouveau système ont été testés et sont prêts à être assemblés: (i) La canne avec une température de base de < 1.5 K. (ii) La plate-forme de manipulation permettant le clivage et l'échange d'échantillons, ainsi que l'échange des pointes. (iii) La chambre UHV dans laquelle – sans étuvage – une pression de $1{\cdot}10^{-9}$ mbar a été obtenue. Finalement, le cryostat qui a été livré récemment est en train d'être testé.

Les supraconducteurs à haute température

L'étude de supraconducteurs ne se fait pas seulement à basse température pour des raisons de résolution en énergie, mais par le simple fait que la supraconductivité n'a lieu que bien au-dessous de la température ambiante. Les températures de transition (T_c) des supraconducteurs dits conventionnels sont typiquement de l'ordre de quelques Kelvin. En revanche, Bednorz et Müller [17] on découvert en 1986 une nouvelle classe de supraconducteurs, appelés les supraconducteurs à haute température (HTS's). Leur structure est basée sur des plans CuO_2 et leur températures de transition peuvent atteindre 134 K (à pression ambiante).

Bien que les propriétés des supraconducteurs conventionnels soient bien comprises dans

*Les abréviations utilisées dans ce résumé proviennent de la terminologie anglaise selon la liste donnée au début de ce travail.

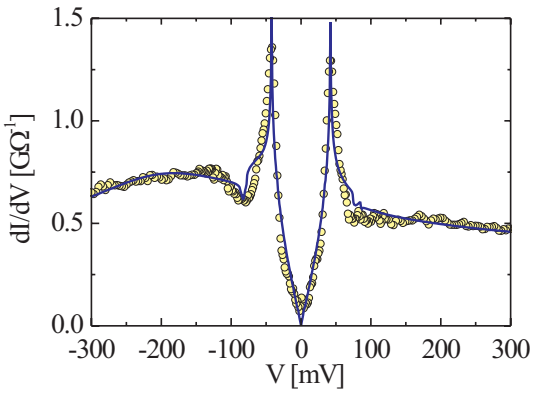

Figure 3: Comparaison entre un spectre obtenu sur BSCCO à basse température (cercles), et un spectre calculé avec un modèle qui décrit l'interaction des quasi-particules selon un mode collectif [23] (trait continu).

le cadre de la théorie BCS (de Bardeen, Cooper, et Schrieffer) [18], le mécanisme microscopique à la base de la supraconductivité des HTS's est moins clair. Les HTS's ont en commun avec les supraconducteurs conventionnels l'existence d'une attraction entre les électrons, mais dans les HTS's cette attraction dépend de la direction dans l'espace réciproque selon une symétrie $d_{x^2-y^2}$. D'autres particularités peuvent être consultées par exemple dans la référence [19].

Les mesures réalisées dans cette thèse ont été faites sur un des HTS's, le matériau $Bi_2Sr_2CaCu_2O_{8+\delta}$ (BSCCO). Il se trouve que les spectres tunnel obtenus sur BSCCO sont assez similaires à ce qui est prédit par la théorie BCS, à condition qu'on admette une symétrie $d_{x^2-y^2}$ pour le paramètre d'ordre (attraction qui mène à la formation de paires d'électrons), et que l'énergie liée à cette attraction (le gap Δ) soit grande.

Les spectres obtenus montrent des pics de cohérence à des énergies de $\pm\Delta$ [20]. L'analyse réalisée dans le chapitre 4 démontre cependant qu'il y a encore des déviations importantes de la théorie BCS. La présence d'un pic dans la densité d'états normale, appelé "singularité van Hove" [21, 22], n'est pas observée directement dans nos spectres. Cette singularité est presque complètement effacée pour des échantillons avec des dopages d'oxygène différents, contrairement aux pics de cohérence qui sont bien présents. Seule une large bosse reste présente dans le fond des spectres, qui se déplace vers des énergies de liaison plus grandes pour des échantillons sous-dopés. Ce résultat implique que le temps de vie des quasi-particules au-dessus du gap est très court, contrairement au temps de vie qui détermine la largeur des pics de cohérence.

La singularité van Hove peut être supprimée en utilisant une interaction des quasi-particules selon un mode collectif, de façon similaire au cas de l'interaction de quasi-particules avec un phonon dans la théorie du couplage fort [24, 25]. Ceci a été testé numériquement en utilisant le modèle de Norman et ses collaborateurs [23]. La comparaison des spectres expérimentaux obtenus avec les simulations démontre en effet une bonne correspondance pour un élément matrice de tunnel constant (pour chaque vecteur d'onde dans la zone Brillouin).

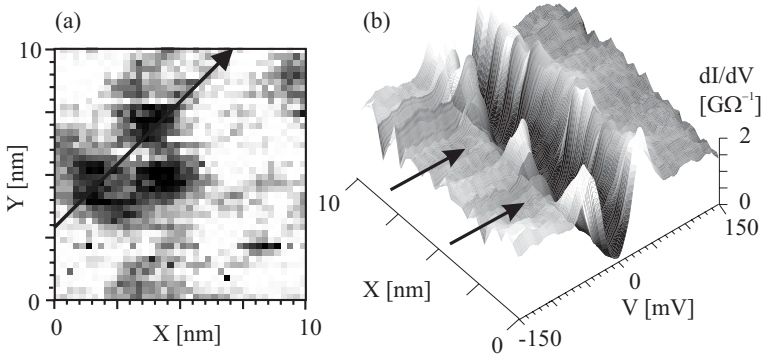

Figure 4: (a) Image d'un coeur de vortex qui est formé de plusieurs éléments séparés. ($B = 6$ T, $T = 4.2$ K.) (b) Les spectres enregistrés le long d'une trace [flèche en (a)] montrent que les pics de cohérence liés à l'état supraconducteur disparaissent au coeur des vortex [flèches en (b)] et remontent entre ces zones .

Comme le STM permet de mesurer les propriétés électroniques à la surface d'un supraconducteur, il est intéressant de mesurer si ces propriétés peuvent changer d'un endroit à l'autre. En fait, ceci est souvent le cas dans le BSCCO [26–32]. et il s'avère que ces inhomogénéités (désordre) peuvent être une signature d'une séparation de phases dans les HTS's, comme cela a été prédit par plusieurs théories [33–35].

Il est alors important de vérifier si un certain degré d'inhomogénéité est intrinsèque à la supraconductivité à haute température. On démontre dans le chapitre 5 que ceci n'est pas le cas, à moins que ces inhomogénéités varient sur une échelle de temps plus petite que la seconde. Pour des échantillons de BSCCO légèrement surdopés et bien oxygénés, les propriétés électroniques (statiques) sont homogènes sur des distances de plusieurs centaines d'Å.

Les coeurs de vortex dans $Bi_2Sr_2CaCu_2O_{8+\delta}$

Il y a plusieurs propriétés des HTS's qui rendent l'étude des vortex dans ces matériaux extrêmement intéressante. Premièrement, la symétrie $d_{x^2-y^2}$ du paramètre d'ordre implique qu'on peut s'attendre à des vortex ayant une forme liée à cette symétrie: ils devraient être plutôt carrés, alors qu'ils sont ronds dans les supraconducteurs conventionnels. Deuxièmement, les vortex peuvent être facilement ancrés dans les HTS's à cause des inhomogénéités ou des défauts présents [36]. Dans de tels cas, – malgré leur répulsion mutuelle – les vortex ne s'arrangent pas nécessairement dans un réseau régulier.

Au cours de l'étude de la forme intrinsèque des coeurs de vortex dans BSCCO, on a observé des formes très irrégulières (chapitre 6). Les coeurs de vortex semblent souvent être formés de plusieurs éléments séparés. La présence de sites d'ancrage semble expliquer ces formes irrégulières. Tant qu'un vortex n'a pas trouvé sa position d'équilibre – souvent dans un site d'ancrage – il continue à osciller entre plusieurs sites d'ancrage voisins. Comme le STM a une résolution limitée en échelle de temps, l'imagerie donne

une position moyenne des coeurs de vortex, ce qui explique pourquoi ils semblent occuper plusieurs sites simultanément.

Un phénomène de mouvement de vortex similaire a été observé sur des distances plus grandes (de l'ordre d'une centaine d'Å). En effet, une fois qu'on a mis le champ magnétique, il faut attendre plusieurs heures avant que les vortex aient trouvé leur position d'équilibre, spécialement dans le cas d'échantillons refroidis en champ nul. Ainsi, en enregistrant des images successives, il a été possible d'étudier les mouvements de vortex dans BSCCO et, comme décrit précédemment, on a pu observer des coeurs de vortex qui – avant de se déplacer complètement d'une position à l'autre – semblaient être divisés entre deux sites d'ancrage.

L'analyse détaillée de nos mesures en fonction de la température suggère fortement que le mouvement des coeurs de vortex est de caractère quantique. En effet, les coeurs de vortex passent *à travers* les barrières de potentiel des sites d'ancrage par effet tunnel et non par fluctuations thermiques [37, 38].

Les chapitres 7 et 8 de cette thèse sont consacrés à l'étude de la nature électronique des coeurs de vortex. Dans les supraconducteurs conventionnels, la suppression du paramètre d'ordre dans un coeur de vortex crée un puits de potentiel pour les quasi-particules à basse énergie. On y trouve des états de quasi-particules localisés [39]. Dans les HTS's, ce puits de potentiel n'est pas complètement fermé, à cause de la présence de noeuds dans le paramètre d'ordre $d_{x^2-y^2}$. On s'attend alors à des états qui s'étendent dans l'espace

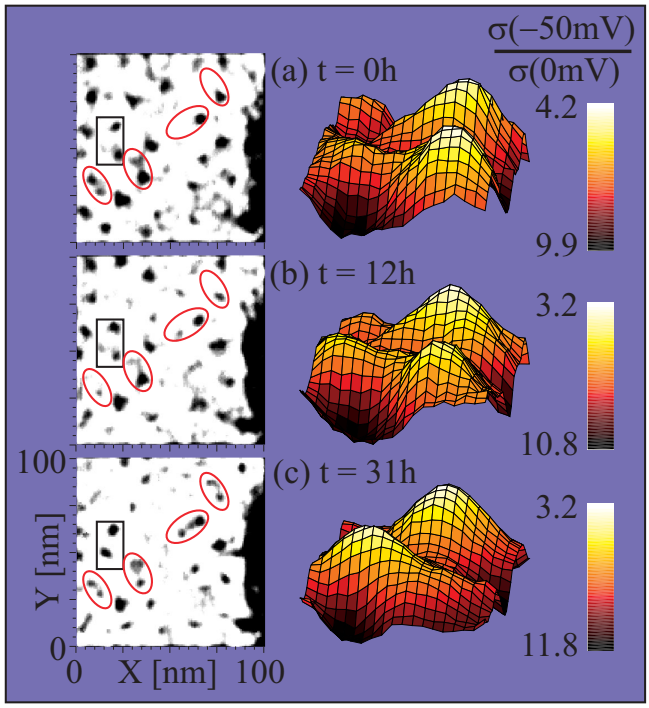

Figure 5: Séquence d'images montrant les mouvements des coeurs de vortex, $B = 6$ T, $T = 4.2$ K. (a) t = 0; (b) t = 12h; (c) t = 31h. A gauche: représentation bi-dimensionnelle (échelle de gris constante). A droite: représentation tri-dimensionnelle de la région délimitée par des rectangles dans les images de gauche. Le coeur de vortex semble être divisé en (b), avant qu'il ne bouge complètement d'une position (a) à l'autre (c).

réel, ce qui doit se caractériser par un large pic au niveau Fermi dans la densité d'états des quasi-particules [40–42].

Contrairement à ces prédictions théoriques (basées sur la théorie BCS), nos mesures démontrent pour la première fois l'existence d'états de vortex discrets (séparés en énergie) dans BSCCO [43, 44]. Ces états apparaissent comme des épaules faibles dans le gap.

A première vue, les états de coeur dans BSCCO semblent bien différents de ceux dans $YBa_2Cu_3O_{7-\delta}$ (YBCO) [45]. Dans YBCO ils sont très prononcés et existent même dans l'état supraconducteur à champ nul sous forme de petites épaules. En revanche, si l'on mesure l'énergie des états de coeur en fonction de la valeur du gap supraconducteur (déterminé à partir des énergies des pics de cohérence), on trouve un comportement très similaire dans BSCCO et YBCO. Ceci indique que ces états de coeur sont une caractéristique générique des HTS's.

Une autre conclusion importante de ce travail est que la dépendance de l'énergie des états de coeur en fonction de la valeur gap est plutôt linéaire, indépendamment du champ magnétique [46]. Ceci est très différent des états de coeurs de vortex dans les

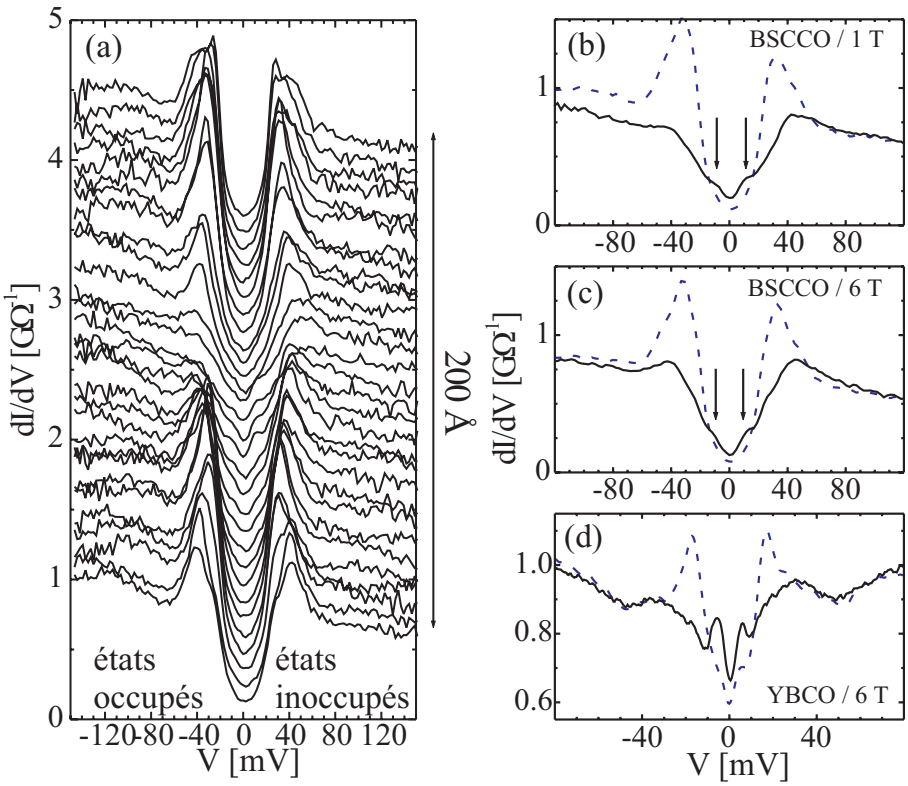

Figure 6: (a) Spectres à 1 T le long une trace de 200 Å. Le coeur de vortex se trouve au centre de la trace. Les spectres sont translatés à l'axe vertical pour des raisons de clarté. V est la tension sur l'échantillon. (b) Spectre moyenné au centre du coeur de vortex (ligne continue), spectre de l'état supraconducteur à proximité (traitillé). Les états de coeur sont indiqués par les flèches. (c) Spectre d'un autre coeur de vortex, à 6 T. (d) Spectre pour un coeur de vortex dans YBCO, à 6 T. L'échelle horizontale a été ajustée afin d'obtenir la même taille de gap pour les trois graphiques.

supraconducteurs conventionnels qui ont une dépendance respective parabolique. Ces résultats (voir les figures 6 et 7) fournissent d'importantes indications pour comprendre la nature électronique des coeurs de vortex. Une explication d'un tel comportement peut être trouvée dans la présence du pseudogap dans les coeurs de vortex [47, 48]. Le pseudogap correspond au gap qu'on observe *au-dessus* de la température de transition, et est une autre caractéristique des HTS's non explicable dans la théorie BCS.

Conclusions et perspectives

Ce travail de thèse à contribué au développement d'un nouveau STM à basse température sous UHV et champ magnétique. L'analyse des spectres obtenus sur BSCCO a montré un temps de vie extrêmement court des quasi-particules au-dessus du gap supraconducteur. Grâce à des longs recuits sous oxygène, on a obtenu des échantillons qui sont homogènes sur des distances de plusieurs centaines d'Å. Des mesures en champ magnétique ont mis en évidence les mouvements des coeurs de vortex à courte distance, probablement par effet tunnel à travers des barrières de potentiel entre sites d'ancrage. Enfin, on a observé pour la première fois des états de coeur de vortex dans BSCCO. Ces états sont indépendants du champ magnétique entre 1 et 6 T, et leur énergie a une dépendance linéaire en fonction du gap supraconducteur.

Un travail de recherche soulève souvent plus de questions qu'elle n'en résoud. Le développement d'un nouveau STM a déjà stimulé de nouvelles idées, mentionnées dans le chapitre 2. En ce qui concerne les résultats sur BSCCO, il sera important de faire

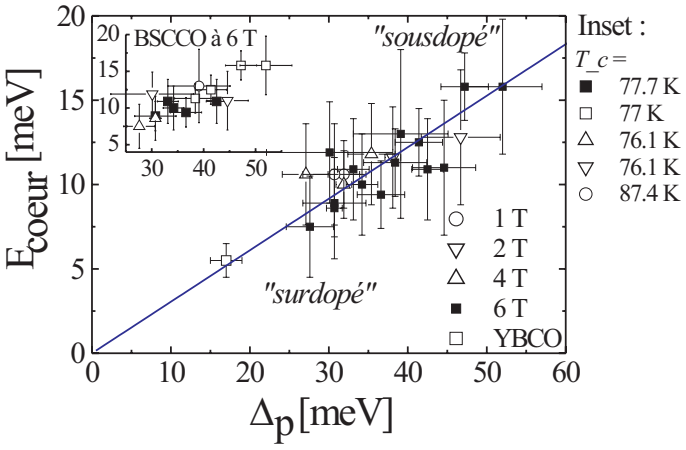

Figure 7: Energie des états de coeur de vortex E_{coeur} en fonction de la valeur du gap supraconducteur (énergie des pics de cohérence) Δ_p. Les données correspondent à des coeurs de vortex pour des champs magnétiques compris entre 1 et 6 T et pour différents échantillons de BSCCO. La valeur obtenue à partir des données sur YBCO à été ajoutée ($\Delta_p = 17$ meV). Une régression linéaire par l'origine de tous les points mesurés sur BSCCO donne une pente de 0.30. Les données pour BSCCO à 6 T sont reportées également en insert pour les différents échantillons mesurés (T_c).

une étude plus systématique de l'(in)homogénéité électronique. La nature du mouvement des coeurs de vortex peut être étudiée à des températures au-dessous de 1 K, pour bien établir son caractère quantique. On pourrait aussi s'imaginer des expériences sur le mouvement des vortex entre des sites d'ancrage créés artificiellement avec le STM. Enfin, l'origine des états de coeur de vortex dans les HTS's est encore loin d'être clarifiée.

References

[1] C. Kittel, *Introduction to Solid State Physics*, 6th ed. (J. Wiley, New York, 1986).

[2] R. P. Feynman, R. B. Leighton, and M. Sands, *Lectures on Physics* (Addison-Wesley, Reading, Massachusetts, 1965), Vol. III.

[3] H. Kamerlingh Onnes, Leiden Comm., **120b, 122b, 124c** (1911).

[4] L. N. Cooper, Phys. Rev. **104**, 1189 (1956).

[5] N. W. Ashcroft and N. D. Mermin, *Solid State Physics* (Saunders College, Philadelphia, 1976).

[6] A. A. Abrikosov, Zh. Eksperim. i Teor. Fiz **32**, 1442 (1957).

[7] S. Gasiorowicz, *Quantum Physics* (John Wiley & Sons, Inc., Singapore, 1974).

[8] I. Giaever, Phys. Rev. Lett. **5**, 147 (1960).

[9] G. Binnig, H. Rohrer, Ch. Gerber, and E. Weibel, Phys. Rev. Lett. **49**, 57 (1982).

[10] G. Binnig and H. Rohrer, Helv. Phys. Acta **55**, 726 (1982).

[11] G. Binnig, C. F. Quate, and Ch. Gerber, Phys. Rev. Lett. **56**, 930 (1986).

[12] H. F. Hess, R. B. Robinson, R. C. Dynes, J. M. Valles, and J. V. Waszczak, Phys. Rev. Lett. **62**, 214 (1989).

[13] A. D. Kent, Ch. Renner, Ph. Niedermann, J.-G. Bosch, and Ø. Fischer, Ultramicroscopy **42-44**, 1632 (1992).

[14] Ch. Renner, Ph.D. thesis, University of Geneva, n° 2620 (1993).

[15] M. Kugler, Ch. Renner, V. Mikheev, G. Batey, and Ø. Fischer, Rev. Sci. Instrum. **71**, 1475 (2000).

[16] M. Kugler, Ph.D. thesis, University of Geneva, n° 3158 (2000).

[17] J. G. Bednorz and K. A. Müller, Z. Phys. B **64**, 189 (1986).

[18] J. Bardeen, L. N. Cooper, and J. R. Schrieffer, Phys. Rev. **108**, 1175 (1957).

[19] J. Orenstein and A. J. Millis, Science **288**, 468 (2000).

[20] Ch. Renner, B. Revaz, J.-Y. Genoud, K. Kadowaki, and Ø. Fischer, Phys. Rev. Lett. **80**, 149 (1998).

[21] O. K. Andersen, O. Jepsen, A. I. Liechtenstein, and I. I. Mazin, Phys. Rev. B **49**, 4145 (1994).

[22] O. K. Andersen, A. I. Liechtenstein, O. Jepsen, and F. Paulsen, J. Phys. Chem. Solids **56**, 1573 (1995).

[23] M. R. Norman and H. Ding, Phys. Rev. B **57**, R11089 (1998).

[24] J. R. Schrieffer, *Theory of Superconductivity* (W. A. Benjamin, New York, 1964).

[25] R. D. Parks, *Superconductivity* (Marcel Dekker, New York, 1969), Vol. 1.

[26] J.-X. Liu, J.-C. Wan, A.-M. Goldman, Y. C. Chang, and P. Z. Jiang, Phys. Rev. Lett. **67**, 2195 (1991).

[27] A. Chang, Z. Y. Rong, Y. M. Ivanchenko, F. Lu, and E. L. Wolf, Phys. Rev. B **46**, 5692 (1992).

[28] T. Cren, D. Roditchev, W. Sacks, J. Klein, J.-B. Moussy, C. Deville-Cavellin, and M. Laguës, Phys. Rev. Lett. **84**, 147 (2000).

[29] T. Cren, D. Roditchev, W. Sacks, and J. Klein, Europhys. Lett. **54**, 84 (2001).

[30] C. Howald, P. Fournier, and A. Kapitulnik, Phys. Rev. B **64**, 100504 (2001).

[31] S. H. Pan, J. P. O'Neal, R. L. Badzey, C. Chamon, H. Ding, J. R. Engelbrecht, Z. Wang, H. Eisaki, S. Uchida, A. K. Gupta, K.-W. Ng, E. W. Hudson, K. M. Lang, and J. C. Davis, Nature **413**, 282 (2001).

[32] K. M. Lang, V. Madhavan, J. E. Hoffman, E. W. Hudson, H. Eisaki, and S. Uchida J. C. Davis, Nature **415**, 412 (2002).

[33] V. J. Emery, S. A. Kivelson, and H. Q. Lin, Phys. Rev. Lett. **64**, 475 (1990).

[34] Y. N. Ovchinnikov, S. A. Wolf, and V. Z. Kresin, Phys. Rev. B **63**, 64524 (2001).

[35] S. Chakravarty, R. B. Laughlin, D. K. Morr, and C. Nayak, Phys. Rev. B **63**, 94503 (2001).

[36] G. Blatter, M. V. Feigel'man, V. B. Geschkenbein, A. I. Larkin, and V. M. Vinokur, Rev. Mod. Phys. **66**, 1125 (1994), and references therein.

[37] B. W. Hoogenboom, M. Kugler, B. Revaz, I. Maggio-Aprile, Ø. Fischer, and Ch. Renner, Phys. Rev. B **62**, 9179 (2000).

[38] B. W. Hoogenboom, Ch. Renner, I. Maggio-Aprile, and Ø. Fischer, in *Vortices in Unconventional Superconductors and Superfluids*, Vol. 132 of *Series in Solid-State Science*, edited by R. P. Huebener, N. Schophohl, and G. E. Volovik (Springer, Berlin Heidelberg, 2002), pp. 269–282.

[39] C. Caroli, P. G. de Gennes, and J. Matricon, Phys. Lett. **9**, 307 (1964).

[40] Y. Wang and A. H. MacDonald, Phys. Rev. B **52**, R3876 (1995).

[41] M. Franz and Z. Tešanović, Phys. Rev. Lett. **80**, 4763 (1998).

[42] K. Yasui and T. Kita, Phys. Rev. Lett. **83**, 4168 (1999).

[43] B. W. Hoogenboom, Ch. Renner, B. Revaz, I. Maggio-Aprile, and Ø. Fischer, Physica C **332**, 440 (2000).

[44] S. H. Pan, E. W. Hudson, A. K. Gupta, K.-W. Ng, H. Eisaki, S. Uchida, and J. C. Davis, Phys. Rev. Lett. **85**, 1536 (2000).

[45] I. Maggio-Aprile, Ch. Renner, A. Erb, E. Walker, and Ø. Fischer, Phys. Rev. Lett. **75**, 2754 (1995).

[46] B. W. Hoogenboom, K. Kadowaki, B. Revaz, M. Li, Ch. Renner, and Ø. Fischer, Phys. Rev. Lett. **87**, 267001 (2001).

[47] C. Berthod and B. Giovannini, Phys. Rev. Lett. **87**, 277002 (2001).

[48] J.-X. Zhu and C. S. Ting, Phys. Rev. Lett. **87**, 147002 (2001).

Chapter 1

Introduction

1.1 Superconductivity

In 1911, Kamerlingh Onnes discovered superconductivity, in Leiden (the Netherlands) [1]. He and his collaborators found that the resistance of metals like mercury, lead and tin dropped to zero below a certain transition temperature (T_c), implying infinite or super conductivity. These metals can thus transport energy without loss.

Though after Onnes' discovery several phenomenological theories were developed, it took more than four decades before (in 1957) physicists were able to produce a consistent microscopic picture of a superconductor. This picture is now known as BCS theory, after its creators Bardeen, Cooper and Schrieffer [2].

One of the key features of this theory, is the formation of electron pairs, so-called Cooper pairs [3]. In a metal, electrons move through a lattice formed by the positive ions. Because of its negative charge, an electron will slightly attract its surrounding positive ions, creating a positive zone. This positive zone can attract an other electron. So under certain circumstances electrons can be attracted to each other, forming pairs in spite of their mutual Coulomb repulsion. As shown in Fig. 1.1, the pair formation is a dynamic process, implying that two electrons are never exactly on the same spot. Generally, the interaction of electrons with the lattice is described in terms of phonons (lattice vibrations).

Electrons are fermions, implying that they can never occupy the same state (the Pauli principle). However, when the electrons form pairs, these pairs can show bosonic behaviour, all occupying the same, macroscopic ground state at low temperature. The point is now that processes leading to resistance only affect individual electrons [4]. When the electrons are bound in pairs, these processes can only perturb the electrons if they provide an energy larger than the energy (2Δ) which binds the electrons together.

Stated in more quantum-mechanical terms, it is energetically favourable for the pairs to be in the same ground state, similar to a Bose-Einstein condensate [5]. Resistance is the result of scattering of electrons or pairs to excited states. And again this is only possible if these scattering processes involve energies larger than the energy gain related to all pairs being in the ground state. As long as this is not the case, the electrons move without any resistance [6].

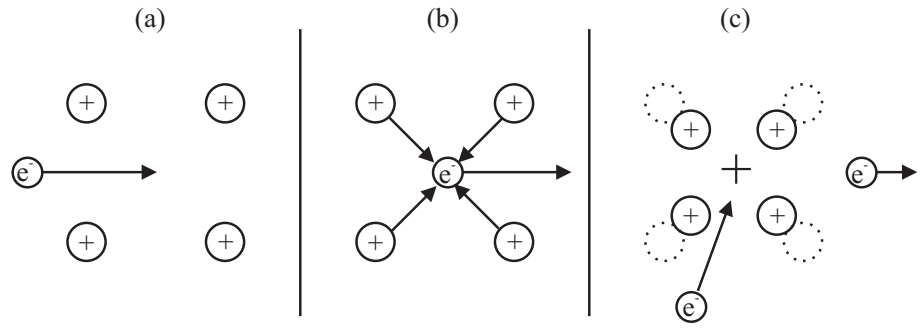

Figure 1.1: (a) An electron (e^-) passing through a lattice of ions (+) with positive charge. (b) Since the electron has a negative charge, it attracts the ions. (c) With some delay, the ions respond to this attraction, creating a zone which is more positive than the surroundings. As a result, an other electron can be attracted. The two electrons move thus as a pair.

1.2 Vortices

One way of breaking Cooper pairs in a superconductor, is by applying a magnetic field. The effect of a magnetic field is to align the spins of the electrons, as if the electrons were compass needles. It is thus possible to flip the spin around. Since the formation of a Cooper pair requires electrons of opposite spin (at least in most superconductors actually kown), a strong magnetic field will destroy superconductivity.

On the other hand, as long as the magnetic field is not too strong, the superconductor can expel the magnetic field. If one applies a magnetic field to a superconductor, currents are created. These currents are such that they create a magnetic field opposing to the applied field. Since there is no resistance, these currents continue to provide this opposing field, exactly cancelling the applied magnetic field. More surprisingly, a superconductor also expels a magnetic field when the field is applied before the material becomes superconducting (before the material is cooled down to below the transition temperature). This is called perfect diamagnetism, or the Meissner effect [7].

The mutual exclusion of magnetism and superconductivity is entirely valid for a large class of superconductors, type I superconductors. In a second class of superconductors, of type II, it is energetically favourable to have local changes from a superconducting zone into a magnetic zone. In more physical terms: there is a negative surface energy associated with the interface between two such zones, resulting from the balance of the local energy gain of condensation of Cooper pairs and the energy cost of creating supercurrents screening the magnetic field.

It follows from this negative surface energy that an external magnetic field can partly penetrate a superconductor, as long as the field is large enough not to be completely expelled, and not so large that all superconductivity is destroyed. A magnetic field penetrates a type II superconductor in the form of tubes, called vortices. In the interior of these tubes, there are no pairs, and around them supercurrents flow, screening the superconducting region from the local magnetic field [8].

Since the vortices repel each other, they will maximise the average distance to their neighbours by forming a lattice. However, if superconductivity is already suppressed in some small zones, it is more attractive for the magnetic field to penetrate just there.

This can perturb the ordered vortex lattice, and is called pinning [6].

In the interior of a vortex – the vortex core – superconductivity is suppressed, and Cooper pairs are broken. In the surrounding superconducting region the electrons are bound in pairs. As a result, for energies below the pair binding energy per electron (Δ), excited states only exist in the vortex cores. Since the elementary excitations in a superconductor are so-called quasiparticle excitations, one speaks of localised quasiparticle states (or excitations).

In other words, vortex cores represent potential wells for low-energy quasiparticles. Because of the dimensions of the vortex cores and the quasiparticle wavelengths, these potential wells are quantum-mechanical [10]. Therefore only discrete quasiparticle states are allowed in the vortex core, though their energy spacing can be rather small (below experimental resolution). The existence of these localised core states was first derived by Caroli, de Gennes, and Matricon [11], and later confirmed experimentally [12, 13].

1.3 High-temperature superconductivity

In conventional superconductors, one should not think of Cooper pairs as pairs in real space. That is, the electrons of a pair are bound, but the size of a Cooper pair is much larger than the distance between the pairs. In fact, in the volume occupied by one Cooper pair (of two electrons) about one million other paired electrons wander around [14].

Furthermore, the pair binding energy (2Δ) is relatively small (typically of the order of a meV). Therefore, if one heats up the superconductor starting at absolute zero ($-273\ ^{o}$C), the additional thermal energy will soon be sufficient to break the pairs. As a result, conventional superconductors have transition temperatures of typically some degrees above zero temperature.

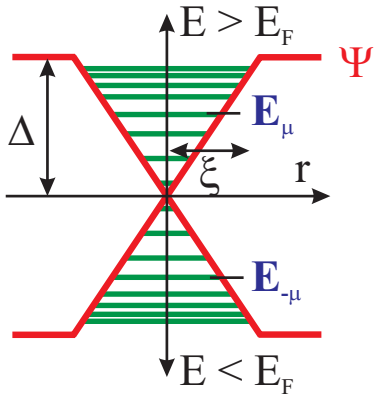

Figure 1.2: Schematic representation of quasiparticle excitations localised in the vortex core in a BCS superconductor (for a more rigorous picture the reader is referred to numerical calculations of Gygi and Schlüter [9]). The order parameter Ψ goes to zero in the vortex core, over a characteristic distance ξ. Inside the vortex core one can find quasiparticle states, the lowest of which correspond to $E_\mu \sim \mu\Delta^2/E_F$ ($\mu = \pm 1/2,\ \pm 3/2,\ \pm 5/2,\ ...$), smaller than the gap Δ. The continuum of quasiparticle states above the gap is not shown in this picture.

The only way to reach such temperatures is by using a cooling liquid [15]: liquid helium, which boils at $-269\ ^oC$ (at atmospheric pressure). Liquid helium is not that easy to use, and most unfortunately, it is very expensive. Another cooling liquid is nitrogen, with a boiling point of $-196\ ^oC$. In contrast to helium, nitrogen is easily obtained (it makes up 80% of air), and cheap.

Spectacularly high transition temperatures (though still far below room temperature) have been found in so-called high-temperature superconductors (HTSs). This new class of superconductors was discovered by Bednorz and Müller [16], in 1986. They studied $La_{2-\delta}Ba_\delta CuO_4$ (LBCO), a material superconducting below a transition temperature of $-235\ ^oC$. Not only did this represent a jump of 12 degrees in the world record of superconducting transition temperature, it also revealed that there was a new (and complicated!) class of materials, called copper-oxides or cuprates or HTSs, with a large potential for superconductivity. Soon after LBCO, $YBa_2Cu_3O_{7-\delta}$ (YBCO) followed, with a transition temperature of about $-181\ ^oC$, and thereafter similar compounds like $Bi_2Sr_2CaCu_2O_{8+\delta}$ (BSCCO) were made. The world record transition temperature (at ambient pressure) is now $-139\ ^oC$, for $Hg_2Ba_2Ca_2Cu_3O_{10}$ (HBCCO). Many of these transition temperatures are well above the boiling point of nitrogen.

As a common feature the HTSs all contain copper-oxide (CuO_2) planes in their structure, which are believed to be mainly responsible for superconductivity. However, their superconducting properties also depend very critically on the ions in the layers neighbouring the CuO_2 planes. To give an example, removing one neighbouring oxygen atom per ten CuO_2 blocks dramatically reduces the transition temperature, or leaves a material which is totally insulating [6]. This insulating behaviour can be explained by the large Coulomb interaction on the Cu atoms. When all Cu sites are occupied by one charge carrier, the Coulomb repulsion between these carriers makes it very difficult for them to move [17]. By adding oxygen atoms, one can add remove some electrons from the CuO_2 planes, allowing the remaining charge carriers to move more easily.

As in conventional (low-temperature) superconductors, in HTSs electron pairs play an important role in causing superconductivity. However, they appear to be different from the Cooper pairs discussed before. First of all, it seems a miracle that they are formed at such high temperatures. According to older theories describing the electron-phonon

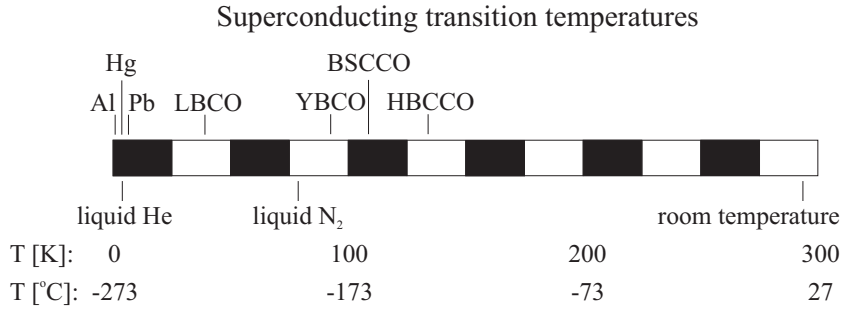

Figure 1.3: A temperature scale, both in Kelvin and degrees Celsius, with the transition temperatures of some conventional (aluminium – Al, mercury – Hg, led – Pb) and high-temperature (LBCO, YBCO, BSCCO, HBCCO) superconductors. The temperatures at which helium (He) and nitrogen (N_2) liquefy, are indicated as well.

interaction (see section 1.1), the thermal energy would prevent pair formation far below the actual transition temperatures of HTSs. Such high transition temperatures were thus thought to be impossible.

Many physicists have ideas about the reason for the attraction between the electrons in HTSs, but there is no common explanation which they agree upon. The electron-phonon interaction may play a role, but in a more sophisticated way than in conventional superconductors [18]. It is also well possible that the Coulomb repulsion between the electrons delays their movements, creating pairs [4]. This has been modelled using theoretical entities called slave bosons. The same Coulomb repulsion causes the undoped CuO_2 planes (one charge carrier per Cu atom) to be magnetically ordered: neighbouring electron spins are aligned in opposite directions. The transition from superconductivity to such a magnetic order can also be described as a rotation in a five-dimensional space, in SO(5) theory [19].

As can be expected because of the high transition temperatures, the paired electrons are much closer one to the other in HTSs than in conventional superconductors. The size of the pairs (the coherence length ξ) is thus very small. Correspondingly the energy binding the pairs together is large, in fact even larger than expected based on the transition temperature.

There is another peculiarity in the way electrons in HTSs attract each other: their attraction depends on direction. The electrons appear more attractive in certain directions, and not attractive at all from others. The exact symmetry of the attraction is a four-fold one (as far as the amplitude is concerned), called $d_{x^2-y^2}$ [20].

Strange enough, many of the mysteries concerning HTSs are related to the *non*-superconducting state. Experiments show the presence of an energy gap – suggesting the

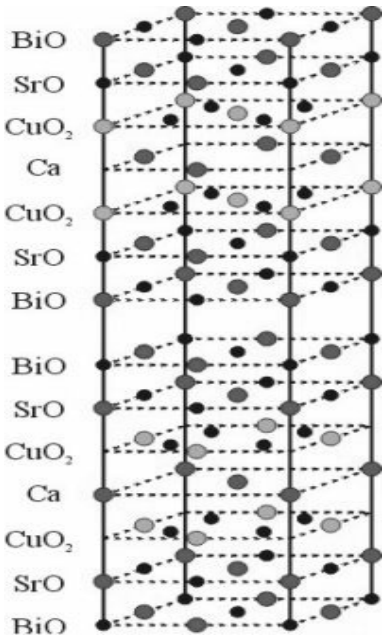

Figure 1.4: The structure of BSCCO, with semiconducting BiO layers, insulating SrO layers, and superconducting CuO_2 layers. The material can be cleaved (exposing a clean surface) between two neighbouring BiO layers.

presence of electron pairs – well *above* the superconducting transition temperature [21]. This may be an indication of the presence of pairs with incoherent phases [22].

So far, theories and experimental results on HTSs [23] are too numerous and too diverse to allow to speak of a proper understanding of these materials. However, HTSs give rise to many specific problems (related to vortex cores, for example), which can be tackled by different experimental methods. The experimental methods discussed in the following section are scanning tunneling microscopy and spectroscopy. They can be used to shed light on several interesting properties of superconductors.

1.4 Scanning tunneling microscopy / spectroscopy

The laws of quantum mechanics allow a particle to tunnel through an energy barrier, even if its energy is not sufficient to overcome the barrier in a classical way [10]. This is equally true if one brings a sharp metallic tip close to the surface of a conducting material. In that case, the particles of importance are electrons, the energy barrier is formed by the free space between the tip and the sample (of the order of some eV). When the distance between tip and sample is small enough, typically smaller than a nanometre, electrons can tunnel from tip to sample or vice versa. A voltage V applied between tip and sample thus leads to a tunnel current I_t, which is strongly dependent on the tip-sample distance.

Using piezo-electric motors, the tip position with respect to the sample can be controlled with a precision smaller than the interatomic distances. The tip can thus move over the surface, and with a feedback loop the tip-sample distance can be kept such that the tunnel current remains constant: the tip follows the contours of the sample surface when it is scanning over the surface. This was first achieved by Binnig and Rohrer, from Zürich, with an instrument called a scanning tunnelling microscope (STM) [24, 25]. Their most spectacular result was the direct imaging of individual atoms on the surface.

Apart from its capacities to map the topography of a (conducting) surface, the STM can also be used to obtain information on the local electronic properties of a sample, with a technique called scanning tunnelling spectroscopy (STS) [26]. For fixed tip and sample positions, one can sweep the voltage V and record the resulting tunnel current I_t.

It can be shown (see Chapter 3 and e.g. Ref. [27]) that the derivative $\mathrm{d}I/\mathrm{d}V(V)$ of such a tunnel spectrum corresponds to the local quasiparticle density of states (DOS) of the sample, on condition that the tip behaves like a metal with free electrons.

Some of the most convincing experimental data in support of BCS theory in fact came from tunnelling experiments with fixed electrodes [28]. Junctions with a metallic and a superconducting side lead to spectra giving the quasiparticle DOS of the superconductor. At low temperature, this DOS is practically zero for voltages smaller than Δ, since all electrons are paired, and the Cooper pairs cannot tunnel into the metallic side of the junction . However, if the voltage become larger than Δ/e (e is the electron charge), it provides enough energy to break pairs, and to create electrons (or holes) capable of tunnelling into the metal. This lead to sharp peaks in the $\mathrm{d}I/\mathrm{d}V(V)$ spectra at voltages of $\pm\Delta/e$

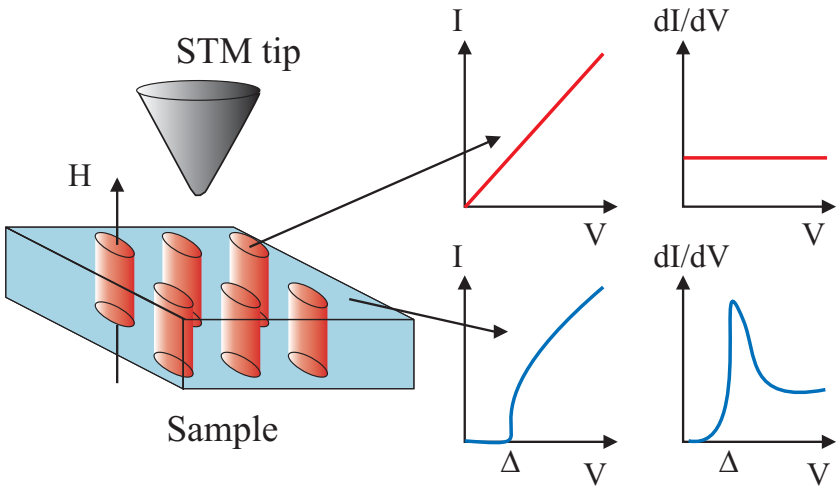

Figure 1.5: With the STM one can scan over the surface of a superconductor, leading to spectra with pronounced coherence peaks at $\pm\Delta$. If one applies a magnetic field H, one may find vortices, of which the cores give spectra without energy gap and coherence peaks. A map of vortex core is obtained by measuring the $\mathrm{d}I/\mathrm{d}V$ at the energy at which the difference between superconducting and vortex core spectra is most important.

An important advantage of the STM with respect to other measurement techniques, is its ability to measure the DOS *locally*. Remember the vortices discussed in section 1.2. In their cores superconductivity is suppressed, so one does not expect to see a gapped spectrum in a vortex core. Around the core, however, the spectra do show an energy gap, due to pairing of electrons in the superconducting state. Low-energy quasiparticles ($< \Delta$) only exist in the vortex cores. This difference in quasiparticle DOS can be used to map vortex cores, as has been done on several superconductors. STM vortex images have been obtained on $NbSe_2$ [12, 13], YBCO [29], $LuNi_2B_2C$ [30], BSCCO [31], YNi_2B_2C [32], $CeRu_2$ [33], and MgB_2 [34]. These images provide information on how the vortices are distributed (lattice or not), what they look like, and how they move.

There are many other experimental techniques giving direct images of vortices, techniques which are sensitive to the local variation of the magnetic field. Such techniques are Bitter decoration [35, 36], magnetic force microscopy [37–39], scanning hall-probe microscopy [40], scanning SQUID microscopy [41, 42], and Lorentz microscopy [43]. None of these, however, gives direct information about the quasiparticle states in vortex cores, in the way it can be obtained by STM.

What are these states like? For HTSs the answer is still not totally clear. Since the pairing attraction between the electrons drops to zero along certain directions, low-energy quasiparticles do exist outside the vortex cores as well. Furthermore, the cores in HTSs are much smaller than in conventional superconductors (corresponding to the small size of the pairs, in fact). The vortex cores are even more interesting because they give deeply frozen, low-temperature information about the non-superconducting state. And for HTSs there is not only a lack of understanding about their superconductivity, but the non-superconducting state above the transition temperature still presents many mysteries as well.

1.5 Scope of this thesis

The main aim of the work described in this thesis has been to get a better understanding of the electronic nature of vortex cores in HTSs. That is, to describe and to understand the properties of quasiparticles in vortex cores, and relate them to more general properties of HTSs.

The first requirement for these kinds of studies is an STM working at low temperatures and (preferentially) ultra-high vacuum. The next chapter describes such an STM. It is also a report on much work on improving existing equipment, and on designing a new low-temperature STM.

After a more mathematical introduction (chapter 3) on the theory behind tunnelling spectroscopy, chapter 4 contains the results of numerical simulations used for the analysis of tunnelling measurements on BSCCO, at zero field. This analysis is important to understand the role of e.g. tunnelling matrix elements, which may perturb the tunnelling spectra.

When trying to map vortex cores, one obtains information about their shape, the way they are distributed, and the way they move. This has led to a detailed study of the shape and motion of vortex cores, as described in chapter 6.

Finally, the chapters 7 and 8 are entirely devoted to the quasiparticle excitations in vortex cores in HTSs. After a characterisation of vortex core spectra, the dependence of so-called vortex core states on hole doping and on the magnetic field is established and discussed.

References

[1] H. Kamerlingh Onnes, Leiden Comm., **120b, 122b, 124c** (1911).

[2] J. Bardeen, L. N. Cooper, and J. R. Schrieffer, Phys. Rev. **108**, 1175 (1957).

[3] L. N. Cooper, Phys. Rev. **104**, 1189 (1956).

[4] S. Doniach and E. H. Sondheimer, *Green's Functions for Solid State Physicists*, 2nd. ed. (Imperial College Press, London, 1998).

[5] R. P. Feynman, R. B. Leighton, and M. Sands, *Lectures on Physics* (Addison-Wesley, Reading, Massachusetts, 1965), Vol. III.

[6] M. Tinkham, *Introduction to Superconductivity*, 2nd. ed. (McGraw-Hill, New York, 1996).

[7] W. Meissner and R. Ochsenfeld, Naturwissenschaften **21**, 787 (1933).

[8] A. A. Abrikosov, Zh. Eksperim. i Teor. Fiz **32**, 1442 (1957).

[9] F. Gygi and M. Schluter, Phys. Rev. B **43**, 7609 (1991).

[10] S. Gasiorowicz, *Quantum Physics* (John Wiley & Sons, Inc., Singapore, 1974).

[11] C. Caroli, P. G. de Gennes, and J. Matricon, Phys. Lett. **9**, 307 (1964).

[12] H. F. Hess, R. B. Robinson, R. C. Dynes, J. M. Valles, and J. V. Waszczak, Phys. Rev. Lett. **62**, 214 (1989).

[13] Ch. Renner, A. D. Kent, Ph. Niedermann, Ø. Fischer, and F. Lévy, Phys. Rev. Lett. **67**, 1650 (1991).

[14] C. Kittel, *Introduction to Solid State Physics*, 6th ed. (J. Wiley, New York, 1986).

[15] R. R. Conte, *Éléments de cryogénie* (Masson et C^{ie}, Paris, 1970).

[16] J. G. Bednorz and K. A. Müller, Z. Phys. B **64**, 189 (1986).

[17] J. Zaanen, G. A. Sawatzky, and J. W. Allen, Phys. Rev. Lett. **55**, 418 (1985).

[18] G. M. Zhao, M. B. Hunt, H. Keller, and K. A. Müller, Nature **385**, 236 (1997).

[19] S.-C. Zhang, Science **275**, 1089 (1997).

[20] D. J. Van Harlingen, Rev. Mod. Phys. **67**, 515 (1995).

[21] Ch. Renner, B. Revaz, J.-Y. Genoud, K. Kadowaki, and Ø. Fischer, Phys. Rev. Lett. **80**, 149 (1998).

[22] V. J. Emery and S. A. Kivelson, Nature **374**, 434 (1995).

[23] J. Orenstein and A. J. Millis, Science **288**, 468 (2000).

[24] G. Binnig, H. Rohrer, Ch. Gerber, and E. Weibel, Phys. Rev. Lett. **49**, 57 (1982).

[25] G. Binnig and H. Rohrer, Helv. Phys. Acta **55**, 726 (1982).

[26] H.-J. Güntherodt and R. Wiesendanger, *Scanning Tunneling Microscopy* (Springer-Verlag, Berlin, 1993), Vol. I-III.

[27] E. L. Wolf, *Principles of Electron Tunneling Spectroscopy* (Oxford University Press, New York, 1985).

[28] I. Giaever, Phys. Rev. Lett. **5**, 147 (1960).

[29] I. Maggio-Aprile, Ch. Renner, A. Erb, E. Walker, and Ø. Fischer, Phys. Rev. Lett. **75**, 2754 (1995).

[30] Y. DeWilde, M. Iavarone, U. Welp, V. Metlushko, A. E. Koshelev, I. Aranson, G. W. Crabtree, and P. C. Canfield, Phys. Rev. Lett. **78**, 4273 (1997).

[31] Ch. Renner, B. Revaz, K. Kadowaki, I. Maggio-Aprile, and Ø. Fischer, Phys. Rev. Lett. **80**, 3606 (1998).

[32] H. Sakata, M. Oosawa, K. Matsuba, N. Nishida, H. Takeya, and K. Hirata, Phys. Rev. Lett. **84**, 1583 (2000).

[33] H. Sakata, N. Nishida, M. Hedo, K. Sakurai, Y. Inada, Y. Onuki, E. Yamamoto, and Y. Haga, J. Phys. Soc. Jpn. **69**, 1970 (2000).

[34] M. R. Eskildsen, M. Kugler, S. Tanaka, J. Jun, S. M. Kazakov, J. Karpinski, and Ø. Fischer, preprint.

[35] U. Essmann and H. Träuble, J. Sci. Instrum. **43**, 344 (1966).

[36] U. Essmann and H. Träuble, Phys. Lett. **24A**, 526 (1967).

[37] P. Rice and J. Moreland, IEEE Trans. Magn. **27**, 5181 (1991).

[38] A. Moser, H. J. Hug, I. Parashikov, B. Stiefel, O. Fritz, H. Thomas, A. Baratoff, H.-J. Güntherodt, and P. Chaudari, Phys. Rev. Lett. **74**, 1847 (1995).

[39] C. W. Yuan, Z. Zheng, and J. N. Eckstein, J. Vac. Sci. Technol. **14**, 1210 (1996).

[40] A. M. Chang, H. L. Kao H. D. Hallen, H. F. Hess, J. Kwo, A. Sudbø, and T. Y. Chang, Europhys. Lett. **20**, 645 (1992).

[41] F. P. Rogers, BS/MS thesis, MIT (1993).

[42] L. N. Vu, M. S. Wistrom, and D. J. van Harlingen, Appl. Phys. Lett. **63**, 1693 (1993).

[43] A. Tonomura, J. Low Temp. Phys. **105**, 1091 (1996), and references therein.

Chapter 2

The Low-Temperature Scanning Tunnelling Microscope

2.1 Introduction

Operating a scanning tunneling microscope (STM) means moving a sharp tip at a few Ångström (Å) distance over a surface without touching. This evidently requires a high level of precision and stability. As will be demonstrated in section 3.2, a variation in tip-sample distance of 1 Å already changes the tunnel current by an order of magnitude. The distance (z) between the tip and the sample surface should therefore be controlled within a fraction of an Å. Equal precision is required for the lateral (xy) tip position in order to allow direct visualisation of atoms at the surface.

Besides its abilities to image surfaces with atomic resolution, the STM is a unique tool for the local investigation of electronic structure by scanning tunnelling spectroscopy (STS). The energy resolution of such a tunnelling experiment is limited to $k_B T \approx 0.1 \cdot T$ meV, with the temperature T in Kelvin. Since many interesting electronic interactions (e.g. superconductivity) have an energy scale of the order of 1 meV, and moreover only occur at low temperatures, one should be able to operate the STM at and below the temperature of liquid helium, i.e. 4.2 K. Further complications arise if one wants to study electronic properties as a function of temperature, requiring an STM not only operating at low-temperature (LT), but also at variable-temperature (VT). The study of vortices, as explained in chapter 1, requires the presence of a relatively high magnetic field. For vortices in high-T_c superconductors this field should be typically some Tesla.

For the interpretation of tunnelling spectra (section 3.3), the possibility to vary parameters that do not change the tunnel junction itself, is extremely useful as well. For instance, features of the spectra that change with temperature or magnetic field, can be directly related to the electronic properties of the surface, and not to any phenomenon resulting from the tunnelling process. Therefore, the variation of temperature and magnetic field not only creates opportunities to study phenomena under different external conditions, but is also an important tool for the comprehension of tunnelling spectra.

Scanning tunnelling microscopy is a surface technique. This will always lead to the question if measurements represent the bulk properties of a material, or only those of its

surface. Especially spectroscopic measurements are extremely sensitive to contamination of the surface. In order to be able to link the surface properties measured with the STM to properties of the bulk material, the surface should thus be kept perfectly clean. For the materials discussed in this thesis, it implies working ultra-high vacuum (UHV) or LT high vacuum (HV).

Therefore, the ideal STM for our experiments should have a high resolution in position and energy, be operating at variable temperatures and magnetic fields, and preferentially in a UHV environment. Though each of these requirements as such corresponds to standard techniques in present-day laboratories, the combination is still far from evident.

In this chapter, I will give an overview of different ways of meeting these combined requirements, followed by a discussion of the STM unit used for this thesis, and of two systems in which this unit has been implemented for operation at low temperature, in magnetic fields, and UHV. The developments worked out in the framework of this thesis will be highlighted.

2.2 Technical background

2.2.1 STM

The key element of the tunnel junction in an STM is the tip, which in principle should be atomically sharp. Tips with apex radii down to some nanometres (nm) are produced by chemical etching of tungsten, gold, iridium or platinum-iridium wires, see e.g. Ref. [1]. Though thus obtained apex radii are larger than the atoms on the surface, these tips are generally sufficiently sharp to obtain atomic resolution.

Apart from a sharp tip, an STM basically consists of two elements. The first is a scanner, which moves the tip over the sample surface with sub-Å resolution. The second is a transport mechanism for coarse motion, to bring the sample within the range of the (fine motion) scanner.

The controlled, fine motion of the tip over the surface is obtained using standard piezo-electric scanner tubes [2]. (In general, a piezo-electric element converts a voltage into a mechanical deformation, or vice versa.) Such a tube has an outer electrode divided into four equal quadrants parallel to the tube axis. When voltages are applied to two adjacent outside quadrants, the tube bends, providing lateral (xy) motion. The vertical (z) displacement is obtained by applying a voltage to the common inner electrode (with respect to the outer electrodes).

Since the (lateral and vertical) scan range of the scanner is usually limited, a coarse motion device is needed to bring the tip-sample distance down to some tenths of a micrometer. This problem has been attacked in various ways. Manual or step-motorised movements using screws, springs, and levers [3–5] are simple but not very compact solutions. Other solutions are based again on piezo-electric materials. Piezos can be used as small feet, moving one by one like the feet of a louse [6], or in an inchworm design [7, 8]. Other designs are based on a slip-stick or inertial motor, walking like a (Besocke) beetle [9] or in a horizontal [10] or vertical [11, 12] slider.

For vibration isolation the STM is usually separated from its environment by low-pass filters. The design of the STM should then be such to push up its resonance frequencies as high as possible. The STM itself will thus act as a high-pass filter. To obtain such an STM, it should be designed as small and rigid as possible. An other, complementary way to obtain a stable instrument is designing the instrument as a damped oscillator (again with low resonance frequency to act as a low-pass filter). Damping can be provided by e.g. Eddy currents.

2.2.2 Low temperature, magnetic field, and UHV

Following the requirements outlined in section 2.1, the STM should be operating at variable temperatures and magnetic fields. This implies that the mechanism to move the STM should be rather insensitive to thermal contractions and other changes of material properties as a function of temperature. Furthermore, the STM should be brought into good thermal contact with a cold point (generally in a liquid helium cryostat). The thermal contact can be achieved either by an exchange gas or by mechanical contact. For practical purposes, it is preferential to have a short cool-down and warm-up time of the whole system, and limited thermal drift of the tip with respect to the sample. The presence of a magnetic field further limits the choice of materials and imposes a non-magnetic motion mechanism.

In order to obtain clean surfaces, samples should be treated or cleaved in UHV before being placed in the STM, without being exposed to air. The STM should thus be operating in UHV, made of entirely UHV-compatible materials, and allow *in-situ* sample exchange. To avoid opening the vacuum system each time the tip needs to be changed, it is very practical to also have the possibility of *in-situ* tip exchange. In general, a UHV environment asks for several additional precautions concerning the cleanliness of materials. It is to be advised to design a system such that only the most elementary tasks are performed *in-situ*, to avoid that the system should be opened in case of failure of a specific function of the system. An alternative for UHV cleaving is cleaving at low temperature in high vacuum [13]. At low temperature, surface reactions are considerably delayed, and by cryogenic pumping a vacuum of 10^{-9}-10^{-10} mbar can be obtained, provided that the system is properly sealed. Though LT-cleaving avoids many of the complications of UHV, it is not that easy to design, and in general does not allow optical inspection of the cleaved surface.

Since the choice of commercially available STMs operating at LT and UHV is at present extremely limited [14, 15], most of the existing STMs fulfilling some and exceptionally all of the requirements indicated above [13, 16–29], are still home-built systems. The LT-STM in exchange gas of Ref. [16] (see section 2.4), developed in Geneva, was used for the measurements described in the next chapters, and – as part of this thesis – adapted to allow *in-situ* tip exchange, and loading of samples and tips via a load-lock. The more recent Geneva-based ^{3}He STM in a bottom-loading cryostat [29], was the starting-point for the design of a new UHV LT STM described in section 2.5. In the latter design, emphasis was laid on simplifying the UHV part of the system and on improving stability and resolution. The latter systems share the basic design of a vertical inertial slider STM developed by Christophe Renner in Geneva [11, 12], as described in section 2.3.

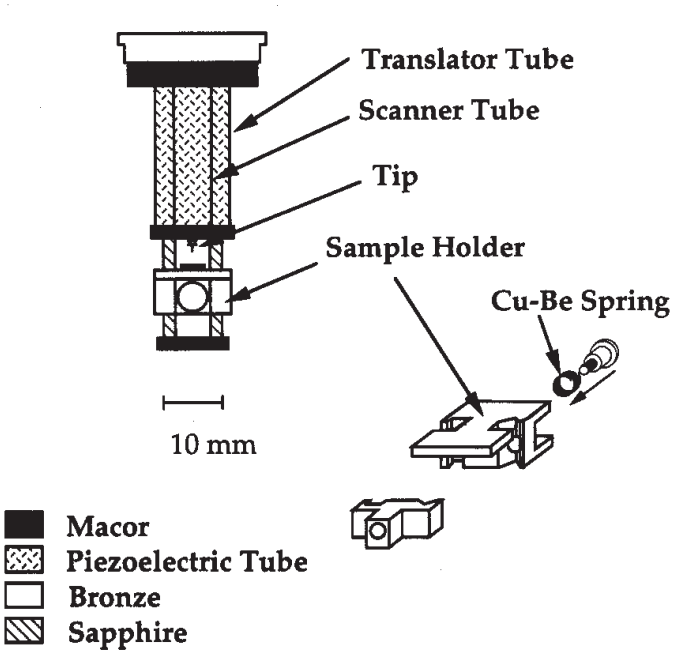

Figure 2.1: Schematic view of the STM head showing the concentric tube design with two piezo-electric tubes. The outer (translator) tube supports two sapphire rails with the sample holder and the inner tube serves as the scanner. The sample holder is shown in the lower part of the figure. (Fig. from Ref [16].)

2.3 STM unit

2.3.1 STM head

The Renner STM design has been described in detail elsewhere [11, 12, 16, 30]. In the following I will briefly recall its basic operation principles. A schematic view of the STM head is given in Fig. 2.1.

The STM consists of two concentric piezo-electric tubes. The inner tube serves as the scanner, as described in the previous section. The outer tube is the translator, driving the vertical inertial motor. The operation of the STM is explained in Fig. 2.2. Two essential features of the vertical inertial motor are: (i) The clamping force of the spring, fixing the caro-bronze sample holder onto the sapphire rails. This clamping force is needed to counter gravitation. (ii) A cycloid driving signal for the translator. This gives the highest acceleration of the sapphire rails.

The STM is very compact, and because the scanner and the translator are closely fixed together, it is intrinsically stable. All materials used for the STM are compatible with UHV and low temperature, and are non-magnetic. As vibration isolation, suspension to a low-resonance frequency (~ 1 Hz) spring is sufficient. The wires descending along the spring provide some damping.

For operation in a system without exchange gas, the materials of the STM head need to have good thermal conductance. For this reason the macor pieces in Fig. 2.1 were

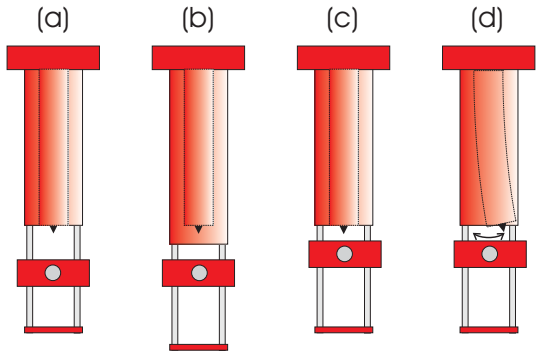

Figure 2.2: Operation of the STM. The outer tube, the translator, drives the coarse, inertial motion of the sample towards the tip. (a) The STM with the sample far away from the tip. (b) The translator tube is *rapidly* elongated. As a consequence of its inertial mass, the sample holder (spring-loaded on the sapphire rails) does not follow the translator motion, and moves up with respect to the translator. (c) The translator tube is *slowly* contracted to its original length. Since the acceleration is low, the sample holder follows the motion of the translator. The translator is now ready for the next step, following (a)-(c). (d) Once the sample is within the range of the scanner tube, the latter moves the tip over the sample with sub-Å resolution.

replaced by caro-bronze. Details on the choice of materials can be found in Ref. [31].

For the system described in section 2.5, the length of the piezo tubes was reduced from 1" to 0.5". This has the effect of decreasing the scanner deformation per applied voltage (thus reducing the effect of noise of the voltage signals, but also reducing the scan range), and pushing up further the resonance frequencies of the STM. The resulting STM head is shown in Fig. 2.6.

2.3.2 STM control electronics

The signals to drive the STM are provided by home-built control electronics, which has been developed in our group over the last 15 years. The general concept is based on an analogue, negative integral feedback loop. The feedback controls the vertical position of the tip during the scan over the sample surface, in order to keep the tunnel current constant. A schematic diagram of the electronic control system is shown in Fig. 2.3. The main parts of the circuit are a current pre-amplifier, a current control unit with adjustable gain, a logarithmic amplifier, an integrator, and a high voltage amplifier (with 3 mV top-top noise for a maximum signal of ± 150 V).

As a part of this thesis, the feedback electronics was redesigned on printed circuit boards, to reduce the amount of soldering needed. Special care was taken to avoid ground loops. The noise on the outputs of the different electronic modules was typically reduced by a factor ~ 5.

The coarse and fine approach of the sample towards the tip, the scanning (xy) of the tip, the sample bias, and the data acquisition are computer controlled. The most recent version of the data acquisition program is based on LABVIEW.* Differential spectra

*The data acquisition program was entirely rewritten by A. A. Manuel, to replace the older TURBO PASCAL version.

$\mathrm{d}I/\mathrm{d}V$ are recorded using a small modulation voltage on top of the sample bias and a lock-in technique.

2.3.3 STM unit: outlook

The most recent versions of our control electronics and data acquisition system, in combination with the piezo-electric scanner, allow a spatial resolution of the order of a picometre (0.01 Å). Since the actual resolution of our instrument is about an order of magnitude higher, there is still space for improvement of the STM itself. The stability of the whole system including the cryostat, as well as the wiring of the STM, will deserve attention in section 2.5. Here I concentrate on several possible improvements of the STM head, both related to its practical use and its stability.

As it was already noted in the early days of the STM development in Geneva [30], in the actual STM design it is rather difficult to position the sample in x-y once it is transferred onto the STM head. An xy table driven by piezo-electric actuators would be an ideal solution for lateral coarse positioning of the sample. Although our group has undertaken several efforts in this direction, it is still not evident how to implement an xy table in the small space on the vertical slider, without making the latter too heavy, and without an undesired coupling between vertical and lateral coarse motion.

The slider itself has proven to be effective during many experiments. It has also shown its limitations, however, in the sense that its motion is not always as reproducible as one would wish, especially at low temperature. One of the reasons for this is the rotational degree of freedom between both sides of the slider (i.e. in between which the sapphire

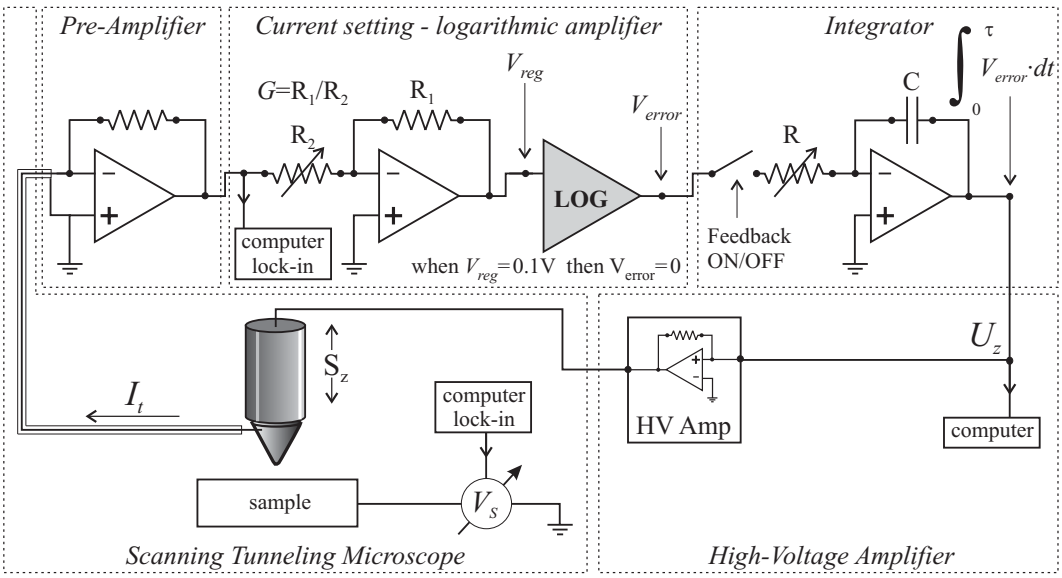

Figure 2.3: Schematic block diagram of the analogue feedback regulation circuitry. The pre-amplifier transforms the tunnel current I_t into a voltage, which is regulated at 0.1 V by adjusting the gain G. When $V_{reg} = 0.1$ V, the error signal of the logarithmic amplifier is zero. Any non-zero error signal is integrated before going via the high-voltage amplifier to the scanner z piezo.

rails are clamped). During tip and sample exchange both sides can slightly rotate with respect to the other, changing the friction force, and thus changing the vertical step size.

In principle the STM head should become more stable when the scanner length is reduced: this leads to a higher resonance frequency, and a smaller response to noise of the high-voltage modules driving the scanner. It also means a reduction of the scan range, however. How this works out at low temperatures will become clear when the UHV LT STM (equipped with a shorter scanner, see section 2.3) is fully operating. Another possibility to reduce noise is better screening of the tunnel current in the STM head.

Some of the considerations given above have led to the development of a new STM head, different from the Renner design described above. A prototype is being constructed during the editing of this thesis. The new design keeps some of the successful characteristics of the Renner design: (i) A caro-bronze slider inertially moving along sapphire rails; (ii) the size, the new design is even smaller, with a diameter of 19 mm and a length of 25 mm. However, instead of moving the sample holder, the coarse approach is done by moving the scanner. Since the sample holder does not move, the implementation of an xy table will be easier. The slider on which the scanner is mounted, is made of one piece, avoiding the rotational degrees of freedom of the slider in the Renner design. The scanner itself is only $1/8" \times 1/4"$.

2.4 The low-temperature STM

2.4.1 General set-up

The Renner STM described in the previous section is sufficiently small to fit into the bore of a superconducting magnet. The general set-up to combine sample cleaving in UHV with a low-temperature STM in high magnetic field is shown in Fig. 2.4 [16].

The system consists of a UHV chamber (typically 10^{-9} mbar) on top of a ^{4}He bath cryostat with a superconducting magnet. When the STM is in the manipulation position (in the UHV chamber), the valve to the cryostat is closed. On the manipulation table, samples can be cleaved and put onto the STM. The STM is then moved towards a viewport, where the sample is brought close to the STM tip (as seen by an optical microscope with $40\times$ magnification).

Thereafter, the valve to the (turbo) pump is closed and the valve to the cryostat opened, and the STM is let down into a tube with typically 10^{-2} mbar very pure helium exchange gas. In measurement position, below in the centre of the magnet, the STM is only suspended on a long spring. The base temperature is 4.2 K, though lower temperatures can be reached by pumping on the helium bath (resulting in high helium consumption). The temperature gradient in the cryostat can be used for variable temperature measurements, but this has the drawbacks of eliminating the vibration isolation due to the spring suspension (when the STM is pulled up), and of rising the STM out of the centre of the superconducting magnet. Variable temperature measurements at a magnetic field are thus not possible. The whole system stands on a concrete basement separated from the building to reduce vibrations. Further details of this system as it was at the start of this thesis, can be found in Ref. [16, 30].

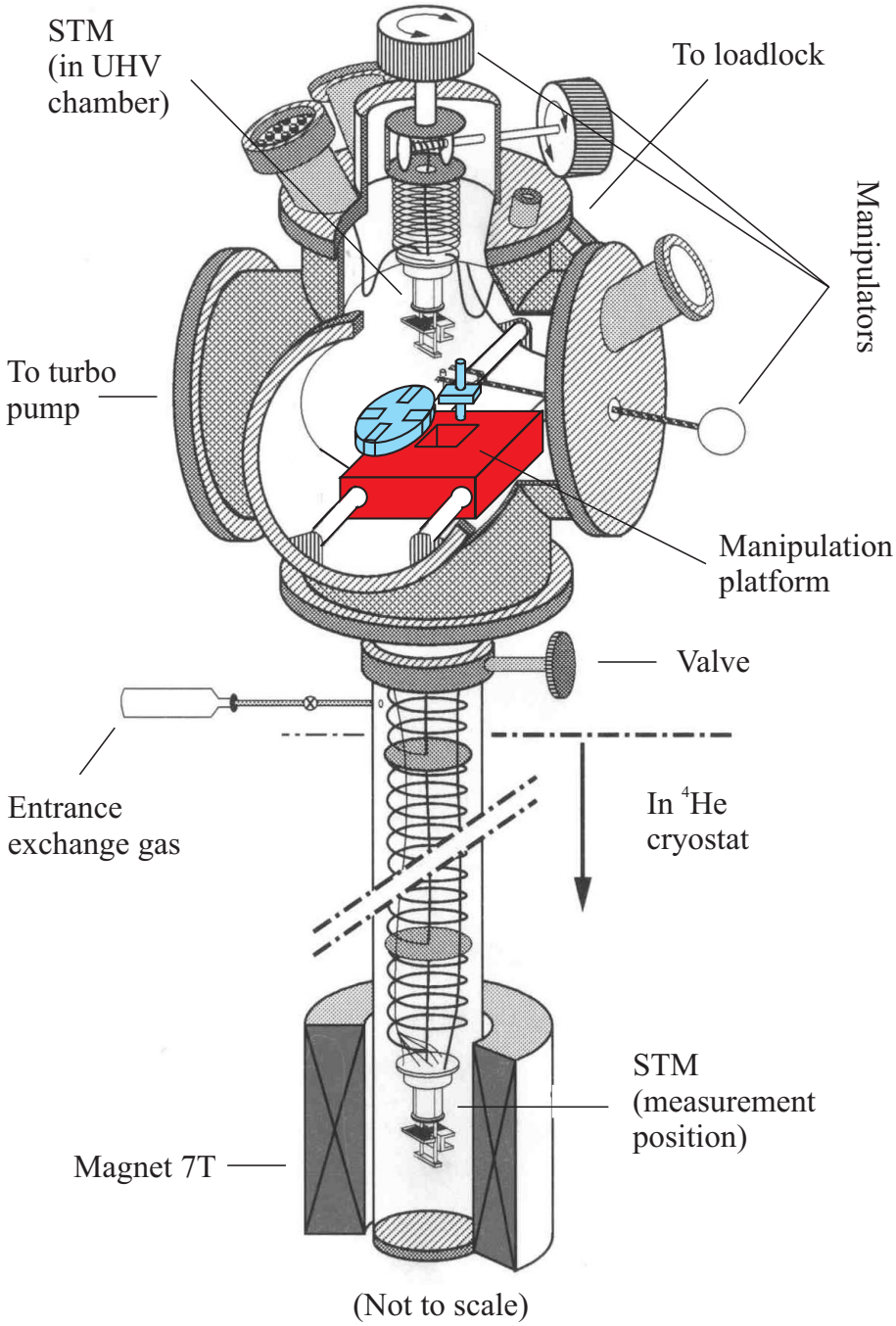

Figure 2.4: Schematic drawing of the low-temperature STM. For explanation see text.

2.4.2 *In situ* sample and tip exchange

The system described above has shown to be extremely useful for the study of high-temperature superconductors. One of its less convenience characteristics, however, was the lack of a fast-entry load-lock. That is, each time new samples were put into the UHV chamber, and each time the STM tip was exchanged, the chamber was exposed to atmospheric pressure. Though 3 or 4 samples could be put in at a time, this inevitably let to opening the system regularly. This was first inconvenient because the time lost by pumping down the system, and second because of the risks of carrying around the flange with the fragile STM.

This problem lead to a design of a manipulation platform which allows *in situ* sample tip exchange, and which is combined with a load-lock and magnetic linear transfer system. This design, originally conceived by Christophe Renner, was finalised and implemented during this thesis. The samples and tips can be transferred on a sample carriage via a load-lock into the UHV chamber. A fork in the platform allows to move the samples on the STM. The load-lock can be pumped down to $\approx 1 \cdot 10^{-7}$ mbar in a couple of hours. The most sophisticated part of the manipulation platform is the tip-exchange tool: a lift which allows to move tips up and down, in and out of the STM, driven by a rotating screw. This screw can be turned around with a standard UHV wobble stick. The tip-exchange mechanism has shown to be very reliable and safe, in spite of the limited optical access to the tip-holder position in the STM.

Especially the time gained for tip exchange is most considerable: It can actually be done in less than half an hour, while previously at least a day was needed to vent the chamber, change the tip, and pump down to UHV again.

2.5 The low-temperature STM in UHV

2.5.1 General set-up

The STM described in the previous section still leaves space for improvement. The sample surface is cleaner if the STM is operating in true UHV, without exchange gas. For measurements of vortex motion (see chapter 6) temperature variation in a magnetic field would be extremely useful. In the LT STM described above, this is hardly possible (with a magnetic field on, one can only reduce the base temperature from 4 to 2 degrees by pumping on the helium bath). Finally, in the latter system, all wiring is only very loosely fixed along the long spring from the top of the chamber to the measurement position at the bottom of the cryostat. Fixed, motionless wires produce considerably less noise, especially for the low-current signals in an STM experiment.

The developments described in this section are aimed at building a new, ^{4}He STM, operating in UHV, allowing measurements at variables temperatures at variable magnetic fields, and reducing electrical and mechanical noise with respect to the existing systems.

One of the main difficulties of designing a low-temperature, UHV STM, is to combine (i) a good thermal contact to a helium bath with (ii) full UHV compatibility and (iii) a transport device for moving STM and sample from the UHV chamber into the cryostat.

Proper UHV conditions exclude the use of an exchange gas. Thermal contact based on mechanical pressure is far from evident, and probably not sufficient when the heat load of STM wiring and of the transport device is taken into account.

This problem can be resolved if the helium from the helium bath is directly lead to an insert holding the STM, through a capillary. Such a helium capillary should be UHV compatible, and allow the STM to move from the bottom of the cryostat to the UHV chamber. These requirements have been met in a very elegant way in a prototype of an STM in a bottom-loading cryostat [29, 31]. This prototype, including ^{3}He refrigeration, was developed in Geneva in collaboration with Oxford Instruments. The UHV chamber where sample and tip can be exchanged, is placed at the bottom instead of at the top of a cryostat. This leads to a minimisation of the travel length from the measurement position in the lower part of the cryostat to the manipulation position in the UHV chamber. A spiral-shaped capillary for liquid helium supply has enough elasticity to allow such a travel length.

Liquid helium flows from the helium bath through an impedance (needle valve) into the capillary, and through the capillary into the 1K pot. The 1K pot is connected to a mechanical pump. By pumping on the 1K pot, temperatures below 4 K can easily be obtained. The temperature can be varied by changing the impedance of the needle valve, by changing the pumping speed, and by using a heater wire on the 1K pot.

The main problems of the ^{3}He bottom-loading cryostat are related to the *in-situ* transport mechanism of the insert (a solution chosen to limit the height of the system). Therefore, in the new system the insert has been made entirely rigid, and the motion is assured by a motor-driven bellow on top of the cryostat. In spite of these differences, the new LT STM has enormously benefited from the in-house experience with the ^{3}He system, as described in Martin Kugler's Ph.D. thesis [31]. This is particularly true for the design of the manipulation platform and the UHV chamber below. The general set-up of the instrument is explained in Fig. 2.5.

Thus the UHV-part of the system has been considerably simplified. Furthermore, all wiring for the STM can be fixed directly to the insert, diminishing noise resulting from long, moving wires, and reducing the risk of short-circuits.

The resulting design allows STM experiments in UHV, at variable temperature between 1.5 K and room temperature, and at variable magnetic fields (a 6 T magnet has been installed in the cryostat). In the following sections, I will describe the design of the ^{4}He insert, the manipulation platform for changing sample and tip in UHV, and the UHV chamber, all home-built and tested in Geneva.

2.5.2 ^{4}He insert

The ^{4}He insert allows variable temperature measurements from the temperature of pumped helium ($\sim$ 1 K) to room temperature [32–37]. In order to keep the insert as simple as possible, it was designed as one stainless steel tube, soldered on a UHV flange at the top, and welded in a copper block at the bottom, on which the STM is mounted. The main considerations for the design of the insert were: (i) The heat balance: the base temperature will result from the equilibrium of heat load and refrigeration due to evap-

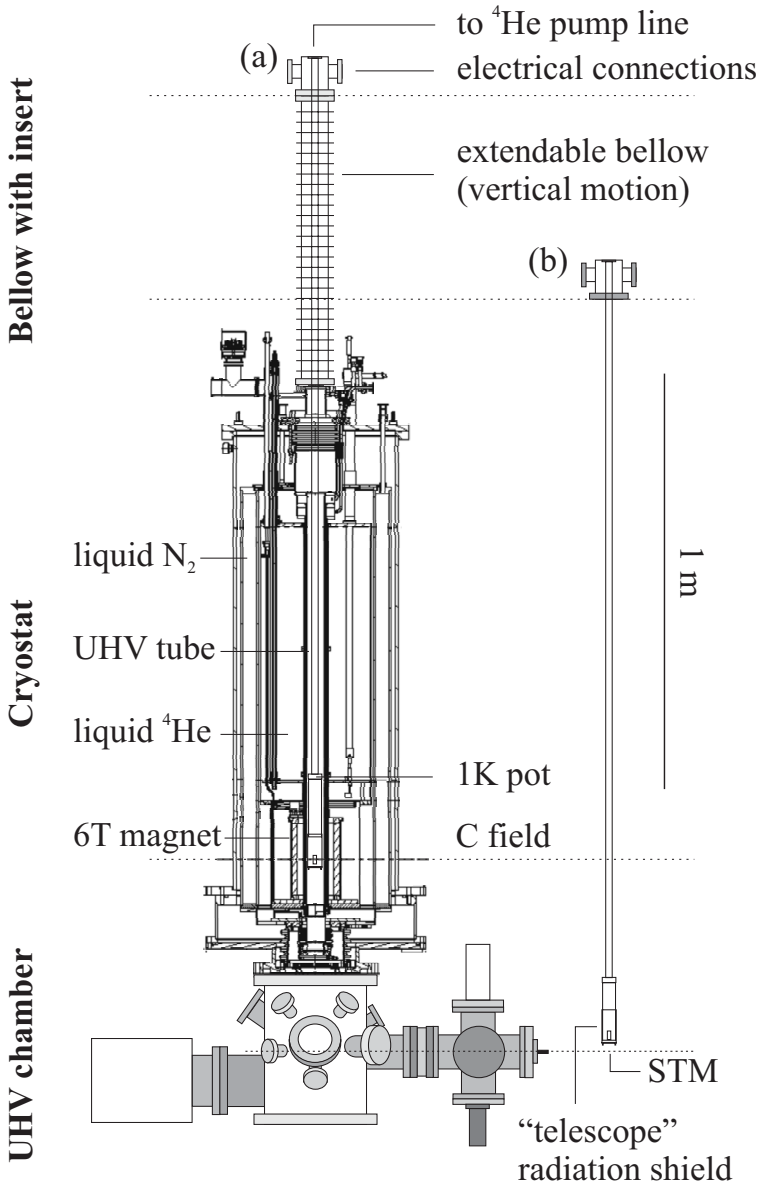

Figure 2.5: Schematic drawing of the low-temperature, UHV STM. (a) Bottom-loading cryostat, with on top of it an extendable bellow supporting the *rigid* insert (in measurement position). The insert is displayed separately, in manipulation position, in (b). The UHV space extends from the UHV chamber at the bottom, through a UHV tube with the insert in the cryostat, to the top flanges of the insert itself. A capillary (not indicated in the figure) feeds the 1K pot with helium from the main liquid helium bath. A telescope radiation shield protects the STM. It is down, covering the STM in (a), and up, allowing access to the STM in (b).

oration of helium. (ii) The effective pumping speed: depending on the pump *and* on the tubing design (impedance!), it should be sufficient to evacuate the evaporated helium. (iii) Mechanical strength: the tube should be able to support the pressure difference between its inner volume and the UHV space. Since these factors are mutually dependent, the proper dimensions of the insert are only found after several trial calculations. The boundary conditions are a desired base temperature between 1 and 1.5 K, the length of the insert $L = 2$ m, and a maximum pumping speed $S = 17.5$ l/s for the mechanical pump. A satisfactory calculation is sketched in the following paragraphs: it is based on a stainless steel tube with O/D 19.05 mm and wall thickness 0.25 mm. More details can be found in Refs. [32–35]. The insert has been tested extensively, before the STM and wiring were connected.

• Heat balance

Since the STM itself produces a negligible heat, all heat load comes from thermal conductivity and radiation. All wires are thin (see "Wiring and mounting of the STM", below) and made of stainless steel (except the wires for the heater), and contribute little to the total conductivity. The heat load due to conductivity W_C is thus entirely determined by the heat conductivity of the stainless steel tube. The conductivity of the stainless steel tube with one end at 1.5 K and the other end at room temperature, is easily calculated using standard formulas and tabulated values [32]: $W_C = 46$ mW. To avoid excessive thermal radiation, radiation shields are placed between the warm and the cold end of the insert (inside the tube, the helium gas flow is allowed by 4 alternating half-disks radiation shields). It is verified that the cooling power of the evaporated helium is sufficient to cool the radiation shields to < 100 K. The radiation heat at the 1K pot then follows $W_R < 5$ mW. The refrigeration at the 1K pot is the result of the latent heat of helium evaporation, which is about 21 J/g. Since part of this refrigeration, 8.8 J/g, is lost due to the enthalpy change of helium between 4 and 1 K, the total heat balance becomes (with $\dot{Q}_m$ the mass flow of helium in g/s):

$$21\dot{Q}_m = W_C + W_R + 8.8\dot{Q}_m. \tag{2.1}$$

From the heat balance, it is derived that a molar flow $\dot{Q}_n = 1$ mmol/s helium is needed to cool the bottom of the insert to below 1.5 K. (This corresponds to a helium flow of 30 ml liquid/h, small compared to the total helium consumption – about 0.5 l/h – of the cryostat.) In this estimation the refrigeration of the tube due to the evaporated helium gas is not taken into account, so that probably less helium is needed.

• Effective pumping speed

The effective pumping speed S_{eff} at the 1K pot is not necessarily the same as the pumping speed of the mechanical pump at the pump inlet S_p. It is also determined by the gas flow conductivity C of the stainless steel pumping tube. The exact conductivity of the tube is difficult to predict, among others because the pressure (p) and temperature (T) gradients along the tube are not known exactly. One can however assume a linear temperature gradient from 1 K to 300 K for the first meter of the insert (in the cryostat), and a constant temperature of 300 K for the second meter (in the bellow). Then it is

possible to calculate the pressure drop in the insert for a given $\dot{Q}_n$ (gas flow in mol), and to derive the corresponding volume flow $p\dot{Q}_V$ from the pressure at the top of the insert. This should be equal to (or smaller than) the maximum pumping speed of the mechanical pump.

The insert with diameter D and length L is now regarded as the serial assembly of N different tubes with diameter D, length $\Delta L = L/N$, and conductivity $C_i(p_i, T_i)$. The total conductivity of the tube follows from the sum

$$C = (1/C_1 + 1/C_2 + ... + 1/C_i + ... + 1/C_N)^{-1}. \tag{2.2}$$

ΔL is taken small. Starting from the desired pressure at the 1K pot $p_0(T_0)$, the conductivity and pressure drop

$$\Delta p_i = p_i \dot{Q}_{V,i}/C_i, \tag{2.3}$$

can be calculated for each element i. The volume flow follows from $p_i\dot{Q}_{V,i} = \dot{Q}_n RT_i$ (ideal gas law). Each $C_i(p_0 - \Delta p_i, T_i)$ is calculated using standard formulas [32] for viscous and molecular flow (depending on the mean free path in the helium gas).

For a given pressure at the bottom of the insert, the pressure drop, and thus the pressure on top of the insert and the required pumping speed, are easily obtained. The helium flow of $\dot{Q}_n = 1$ mmol/s, necessary to achieve a base temperature of 1.5 K ($p_0 = 3.6$ Torr), requires a pump speed of 8.25 l/s. This is roughly half of the maximum pump speed of the mechanical pump. According to these estimations, the base temperature of the insert is thus $\lessapprox$ 1.5 K. For lower temperatures, the required base pressure p_0 rapidly drops, resulting in rapidly increasing required pumping speed.

• Mechanical strength

Although the walls of the insert should be as thin as possible to decrease thermal conductivity, they should be thick enough to support the pressure difference between the inner space of the tube, and the UHV space around it. The strength of the tube critically depends on the ratio between the wall thickness and the diameter of the tube. For the dimensions given above, the tube will support an outer pressure of maximum 2 bar, and an inner pressure up to 20 bar [32]. This means that even in case of important failure of the apparatus or of the experimentalist, the insert will not collapse.

• Testing the insert

In order to test the insert, it was put into a leak-tight stainless steel tube (hereafter called test tube, to distinguish it from the insert itself), mounted in a glass cryostat. With a helium exchange gas between the test tube and the insert, the insert could thus be tested for leaks between 4 K and room temperature. The leak rate was determined to be $< 10^{-10}$ mbar·l/s. Thermal cycling did not influence this result.

In the same test set-up, the space between the test tube and the insert was evacuated for isolation between the helium bath and the insert. The 1K pot was connected to the helium bath by a silicon-oxide capillary, with approximately the impedance required to

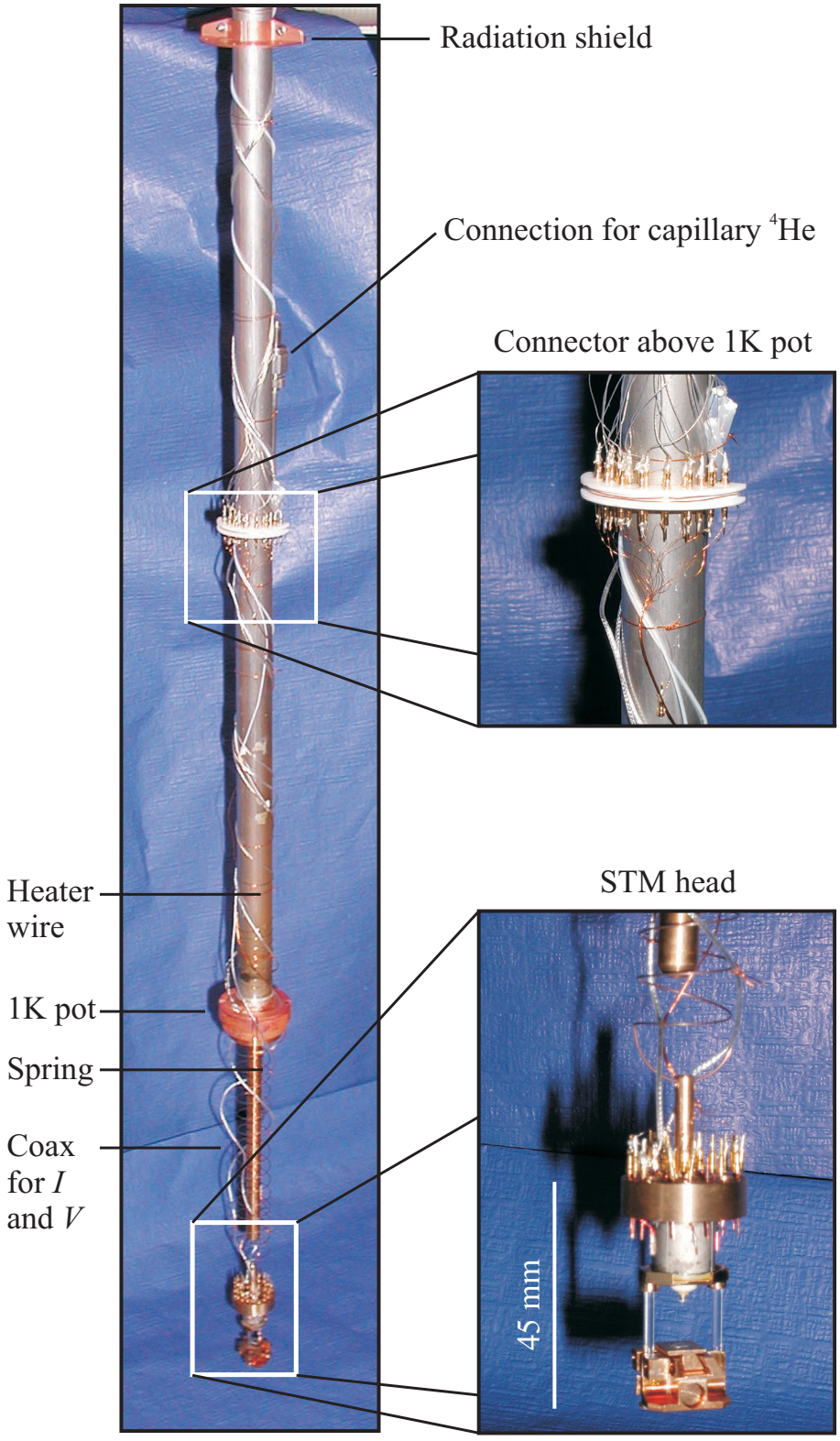

Figure 2.6: The bottom part of the insert with the STM. The radiation shields around the STM have been removed.

allow a helium flow of $\dot{Q}_n = 1$ mmol/s from the helium bath to the 1K pot [32]. Without precise optimisation of the impedance (which in the final set-up can be adjusted with a needle valve), with only minimum radiation shielding, and a pumping speed of 8.8 l/s, a base temperature of 1.5 K was reached. With proper adjustment of the impedance, the temperature could be lowered even further, as could have been expected because of the conservatively chosen parameters in the design.

- **Wiring and mounting of the STM**

To reduce thermal conductance, all (24) wires descending from the top of the insert to the 1K pot, are made of stainless steel, except two copper wires ($\phi = 0.24$ mm) for the heater current. The nichrome heater wire at the 1K pot has a resistance of 25 Ω. Above the 1K pot, 18 stainless steel wires are clamped to a home-made connector (apart from these, there are 4 wires for the thermometer at the 1K pot, and 2 spare wires). From the connector, 18 flexible 50μm capton insulated copper wires lead to the STM. Furthermore two miniature stainless steel coaxial cables go from the top of the insert directly down to the STM, one for the tunnel current and one for the sample bias. Their shields are floating with respect to the insert, to be able to separate low-signal shielding from the cryostat, and avoid ground loops. All wires have been wrapped around the insert over the full length of the insert, to ensure thermal anchoring.

The STM is suspended on a copper-beryllium spring with a resonance frequency of 1∼2 Hz for vibration isolation. The damping of the instrument is provided by the wires for electric connections. The STM is protected by a radiation shield, part of which can move up to allow access to the STM for sample and tip exchange (see the following section). The bottom part of the insert, with fragile wiring and connectors, is protected from the spiral-formed helium capillary by an additional, removable tube. Cernox thermometers at the STM and the 1K pot indicate the temperature. The bottom part of the insert, without the shields protecting the STM, the wires and the connectors, is shown in Fig. 2.6.

2.5.3 STM manipulation platform

When the insert with the STM is in the lower, manipulation position, the heat shield should be removed to access the STM. Once the STM is made accessible, a sample-holder should be exchanged and positioned under the STM tip. These operations are performed with the help of the manipulation platform in the UHV chamber, which also serves as a storage for samples and tips [31]. The latter are imported into the UHV chamber on a circular sample carriage, via the load-lock.

2.5.4 UHV chamber

The UHV chamber consists of a CF300 cylindrical tube to be mounted under the cryostat, and of several ports for the ion pump, for the load-lock, and for the necessary equipment for control and manipulation in the vacuum space [31]. The load-lock allows to bring samples and tips into the main chamber without breaking the vacuum. The whole

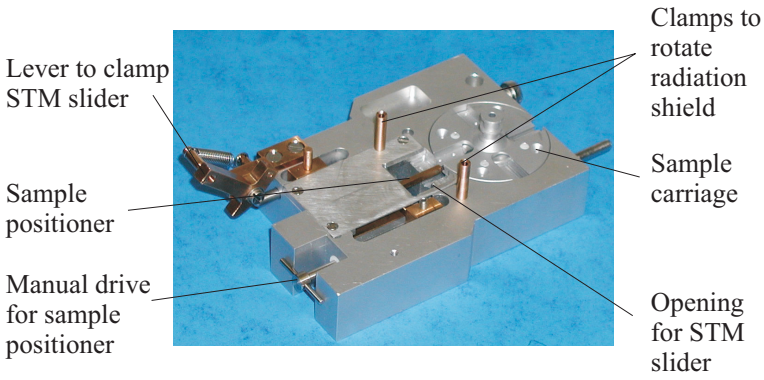

Figure 2.7: The manipulation platform. First, the radiation shield can be turned around, and opened using cylindrical clamps on the table. The bottom part of the STM (the slider) with the sample holder can be lowered into the opening in the centre of the platform. A fork (not visible) in the platform, driven by the lever at the top left, clamps the slider in its position. Using the sample positioner, samples can be transferred from the STM to the sample carriage and vice versa.

chamber is home-built and leak-tested to $< 10^{-9}$ mbar·l/s. Without baking, a base pressure of $1 \cdot 10^{-9}$ mbar is reached. The UHV chamber is shown in Fig. 2.8.

A preliminary vacuum is obtained by a turbo pump via the load-lock. When the system is fully operating, the ion pump with a titanium sublimator pumps the system further down, and maintains the UHV without any additional vibrations. The pressure in the main chamber is controlled by an ion gauge, and a mass spectrometer allows residual gas analysis.

2.5.5 Vibration isolation

The vibration isolation foreseen so far is relatively simple: The system stands on a concrete basement separate from the building (external vibration isolation), and the STM is suspended on a spring with low resonance frequency (1∼2 Hz, *in-situ*, internal vibration isolation). In principle, the external vibration isolation can still be improved by supporting the system by air-spring legs. The internal vibration isolation can be improved by Eddy-current damping, to suppress the resonant modes of the spring. In our case Eddy current damping is complicated because the STM head should fit into the bore of a superconducting magnet, and the magnets for the damping system should not interfere with the magnetic field applied to the sample. The damping system should therefore be outside the superconducting magnet, above [38] or preferentially – to avoid affecting the stability of the STM head – below.

2.5.6 System assembly: outlook

The main components – the electronics, the insert with STM, the manipulation platform and the UHV chamber – of the UHV LT STM having been tested, the next phase is the assembly of the system. The cryostat having just been delivered (April 2002), this means connecting the different components and taking care of minor adjustments.

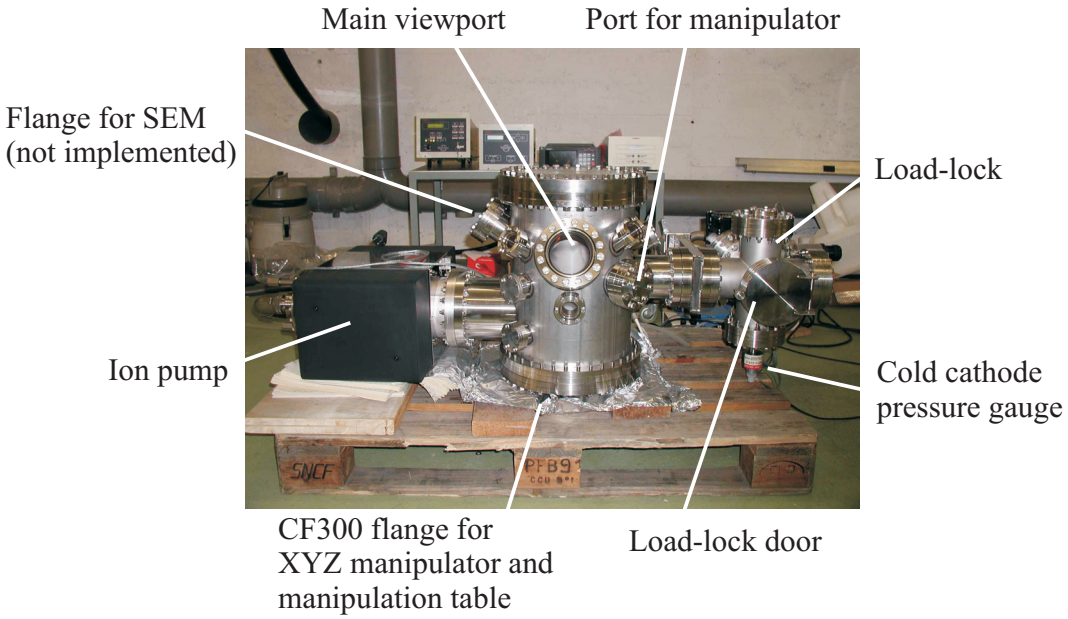

Figure 2.8: Front view of the UHV chamber, as it will be mounted under the cryostat. Not visible: the ion gauge and the mass spectrometer at the back of the main chamber, and the turbo pump at the back of the load-lock. In the final configuration, a magnetically driven linear manipulator transports samples and tips from the load-lock into the main chamber and vice versa. The manipulation platform will be mounted on a XYZ manipulator at the bottom flange of the chamber.

Here follows a list of actions still to be undertaken.

- ⋆ Testing the cryostat. This implies testing the cryostat for its leak-tightness and for its liquid helium consumption. Furthermore, the magnet will have to be energised.
- ⋆ The installation of the cryostat in its final laboratory space. The support on which the cryostat will be mounted, is about to be finished, and will stand on a concrete block isolated from the building.
- ⋆ Connection of the UHV chamber at the bottom of the cryostat. Testing bake-out equipment, and base pressure of the complete system. After this the remaining UHV manipulators will be mounted on the chamber. So far, they have not been mounted, to allow easy transport of the UHV chamber.
- ⋆ Installing the insert in the cryostat. Verifying that it can move freely up and down. Finally the helium pick-up capillary will be put in the proper shape, after which the connection between the helium bath and the 1K pot can be established. Again the UHV conditions will need testing, as well as the cryogenics.
- ⋆ Full testing of the proper functioning of the STM at low temperature and UHV (the translator has already been tested to 4.2 K in a top-loading cryostat).
- ⋆ Acoustic and electro-magnetic isolation from the surroundings. To this end a Faraday cage of sufficient mass should be sufficient.
- ⋆ Testing the system performance on well-known materials like graphite and $NbSe_2$.

2.6 Summary

All measurements described in the following chapters have been performed on the LT STM in exchange gas (section 2.4). The system is based on the STM head designed by Christophe Renner in the beginning of the 1990s, and allows *in-situ* cleaving and measurements at various temperatures and magnetic fields.

During the last years, it has been equipped with new (home-built) analogue feedback electronics, and with a load-lock and a manipulation platform allowing *in-situ* sample and STM tip exchange without breaking the vacuum.

In order to be able to operate the STM in UHV and without exchange gas, to be able to perform variable temperature measurements in a magnetic field, and to reduce noise related to *in-situ* moving wires, a new LT STM was designed (section 2.5). The main components of the system have been completed and tested: (i) A ^{4}He insert, allowing a base temperature of < 1.5 K, with a short-scanner STM mounted on it. (ii) A manipulation platform for sample cleaving, and for sample and tip exchange in UHV. (iii) A UHV chamber in which – without baking – a pressure of $1 \cdot 10^{-9}$ mbar is reached. The chamber is directly connected to a load-lock, which allows to transport samples and tips into the UHV chamber without breaking the vacuum. The cryostat having been delivered recently, the main remaining task is fitting the different components together, and testing the system performance.

Based on the experience in operating the LT STM and in developing the new system, several suggestions have been made to further improve the STM head (section 2.3) and the vibration isolation (section 2.5). A prototype of a new STM head is currently being constructed.

Manufacturers and distributors

Product	Manufacturer	Distributor
Aluminium-oxide tubes	Friedrichsfeld GmbH, Mannheim (D)	Degussa AG, Baar
Bottom-loading cryostat	Oxford Instruments, www.oxinst.com	Oxford Instruments, Wiesbaden (D)
Cernox thermometers / controller	Lakeshore Cryotronics, www.lakeshore.com	TECO René Koch, Gland
EBL2 piezo ceramic tubes	Staveley Sensors, www.staveleyndt.com	-
Electronics components	various	Distrelec, www.distrelec.ch
Electronics components	ELMA Electronic, Epalinges	-
Epoxy glues, Epotek H70E and 417	Epoxy Technology, www.epotek.com	Polyscience, Cham
Heater tube (B56409)	Fisher Scientific, www.fishersci.com	Fisher Scientific, Wohlen
Insulated cables	LEMO, Eclubens	-
Linear shift mechanism	Kurt Lesker, www.lesker.com	-
Liquid helium level monitor	Cryomagnetics, www.cryomagnetics.com	TECO René Koch, Gland
Lock-in amplifier	Stanford Research Systems, www.srsys.com	GMP, www.gmp.ch
Magnetically driven wobble-stick	Ferrovac, Zürich	Semisupply, Walchwill
Mass spectrometer	Leybold Vacuum, www.leyboldvac.de	Leybold, Zürich
Operational amplifiers	various	Spoerle, www.spoerle.com
Resistor 1GΩ	EBG, www.ebg.at	Etronics, www.etronics.ch
Sapphire rails	Frieden, Balerna	-
Silicium-oxide capillary	Agilent, www.chem.agilent.com	MSP Friedli, Koeniz
Stainless steel capillary tube	LMC Christaud, Echirolles (F)	-
Stainless steel mini-coaxial cable	Lakeshore Cryotronics, www.lakeshore.com	TECO René Koch, Gland
Stainless steel tube	Oxford Instruments, www.oxinst.com	Meili Kryotech, Döttingen
Teflon coated copper wire	Goodfellow, www.goodfellow.co.uk	-
Teflon coated stainless steel wire	Advent Research Materials, www.advent-rm.com	-
STM tip wire	Goodfellow, www.goodfellow.co.uk	-
Vacuum pumps	Varian, www.varianinc.com	Varian, Torino (I)
VCR Swagelok fittings	Swagelok, www.swagelok.com	Arbor Ventil + Fitting, Niederrohrdorf
UHV feedthroughs, connectors	Ceramaseal, www.ceramaseal.com	Meili Kryotech, Döttingen
UHV gate valve	VAT, www.vat.ch	-
UHV hardware	Thermo Vacuum Generators, www.vacgen.com	Meili Kryotech, Döttingen
XYZ manipulator	Kurt Lesker, www.lesker.com	-

References

[1] J. Lindhal, T. Takanen, and L. Montelius, J. Vac. Sci. Technol. B **16**, 3077 (1998).

[2] G. Binnig and D. P. E. Smith, Rev. Sci. Instrum. **57**, 1688 (1986).

[3] F. J. Giessibl, Ch. Gerber, and G. Binnig, J. Vac. Sci. Technol. B **9**, 984 (1991).

[4] J. Heil, J. Wesner, K. Hillmann, and J. Grill, J. Vac. Sci. Technol. A **6**, 401 (1988).

[5] A. K. Schmidt and J. Kirschner, J. Vac. Sci. Technol. B **9**, 648 (1991).

[6] G. Binnig, H. Rohrer, Ch. Gerber, and E. Weibel, Appl. Phys. Lett. **40**, 178 (1982).

[7] Burleigh Instruments, www.burleigh.com.

[8] N. Shimizu, T. Kimura, T. Nakamura, and I. Umedu, J. Vac. Sci. Technol. A **8**, 333 (1990).

[9] K. Besocke, Surface Science **181**, 145 (1987).

[10] J. W. Lyding, S. Skala, J. S. Hubacek, R. Brockenbrough, and G. Gammie, Rev. Sci. Instrum. **59**, 1897 (1988).

[11] Ch. Renner, Ph. Niedermann, A. D. Kent, and Ø. Fischer, J. Vac. Sci. Technol. A **8**, 330 (1990).

[12] Ch. Renner, Ph. Niedermann, A. D. Kent, and Ø. Fischer, Rev. Sci. Instrum. **61**, 965 (1990).

[13] S. H. Pan, E. W. Hudson, and J. C. Davis, Rev. Sci. Instrum. **69**, 125 (1999).

[14] Omicron Vakuumphysik GmbH, www.omicron.de.

[15] VTS-Createc GmbH, www.vts-createc.com.

[16] A. D. Kent, Ch. Renner, Ph. Niedermann, J.-G. Bosch, and Ø. Fischer, Ultramicroscopy **42-44**, 1632 (1992).

[17] K. Ikeda, K. Takamuku, H. Kubota, R. Itti, and N. Koshizuka, Rev. Sci. Instrum. **64**, 2221 (1993).

[18] S. Stranick, M. Kamna, and P. S. Weiss, Rev. Sci. Instrum. **65**, 3211 (1994).

[19] S. H. Tessmer, J. W. Lyding, and D. J. van Harlingen, Rev. Sci. Instrum. **65**, 2855 (1994).

[20] R. R. Schulz and C. Rossel, Rev. Sci. Instrum. **65**, 1918 (1994).

[21] H. Hancotte, D. N. Davydov, M. Ye, and R. Deltour, Physica B **204**, 206 (1995).

[22] J. G. Dubois, J. W. Gerritsen, J. G. Hermsen, and H. van Kempen, Rev. Sci. Instrum. **66**, 4146 (1995).

[23] G. Meyer, Rev. Sci. Instrum. **67**, 2960 (1996).

[24] Ch. Wittneven, R. Dombrowski, S. H. Pan, and R. Wiesendanger, Rev. Sci. Instrum. **68**, 3806 (1997).

[25] D. Wehnes, J. Meier, J. Classen, and C. Enss, Appl. Phys. A **66**, 41 (1998).

[26] J. H. Ferris, J. G. Kushmerick, J. A. Johnson, M. G. Youngquist, R. B. Kessinger, H. F. Kingsbury, and P. S. Weiss, Rev. Sci. Instrum. **69**, 2691 (1998).

[27] L. E. Harrel and P. N. First, Rev. Sci. Instrum. **70**, 125 (1999).

[28] O. Pietzsch, A. Kubetzka, D. Haude, M. Bode, and R. Wiesendanger, Rev. Sci. Instrum. **71**, 424 (2000).

[29] M. Kugler, Ch. Renner, V. Mikheev, G. Batey, and Ø. Fischer, Rev. Sci. Instrum. **71**, 1475 (2000).

[30] Ch. Renner, Ph.D. thesis, University of Geneva, n° 2620 (1993).

[31] M. Kugler, Ph.D. thesis, University of Geneva, n° 3158 (2000).

[32] R. R. Conte, *Éléments de cryogénie* (Masson et C^{ie}, Paris, 1970).

[33] R. C. Richardson and E. N. Smith, *Experimental Techniques in Condensed Matter Physics at Low Temperatures* (Addison-Wesley Publishing Company, Inc., California, Massachusetts, New York, 1988).

[34] G. K. White, *Experimental Techniques in Low-Temperature Physics*, 3rd. ed. (Clarendon Press, Oxford, 1979).

[35] S. W. Van Sciver, *Helium Cryogenics* (Plenum Press, New York, 1986).

[36] B. N. Engel, G. G. Ihas, E. D. Adams, and C. Fombarlet, Rev. Sci. Instrum. **55**, 1489 (1984).

[37] E. T. Swartz, Rev. Sci. Instrum. **57**, 2848 (1986).

[38] H. J. Hug, B. Stiefel, P. J. van Schendel, A. Moser, S. Martin, and H.-J. Güntherodt, Rev. Sci. Instrum. **70**, 3625 (1999).

Chapter 3

Theoretical Aspects of Tunnelling Spectroscopy

3.1 Tunnelling theory

To get a proper understanding of what can be measured with an STM, it is useful to start with a discussion of tunnelling through a planar junction. As a first approximation, this can be described in a one-dimensional model of a potential barrier, as found in standard quantum mechanics text books [1]. It is depicted in Fig. 3.1. By matching the wave functions across the barrier, one can calculate the probability of transmission for an incoming plane wave, leading to a transmission coefficient of

$$|T|^2 \approx \mathrm{e}^{-2\kappa d}, \tag{3.1}$$

where $\kappa = \sqrt{2m\phi/\hbar^2}$, with ϕ the height of the barrier, m the electron mass, and d the width of the barrier. This approximation is only valid for electron energies $\ll \phi$.

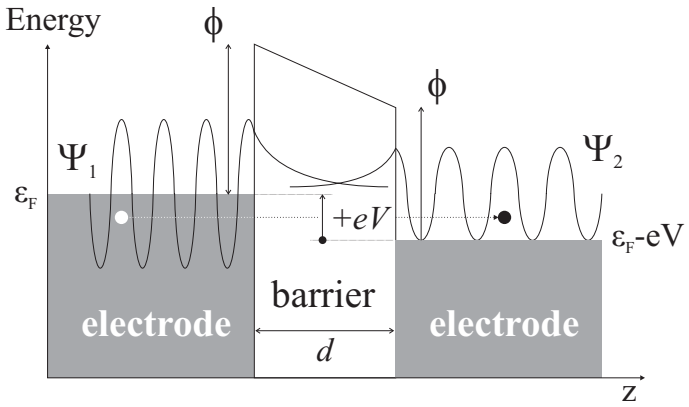

Figure 3.1: Schematic representation of tunnelling through a potential barrier of height ϕ and width d. The Ψ denote the wave functions at each side of the barrier. A potential of eV is applied across the junction.

A more powerful approach implies the use of a transfer Hamiltonian. The two sides of the junction are described by their respective Hamiltonians H_1 and H_2, while the

tunnelling (transfer) of electrons from one side of the junction to the other is treated as a perturbation term H_T [2]: the two sides of the junction are assumed not to influence each other. The full Hamiltonian becomes

$$\begin{aligned} H &= H_1 + H_2 + H_T, \\ H_T &= \sum_{\mathbf{kp}} T_{\mathbf{kp}}[c^\dagger_{\mathbf{k}} c_{\mathbf{p}} + c^\dagger_{\mathbf{p}} c_{\mathbf{k}}]. \end{aligned} \tag{3.2}$$

$\mathbf{k}$ and $\mathbf{p}$ are the wave vectors at both sides of the junction, $T_{\mathbf{kp}}$ is the tunnelling matrix element, and $c^\dagger$ and c are the electron creation and annihilation operators.

Using many-body theory, the tunnel current I as a function of the potential eV across the junction, is shown to be

$$I(V) = 2e \sum_{\mathbf{kp}} |T_{\mathbf{kp}}|^2 \int_{-\infty}^{\infty} \frac{\mathrm{d}\omega}{2\pi} A_1(\mathbf{k},\omega) A_2(\mathbf{p},\omega - eV)[f(\omega) - f(\omega - eV)], \tag{3.3}$$

where A_1 and A_2 are the spectral functions on both sides of the junction, and $f(\omega)$ is the Fermi-Dirac distribution function.

Assume that one of the electrodes is metallic, so its spectral function is given by a delta function, $A_2(\mathbf{p},\omega) = 2\pi\delta(\omega - \xi_{\mathbf{p}})$, leading to

$$I(V) = 2e \sum_{\mathbf{kp}} |T_{\mathbf{kp}}|^2 A_1(\mathbf{k}, \xi_{\mathbf{p}} + eV)[f(\xi_{\mathbf{p}} + eV) - f(\xi_{\mathbf{p}})]. \tag{3.4}$$

This formula will be the basis for the interpretation of tunnelling spectra given below.

$T_{\mathbf{kp}}$ was first evaluated by Bardeen, who derived

$$T_{\mathbf{kp}} = \hbar^2/(2m) \int \mathrm{d}\mathbf{S}[\Psi^*_{\mathbf{k}} \bigtriangledown \Psi_{\mathbf{p}} - \Psi_{\mathbf{p}} \bigtriangledown \Psi^*_{\mathbf{k}}], \tag{3.5}$$

where $\mathbf{S}$ is the surface separating the two sides of the junction [3].

To gain insight in the effect of the tunnelling matrix element, one can employ independent-electron theory. As was shown by Harrison [4, 5],

$$|T_{\mathbf{kp}}|^2 = |\partial\xi_{\mathbf{k}}/\partial k_z||\partial\xi_{\mathbf{p}}/\partial p_z| D(\varepsilon_z)\delta(\mathbf{k}_{x,y} - \mathbf{p}_{x,y}), \tag{3.6}$$

$$D(\varepsilon_z) = g \exp\{-2 \int_0^d \mathrm{d}z \sqrt{2m/\hbar^2[U(z) - \varepsilon_z]}\}, \tag{3.7}$$

$$g = \frac{16kp\kappa^2}{(k^2 + \kappa^2)(p^2 + \kappa^2)}. \tag{3.8}$$

Thus $|T_{\mathbf{kp}}|^2$ is proportional to the inverse of the density of states on both sides of the junction in the tunnelling direction ($\partial k_z/\partial\xi_{\mathbf{k}}$ and $\partial p_z/\partial\xi_{\mathbf{p}}$). The energy of the tunnelling electrons $\varepsilon_{\mathbf{k}}$ is decomposed in a part ε_{xy} perpendicular to the tunnelling direction and a part ε_z parallel to it; $\mathbf{k}_{x,y}$ and $\mathbf{p}_{x,y}$ are the wave vectors perpendicular to the tunnelling direction z, d is the width of the junction, and $U(z)$ the barrier potential. The expression for g results from wave vector matching across the barrier, and is exact for a square barrier potential of height ϕ, with $\kappa = \sqrt{2m/\hbar^2(\phi - \varepsilon_z)}$; far from the band edges g

is approximately a constant [5], and Eq. 3.7 becomes identical to Eq. 3.1 for electron energies small compared to the barrier height. In the following it will be assumed that the variation of g with momentum is negligible (g is assumed to be unity) compared to the variation of the exponential term in $D(\varepsilon_z)$.

In the sections 3.2 and 3.3 these equations will form the framework for treating tunnelling in the STM configuration, and for understanding what is measured by tunnelling spectroscopy.

3.2 Tunnelling in the STM configuration

Eq. 3.1 provides an explanation for the tremendous vertical resolution (< 0.1 Å) of the STM. In an STM experiment, the two sides of the tunnel junction – tip and sample – are separated by vacuum (or air when the STM is operated under atmospheric pressure). The height of the tunnel barrier corresponds to the work function ϕ on the two sides of the junction. The decay constant $\kappa = \sqrt{2m\phi/\hbar^2} \approx 0.5\sqrt{\phi}$ Å^{-1}, with ϕ in eV. For a typical metal ϕ is about 5 eV. Thus $\kappa \approx 1$ Å^{-1}, meaning that for a variation of the tip-sample distance by 1 Å, the tunnel current will vary by about one order of magnitude.

To our knowledge, an expression for the corrugation in an STM experiment was first obtained by Tersoff and Hamann [6]. The corrugation is the variation in the vertical STM tip position (for constant tunnel current) between different sites on the surface, on and in-between the atomic positions. To obtain atomic resolution, the corrugation should be larger than the vertical resolution of the STM. In the Tersoff-Hamann theory, the tip is modelled by an apex with spherical (s-wave) symmetry and curvature R. Starting with Bardeen's transfer Hamiltonian approach, the matrix element of Eq. 3.5 is evaluated for the STM configuration, and the tunnelling conductance becomes

$$\sigma \approx 0.1 R^2 \mathrm{e}^{2\kappa R} \sum_{\mathbf{k}} |\Psi_{\mathbf{k}}(\mathbf{r_0})|^2 \delta(\varepsilon_{\mathbf{k}} - \varepsilon_F), \tag{3.9}$$

for transitions at the Fermi level ε_F. $\Psi_{\mathbf{k}}(\mathbf{r_0})$ is the wave function of the sample evaluated at the centre of the tip, which – apart from a constant – should replace $T_{\mathbf{kp}}$ in Eq. 3.4. With an exponentially decaying wave function, and with an ohmic behaviour of the tunnel resistance, this leads again to $I = V\sigma \propto \mathrm{e}^{-2\kappa d}$. As can be intuitively expected, Eq. 3.9 implies that the tunnel current I directly depends on the charge density at the Fermi level on the surface of the sample. This theory was refined for tips with electronic states of higher orbital momentum (p and d, instead of s) by Chen [7, 8]. He showed that the corrugation following from Eq. 3.9 is considerably enhanced for d_{z^2} symmetry, down to a fraction of an Å. d_{z^2} symmetric states can indeed be present at standard tips made of W or Ir.

It should be underlined that the Tersoff-Hamann theory relies on an approximate form of the wave functions of the sample and of the matrix elements (3.5), and on a highly simplified tip geometry. Furthermore, it neglects tip-sample interactions. Improvements on the description of the wave functions followed from scattering theory, and in some cases the matrix elements could be explicitly calculated [9]. More recent theoretical approaches use ab-initio calculations to model the whole tip-sample system. Some of the

most recent results are [10]: (i) Atomic resolution can only be obtained for a narrow range of tip-sample distances (a range of about 0.5 Å). For distances smaller than some Å the tip-sample interaction becomes too important, while at larger distances the corrugation is not sufficient. (ii) For short tip-sample distances, relaxation of the atoms near the tunnel junction can even cause the tunnel current to decrease when the tip-sample distance becomes smaller. These conclusions correspond to the experimentalist's wisdom that atomic resolution is only obtained after adjusting the parameters determining the tunnel junction, and that the interpretation of STM images and spectra is certainly not straightforward.

It should be realised that numerical approaches of the full tip-sample configuration are (so far) restricted to simple systems of which the electronic structure is well understood. This is certainly not the case for high-temperature superconductors, which are the main subject of this thesis. In the latter case, the interpretation of the experimental data – especially of tunnelling spectra – relies on approximate models, in combination with measurements which compare tunnelling data at different temperatures and magnetic fields.

3.3 Tunnelling spectroscopy

In order to interpret tunnelling $I-V$ spectra in terms of sample properties, Eq. 3.4 is further simplified by using the delta function in the matrix element (3.6) for eliminating the sum over the tip wave vector perpendicular to the tunnelling direction. Furthermore, the sum over p_z is transformed into an integral over energy. The Jacobian of this transformation eliminates the term $|\partial\xi_{\mathbf{p}}/\partial p_z|$ in the matrix element. The tunnelling conductance is now given by [2, 11]

$$\frac{\mathrm{d}I(V)}{\mathrm{d}V} = \int_{-\infty}^{\infty} \frac{d\omega}{2\pi} \left(-\frac{\partial f(\omega - eV)}{\partial eV} \right) \sum_{\mathbf{k}} |T_{\mathbf{k}}|^2 A_S(\mathbf{k}, \omega). \tag{3.10}$$

The function $[-\partial f(\omega - eV)/\partial eV]$ is peaked around $\omega = eV$ and has the effect of broadening the spectra over an energy of the order $k_B T$. The matrix element is now given by

$$|T_{\mathbf{k}}|^2 = 2e^2 |\partial\xi_{\mathbf{k}}/\partial k_z| D(\varepsilon_z), \tag{3.11}$$

with $D(\varepsilon_z)$ as in Eq. 3.7.

If the matrix element is (approximately) a constant, the $\mathrm{d}I(V)/\mathrm{d}V$ spectra represent the quasiparticle density of states [DOS, $N(\omega) = \sum_{\mathbf{k}} A_S(\mathbf{k}, \omega)$], smeared out by the temperature. This explains the observation of the BCS DOS in Giaever's pioneering tunnelling experiments [12, 13].

In general, however, the matrix element is not a constant. First, since $\varepsilon_z = \varepsilon_{\mathbf{k}} - \varepsilon_{xy} - \varepsilon_F$ and assuming that ε_{xy} is a monotonic function of the transverse momentum $\mathbf{k}_{x,y}$, the energy dependence of

$$D(\varepsilon_z) \approx \exp[-2d\sqrt{2m/\hbar^2(\phi - \varepsilon_z)}] \tag{3.12}$$

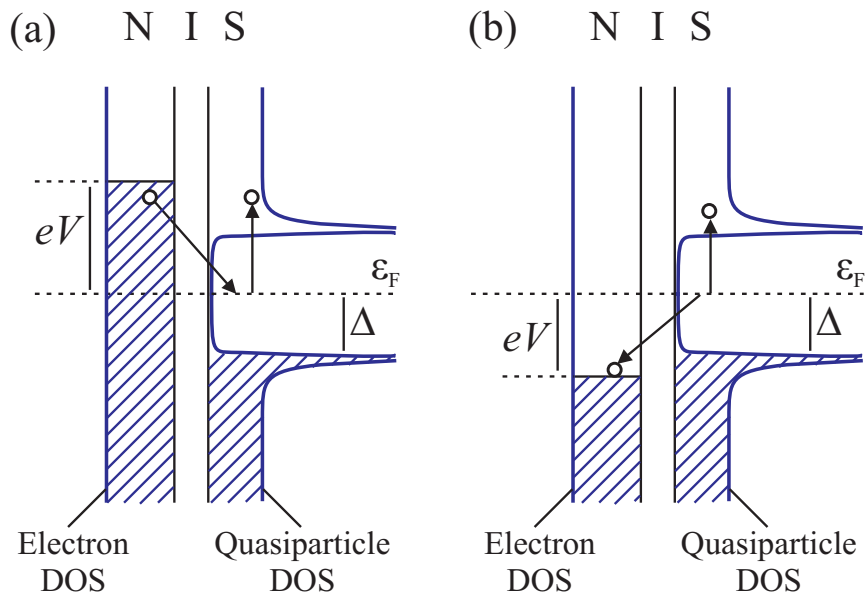

Figure 3.2: Electron tunnelling between a normal metal (N) and a superconductor (S) through an insulating barrier (I), at $T = 0$ K. The vertical scale is the energy. V is the bias voltage across the tunnel junction, ε_F is the Fermi energy (in the superconductor), where the Cooper pairs are located. (a) An electron tunnels from the metal to the superconductor. In the superconductor, it will form a Cooper pair with an other electron. Conservation of energy requires the excitation of a quasiparticle. (b) For reverse bias, a pair is broken in the superconductor, and an electron tunnels to the metal. Energy conservation is assured by the excitation of a quasiparticle. Both processes, (a) and (b), can only take place if $eV > \Delta$.

causes the matrix element to fall off rapidly with $\mathbf{k}_{x,y}$. The transverse (x, y) band structure will thus have only minor effects on the tunnelling spectra [5, 14]. Furthermore, the longitudinal (z) band structure $\partial k_z/\partial \xi_{\mathbf{k}}$ cancels with the group velocity term $\partial \xi_{\mathbf{k}}/\partial k_z$ in $|T_{\mathbf{k}}|^2$, when transforming the sum over k_z into an integral over energy. As a result, the single-particle band structure is suppressed in the tunnelling spectra [4, 5, 15]. The situation is more complicated for tunnelling between electron states (in a metal) and quasiparticle states (in a superconductor), see Fig. 3.2. In that case the BCS quasiparticle DOS is present in $\mathrm{d}I(V)/\mathrm{d}V$ spectra, but the single-electron DOS is not.

The cancellation of the longitudinal group velocity by the longitudinal band structure has the counterintuitive result that tunnelling perpendicularly into practically two-dimensional (2D) electronic states is possible. Indeed, though in this case the group velocity approaches zero, the longitudinal DOS becomes large. Experimentally, tunnelling into 2D electronic states has been demonstrated by experiments on surface states on Cu(111) [16].

The suppression of transverse (in-plane) band structure effects on the tunnelling spectra as described above, is not valid for the copper-oxide superconductors treated in this thesis. One of their peculiarities is their highly 2D structure, practically without dispersion perpendicular to the planes. In other words, the longitudinal energy ε_z can be considered as constant, excluding any strong $\mathbf{k}$-dependence of $D(\varepsilon_z)$. This leads to the conclusion that all wave vectors in the Brillouin zone can contribute to the tunneling current, and that the tunnelling conductance of layered (2D) materials *is* sensitive to features in the

transverse band structure [11, 14]. Furthermore, because of the cancellation of the longitudinal band structure, the sum in Eq. 3.10 can be restricted to $\mathbf{k}_{x,y}$. These observations will help us to simulate and analyse tunnelling spectra in Chapter 4.

References

[1] S. Gasiorowicz, *Quantum Physics* (John Wiley & Sons, Inc., Singapore, 1974).

[2] G. D. Mahan, *Many-Particle Physics*, 2nd. ed. (Plenum Press, New York, 1983).

[3] J. Bardeen, Phys. Rev. Lett. **6**, 57 (1961).

[4] W. A. Harrison, Phys. Rev. **123**, 85 (1961).

[5] E. L. Wolf, *Principles of Electron Tunneling Spectroscopy* (Oxford University Press, New York, 1985).

[6] J. Tersoff and D. R. Hamann, Phys. Rev. Lett. **50**, 1998 (1983).

[7] C. J. Chen, Phys. Rev. Lett. **65**, 448 (1990).

[8] C. J. Chen, Phys. Rev. B **42**, 8841 (1990).

[9] H.-J. Güntherodt and R. Wiesendanger, *Scanning Tunneling Microscopy* (Springer-Verlag, Berlin, 1993), Vol. I-III.

[10] W. A. Hofer, A. J. Fisher, R. A. Wolkow, and P. Grütter, Phys. Rev. Lett. **87**, 236104 (2001).

[11] M. Franz and Z. Tešanović, Phys. Rev. B **60**, 3581 (1999).

[12] I. Giaever, Phys. Rev. Lett. **5**, 147 (1960).

[13] M. Tinkham, *Introduction to Superconductivity*, 2nd. ed. (McGraw-Hill, New York, 1996).

[14] J. Y. T. Wei, C. C. Tsuei, P. J. M. van Bentum, Q. Xiong, C. W. Chu, and M. K. Wu, Phys. Rev. B **57**, 3650 (1998).

[15] C. B. Duke, *Tunneling in Solids* (Academic Press, New York, 1969).

[16] M. F. Crommie, C. P. Lutz, and D. M. Eigler, Nature **363**, 524 (1993).

Chapter 4

Short Lifetime of Sup-Gap Quasiparticles and k-Independent Tunnelling Matrix Elements in High-T_c Superconductors

4.1 Introduction

Since scanning tunnelling spectroscopy gives access to the local quasiparticle density of states (DOS) with sub-meV resolution, it is an extremely useful tool for the study of high-T_c superconductors (HTSs). Especially on cleaved surfaces of $Bi_2Sr_2CaCu_2O_{8+\delta}$ (BSCCO) single crystals, a rich set of experimental data has been obtained indeed. These data have lead to a better understanding of the gap size [1–3], of temperature and doping dependence of the gap [4–10], of the electronic nature of vortex cores [11–14], and of defects and impurities [15–17].

On the other hand, little has been done to extract information from tunnelling spectra about the band structure, the behaviour of the van Hove singularity (vHs) near the Fermi level, and the many-body effects usually contained in the electronic self-energy. These domains have mainly been made accessible by angular resolved photoemission (ARPES) [18]. Tunnelling and ARPES should lead to the same conclusions, where tunnelling spectroscopy benefits from higher energy resolution, and ARPES from its high resolution in k-space. An analysis of tunnelling spectra in terms of band structure and electronic self-energies is therefore a useful complement to ARPES data, and helpful to identify probe-independent, intrinsic properties of HTSs.

The interpretation of tunnelling spectra of HTSs is rather complex, however, as demonstrated by the large variety of models proposed for it. The effects of low tunnelling barrier height and large energy gaps have been considered [19], as well as inelastic tunnelling [20, 21], directional selectivity of the tunnelling matrix element [21–24], band structure effects like van Hove singularities [22, 23, 25], resonant tunnelling [26], and energy-dependent superconducting gap functions [27, 28].

The main phenomena in low-temperature tunnelling spectra that are not covered by sim-

ple BCS d-wave analysis (see Fig. 4.1), are the large size of the coherence peaks, the role of the vHs, and the dip-hump structure at an energy of about twice the superconducting gap. This dip-hump structure is more pronounced at negative than at positive bias.

Apart from these still not well understood phenomena, the role of tunnelling matrix elements should be clarified. Based on band structure calculations [29–31], one may expect them to modify the tunnelling spectra with respect to the constant matrix-element expectation. A proper modelling of tunnelling spectra can shed light on this problem.

In this study, the vHs is identified at negative bias in the tunnelling spectra, at an energy depending on hole doping. In fact, tunnelling spectra for different hole doping levels have a background which is in excellent agreement with a broadened single-particle band structure. This broadening is in apparent contradiction with the sharpness of the quasiparticle coherence peaks, in a similar way as has been observed in ARPES measurements [18, 32]. It implies a sup-gap quasiparticle lifetime about two orders of magnitude smaller than the lifetime of the quasiparticles forming the coherence peaks. A simple model describing quasiparticle interaction with a collective, bosonic mode [33] is shown to give an accurate description of the broadened band structure, the peak height and the dip-hump above the gap. Using a proper model for the background in the tunnelling spectra, it is demonstrated that the tunnelling matrix elements have only a minor dependence on the in-plane wave vector.

4.2 Model

The starting point for our analysis is the standard tunnelling Hamiltonian treatment [34, 35] for tunnelling between a normal metal (free electrons) and a superconductor. As shown in chapter 3, this leads to the tunnelling conductance [24, 35]

$$\frac{\mathrm{d}I(V)}{\mathrm{d}V} = \int_{-\infty}^{\infty} \frac{\mathrm{d}\omega}{2\pi} \left(-\frac{\partial f(\omega - eV)}{\partial eV} \right) \sum_{\mathbf{k}} |T_{\mathbf{k}}|^2 A_S(\mathbf{k}, \omega). \tag{4.1}$$

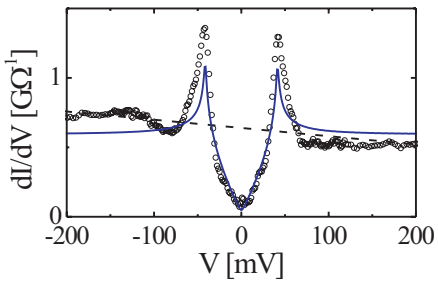

Figure 4.1: Circles: scanning tunnelling spectrum of optimally doped BSCCO ($T_c = 92.2$ K) at 4.2 K [4]. The straight dashed line corresponds to an estimated background. The area under the dashed line is equal to the area under the spectrum to within a few percent (see text). Continuous line: BCS DOS for an order parameter with d-wave symmetry, and assuming a free electron gas in the normal state.

Here $f(\omega - eV)$ is the Fermi-Dirac distribution function, $T_{\mathbf{k}}$ the tunnelling matrix element, and A_S the spectral function of the superconductor. At low temperature $[-\partial f(\omega - eV)/\partial eV]$ can be replaced by a δ-function ($k_B T < 1$ meV, this corresponds to negligible smearing in our results). The matrix element $|T_{\mathbf{k}}|^2$ is, to a first approximation, proportional to the group velocity [36, 37].

Following BCS theory, the spectral function can be written

$$A_S(\mathbf{k}, \omega) = 2\pi[u_k^2 \delta(\omega - E_k) + v_k^2 \delta(\omega + E_k)], \tag{4.2}$$

with a quasiparticle energy $E_k = \sqrt{\xi_{\mathbf{k}}^2 + \Delta_{\mathbf{k}}^2}$, a d-wave gap $\Delta_{\mathbf{k}} = \Delta_0(\cos k_x - \cos k_y)/2$, and the coherence factors $u_k^2 = (1 + \xi_{\mathbf{k}}/E_{\mathbf{k}})/2$ and $v_k^2 = (1 - \xi_{\mathbf{k}}/E_{\mathbf{k}})/2$ [35].

The single-particle energies $\xi_{\mathbf{k}}$ are calculated using the 8-band tight-binding fit of Andersen *et al.* [29, 30] to an LDA calculation for the odd bands in $YBa_2Cu_3O_7$ (YBCO). Here odd and even refer to the odd and even combinations of the wave functions in the two CuO_2 layers of the YBCO unit cell. One of the odd bands has a vHs close to the Fermi level, with correspondingly high DOS. In the energy range considered here, the even bands only have a minor contribution to the DOS. The hole doping of the sample is simulated by shifting the Fermi level ε_F. This is the only parameter which is varied with respect to the parameters of Andersen *et al.*. Though the fit is originally designed for YBCO, it is a generic description of the 2-dimensional band structure of the CuO_2 planes in HTSs, within the range of -2 to 2 eV around the Fermi level [29, 30]. Nevertheless, because of its higher anisotropy, BSCCO has a smaller bi-layer splitting between the odd and the even bands than YBCO, $\lessapprox 100$ meV for the bands crossing the Fermi level [38–43]. We assume that the bi-layer splitting does not have an important effect on the tunnelling spectra. Indications that this assumption is justified, are (i) the large energy broadening of the independent-particle band structure as demonstrated below (over 250 meV, much larger than the bi-layer splitting) and (ii) the correspondence between the experimentally determined $p - T_c$ diagram and the one based on simulations including only the odd band (see Fig. 4.3).

The bare single-particle DOS has a sharp vHs just below the Fermi level. In the superconducting state, it is either clearly separated from the coherence peaks, or – when it is closer to the Fermi level – integrated in the peaks. The former case is clearly not consistent with experiment. In the latter case the total spectral weight in the energy window of Fig. 4.1 should be increased by 20 to 30% with respect to an approximately constant DOS. However, the total spectral weight of the experimental spectrum equals the area under the extrapolated, *flat* background to within a few percent. We therefore conclude that the vHs must be (almost) completely suppressed in the tunnelling spectra. Correspondingly, using a similar analysis of spectra normalised to the background, Cren *et al.* [28] have shown that all additional spectral weight in the coherence peaks (with respect to a BCS d-wave fit) is due to a rearrangement of spectral weight from the dips (at about $\pm 2\Delta_0$) to the peaks, and thus is not directly related to the vHs.

The experimental spectra discussed below were taken with the tunnelling direction perpendicular to the CuO_2 planes of the HTS. It has been demonstrated previously that in such experiments the vHs of the two-dimensional band structure should show up in tunnelling spectra [22]. Furthermore, the group velocity in the tunnelling matrix element cancels the effects of the longitudinal band structure (i.e. in the tunnelling direction, see

chapter 3) [24, 37]. The main question is now how the vHs is suppressed (smeared out), without affecting the sharpness of the coherence peaks.

In the following phenomenological analysis, we first demonstrate that the background in the tunnelling spectra indeed corresponds to a broadened single-particle DOS, using model 1 below. The main advantage of model 1 is its extreme simplicity, while it still gives a close correspondence to the background in experimental tunnelling spectra. After a comparison to the experimental data, we will discuss the mechanism that may be responsible for this. To this end we employ a model for describing the interaction of the quasiparticles with a collective mode, model 2 [33]. At first, we assume the matrix element in Eq. 4.1 to be constant.

Model 1. We rewrite the momentum dependence of the spectral function as $A_S(\mathbf{k},\omega) = A_S(\xi_\mathbf{k},\Delta_\mathbf{k},\omega)$. The separate dependence on $\xi_\mathbf{k}$ and $\Delta_\mathbf{k}$ can only be correct if there is no random scattering in $\mathbf{k}$-space. To broaden the single-particle band structure we convolute this spectral function with a Lorentzian $g(\xi)$, of width Γ, in the following way:

$$\tilde{A}_S(\mathbf{k},\omega) = \int g(\tilde{\xi}-\xi_\mathbf{k})A_S(\tilde{\xi},\Delta_\mathbf{k},\omega)\mathrm{d}\tilde{\xi}. \tag{4.3}$$

Because of the δ-functions in A_S (Eq. 4.2) the convolution is easily done analytically:

$$\begin{aligned}\tilde{A}_S(\mathbf{k},\omega) =& \pi[\frac{|\omega|}{\sqrt{\omega^2-\Delta_\mathbf{k}^2}}+\mathrm{sgn}(\omega)]g(\xi_\mathbf{k}-\sqrt{\omega^2-\Delta_\mathbf{k}^2}\,)\,+\\ & \pi[\frac{|\omega|}{\sqrt{\omega^2-\Delta_\mathbf{k}^2}}-\mathrm{sgn}(\omega)]g(\xi_\mathbf{k}+\sqrt{\omega^2-\Delta_\mathbf{k}^2}\,),\ |\omega|>|\Delta_\mathbf{k}|.\end{aligned} \tag{4.4}$$

[To avoid infinite values of the spectral function, it is broadened by taking the real part of the complex $\tilde{A}_S(\mathbf{k},\omega-i\eta)$, with $\eta = 1$ meV (similar to the Dynes DOS [44]).] To calculate the $\mathrm{d}I/\mathrm{d}V$ spectra, the new spectral function $\tilde{A}_S(\mathbf{k},\omega)$, with the band structure broadened over Γ, is inserted in Eq. 4.1. The only adjustable parameters are the width of the Lorentzian $g(\xi)$, the Fermi level ε_F (as explained above), and the maximum gap Δ_0.

Model 2. A model describing interaction with a collective mode [33] allows us to verify whether such a mode can be responsible for the large smearing of the sup-gap quasiparticles in tunnelling spectra. It can also cause a transfer of spectral weight from the dips at $\pm\sim 2\Delta_0$ to the coherence peaks, explaining their unusual spectral weight. The mode can have various origins, though several groups claim a relation to (π,π) resonance observed in neutron scattering experiments, implying collective spin excitations [45–52]. The model used here was originally designed for describing ARPES data, on which good fits were obtained [33].

In this model the spectral function of the superconductor is given by the strong-coupling expression [53, 54]

$$A_S(\mathbf{k},\omega) = \frac{1}{\pi}\mathrm{Im}\frac{Z\omega+\xi_\mathbf{k}}{Z^2(\omega^2-\Delta_\mathbf{k}^2)-\xi_\mathbf{k}^2}, \tag{4.5}$$

with $Z(\omega) = 1-\Sigma(\omega)/\omega$, and $\Sigma(\omega)$ the complex self-energy. The interaction with a collective mode results in a large imaginary part of the self-energy Σ'' above the energy

of the dip, leading to a large broadening of structures at high bias. Near the Fermi energy, however, Σ'' is small. Here we just reproduce the equations for the imaginary and real parts of the self-energy, based on first-order perturbation theory, and refer to Ref. [33] for more details.

$$-\Sigma''(\omega) = \begin{cases} \Gamma_0 N(|\omega|) + \Gamma_1 N(|\omega| - \Omega_0), & |\omega| > \Omega_0 + \Delta, \\ \Gamma_0 N(|\omega|), & \Delta < |\omega| < \Omega_0 + \Delta, \\ 0, & |\omega| < \Delta, \end{cases} \tag{4.6}$$

where $N(\omega) = \omega/\sqrt{\omega^2 - \Delta^2}$ is the BCS density of states, Ω_0 is the energy of the collective mode, and all $\mathbf{k}$-dependence enters via the gap function $\Delta = \Delta_{\mathbf{k}}$. The Γ_0 term leads to an (artificial) damping of the coherence peaks, Γ_1 is the coupling between the quasiparticles and the collective mode. The real part of the self-energy follows analytically via Kramers-Kronig transformation. For this derivation the s-wave BCS DOS is taken for $N(\omega)$, assuming that the result for the d-wave case will be similar.

$$\begin{aligned} \pi\Sigma'(\omega) =& \Gamma_0 N(-\omega) \ln[|-\omega + \sqrt{\omega^2 - \Delta^2}|/\Delta] + \\ & \Gamma_1 N(\Omega_0 - \omega) \ln[|\Omega_0 - \omega + \sqrt{(\omega - \Omega_0)^2 - \Delta^2}|/\Delta] \\ & - \{\omega \to -\omega\}. \end{aligned} \tag{4.7}$$

Once the self-energy is determined, the spectral function (Eq. 4.5) is directly inserted into Eq. 4.1.

4.3 Results

In Fig. 4.2 we show calculated spectra based on model 1 compared to experimental data for different hole doping levels, ranging from overdoped to underdoped [4]. To obtain a reasonable agreement with the measured tunnelling spectra, the broadening Γ should be larger than 200 meV. The Fermi level has been adjusted to match the asymmetric background. As far as the background is concerned, the correspondence between calculated and measured spectra is remarkably good. The V-shaped low-bias parts of the spectra agree as well. The height of the peaks and the dip are not reproduced correctly, however. We will come back to this later. The parameters giving the best agreement between calculated and measured data for the different samples are given in Table 4.1. The typical value of Γ of 250 meV is only slightly smaller than the 300 meV extracted from ARPES data for the imaginary part of the self-energy [32]. For the underdoped sample the slope of the background is considerably larger, which can – within this model – only be reproduced by a smaller Γ, of 150 meV. Deviations from a rigid band description (as has been used here) could be responsible for the different Γ in the underdoped sample.

From the Fermi energies needed to simulate the background, the band filling and the hole concentration p of the odd band can be derived. One can plot T_c as a function of the thus obtained p, and compare it to a generic $T_c - p$ relation [55, 56]. Taking into account that the effect of doping is simulated by a rigid-band shift of the Fermi level, the correspondence in Fig. 4.3 is surprisingly good. This strengthens our conclusion that

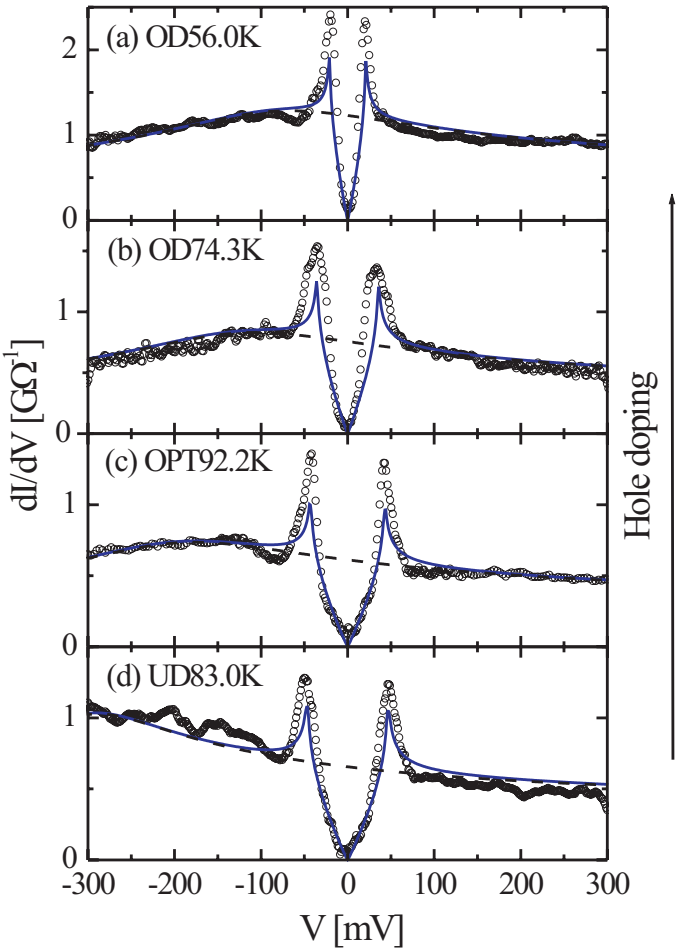

Figure 4.2: Experimental (circles) [4] and calculated (continuous lines) spectra for two overdoped samples (T_c of 56.0 and 74.3 K), for an optimally doped sample ($T_c = 92.2$ K), and for an underdoped sample ($T_c = 83.0$ K). The dashed lines correspond to the calculated spectra in the normal state ($\Delta_0 = 0$). The calculated spectra have been normalised to obtain the same integrated spectral weight as the experimental data, over the energy range depicted here.

the asymmetric background in the tunnelling spectra is due to a broadened vHs, which shifts away from the Fermi level with underdoping.

T_c [K]	Δ_0 [meV]	Γ [meV]	ε_{vHs} [meV]
56.0	21±2	250±40	-100±30
74.3	36	250	-140
92.2	44	250	-210
83.0	49	150	-310

Table 4.1: Parameters for the calculated spectra in Fig. 4.2: The gap Δ_0, the broadening of the band structure Γ, and the energy of the vHs ε_{vHs} with respect to the Fermi level. The latter value is determined by the Fermi energy.

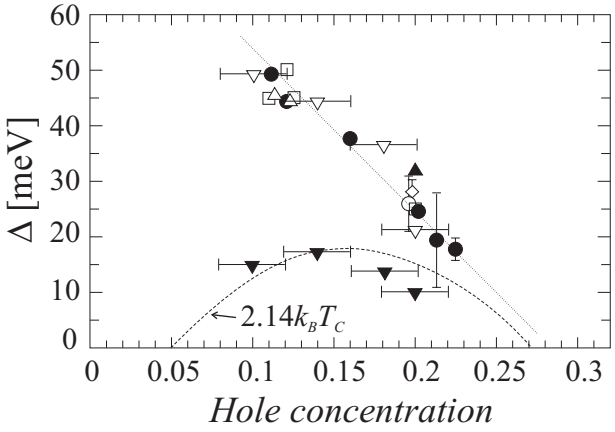

Figure 4.3: Doping (p) dependence of the gap (Δ), as compiled from various tunnelling and photoemission measurements [6]. We have added the open triangles ($\triangledown$), corresponding to the data points (p, Δ) derived from our simulations. p and Δ follow from the Fermi level in the odd band and the gap Δ_0, respectively. The filled triangles ($\blacktriangledown$) compare the $T_c - p$ relation based on our simulations, to the generic $T_c - p$ relation (the bell-shaped curve) for HTSs [55, 56].

The broadened normal state dispersion is clearly visible in the calculated spectral functions in Fig. 4.4. It is very similar to the dispersion of the hump in ARPES spectra [45, 57]. The broadened normal state, in coexistence with sharp coherence peaks, is in agreement with ARPES too.

To improve the correspondence to the experimental data, we calculate the $\mathrm{d}I/\mathrm{d}V$ spectrum using model 2, for interaction with a collective (bosonic) mode (Eq. 4.5), see Fig. 4.5(a). The Fermi level and the gap width are the same as for the optimally doped sample in Fig. 4.2. The (rather artificial) damping of the coherence peaks Γ_0 is 20 meV, the strength of the mode Γ_1 is 100 meV, and the energy of the mode Ω_0 is set to $\Delta_{\mathbf{k}}$ [33]. Nevertheless, including this self-energy in a BCS d-wave calculation, all features of the spectra are well reproduced: (i) the dip-hump structure, (ii) the height of the coherence peaks, (iii) the asymmetric background made of a broadened vHs and (iv) the shape of the spectra at low bias.

The latter point deserves special attention. In the calculations above, the tunnelling matrix element $T_{\mathbf{k}}$ was assumed to be a constant. However, it has been argued that the most probable channel for tunnelling into the low-energy states is Cu s orbital [29–31]. This implies that the tunnelling probability for states along the (π,π) direction – i.e. along the nodes of the gap function – is strongly suppressed. We explicitly calculated this matrix element, which corresponds to the participation of the Cu s orbital to the band at the Fermi level. This leads to similar results as a matrix element $T_{\mathbf{k}} \propto [\cos(k_x) - \cos(k_y)]$ [29–31], and as a matrix element based on the out-of-plane group velocity in a three-dimensional extension of the 8-band model (by including a term $2t_z \cos(k_z)$ in the energy of the Cu s orbital). The resulting spectrum is shown in Fig. 4.5(b). The agreement with the experimental data, especially around zero bias, is worse than before, suggesting strongly that for low energies a constant matrix element is much closer to the actual situation than a strongly $\mathbf{k}$-dependent one.

It is rather easy to perform a more complete calculation of the tunnelling matrix elements

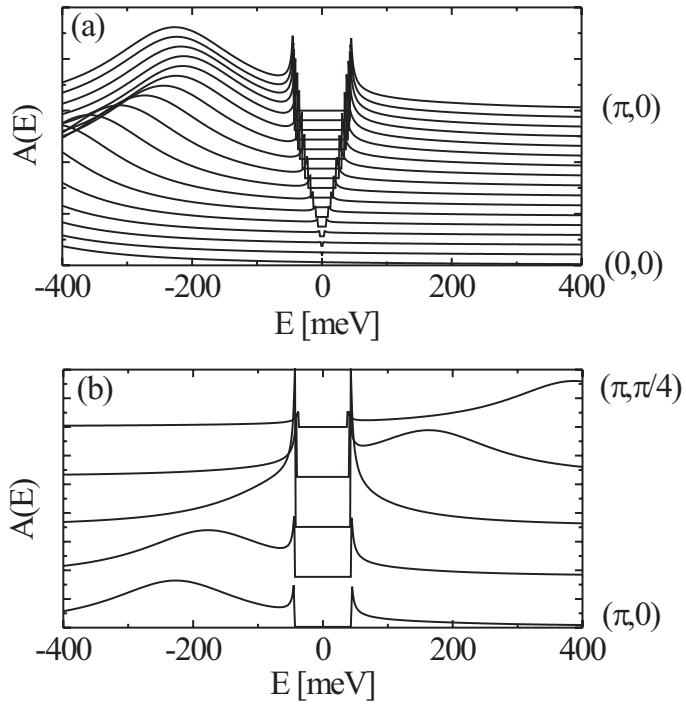

Figure 4.4: Spectral functions based on Eq. 4.4, along (a) the (0,0)-(π,0) and (b) the (π,0)-(π,π/4) directions in the Brillouin zone.

(i.e. not only based on tunnelling via the Cu s orbital), deriving them from the bilayer splitting between the odd and the even band [30]: $|T_{\mathbf{k}}|^2 \propto |\xi_{even}(\mathbf{k}) - \xi_{odd}(\mathbf{k})|$. The resulting spectrum is indicated as the dashed line in Fig. 4.5(a). The matrix elements only enhance the asymmetry in the background. Near zero bias, it is almost impossible to distinguish it from the spectrum based on a constant matrix element. Therefore, based on comparison to both experimental and theoretical data, we conclude that a constant matrix element is a good approximation.

4.4 Discussion

The main result of our analysis is the extreme broadening of the single-particle band structure, while the quasiparticle coherence peaks remain sharp. The broadening can have various origins. A first possibility to be considered, is scattering of electrons in the tunnelling process. However, this is hard to reconcile with presence of sharp coherence peaks at energies close to the broadened vHs.

Another reason for the broadening of the single-particle band structure could be the small, though finite energy dispersion in the direction perpendicular to the CuO_2 planes. However, the broadening required here is a factor 2 to 3 larger than the dispersion as determined by ab-initio band structure calculations [38–41] and recent photoemission

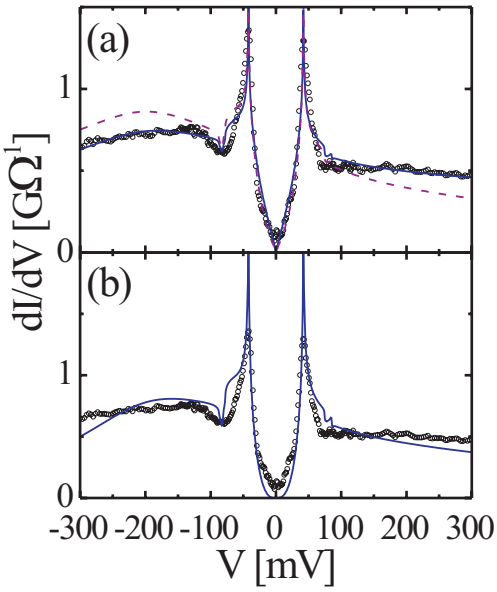

Figure 4.5: (a) Comparison between experimental data for the optimally doped sample (T_c = 92.2 K) and the tunnelling spectra calculated with a model for describing interaction with a collective mode [33]. The tunnelling matrix element is set to a constant (continuous line). The dashed line is a simulation taking into account the matrix elements derived from the bilayer splitting [30]. (b) As in (a), but with the tunnelling matrix element according to the participation of the Cu s orbital to the band crossing the Fermi level.

experiments [42, 43].

The close correspondence between experimental data and the collective mode calculation (model 2), suggests that the mode is responsible for the short lifetime of sup-gap quasiparticles. This requires some careful investigation of the model. The imaginary part of the self-energy is dependent on the DOS $N(\omega)$ according to: $\Sigma''(\omega) = \Gamma N(\omega + \Omega_0)$ for $|\omega| > \Omega_0$ and $\omega < 0$, and similarly, with $\{\Omega_0 \rightarrow -\Omega_0\}$, for $\omega > 0$ [53, 54]. One would thus expect a peak in the DOS to lead to a peak in the imaginary part of the self-energy. A first order calculation using the CuO_2-plane band structure would lead to a dip-hump structure at the energy of the vHs plus the energy of the mode ($|\varepsilon_{vHs}| + \Omega_0$, at negative bias). This is also the case if the resonance is centred around a wave vector of (π, π) [45–52], which in fact highlights the region in k-space near the vHs (we checked this numerically using the model of Ref. [46]). Our results clearly indicate the presence of the (broadened) vHs at negative bias for different doping levels, but dip-hump structures are only observed next to the coherence peaks, *below* the energy of the vHs.

The reason why the model of Eqs. 4.5-4.7 still works, is that the quasiparticle DOS used to calculate the self-energy is the BCS DOS without any band structure features (the normal DOS is constant). It therefore assumes that the vHs is either not there, or already highly suppressed. If the suppression of the vHs is due to the collective mode, a perturbation approach should thus take into account higher-order contributions. For electron-phonon interactions, higher order contributions are smaller by at least a factor

$\sqrt{m/M}$ (m is the electron mass, M the mass of the ions in the lattice), and are negligible (Migdal's theorem) [53, 54]. This does not seem to be consistent with our results.

Resuming, a first-order calculation of the collective mode self-energy will not give a correct result unless a *broadened* DOS is inserted. In this case, the standard BCS s-wave DOS is similar to the actual quasiparticle DOS as far as sharp features (the coherence peaks) are concerned. This leads to the agreement with the experimental data in Fig. 4.5(a). The disagreement in the shape of the dip (in the calculated spectrum it is too narrow) probably follows from the finite width of the mode, not taken into account in model 2.

Apart from that, the correspondence is very good, and indicates that the quasiparticle DOS results from a BCS d-wave-like state in combination with a collective mode. The collective mode does not only lead to the large coherence peaks and the dip-hump structure, but also to an extremely short lifetime of the sup-gap quasiparticles. It is worth noting that the $\mathrm{d}I/\mathrm{d}V$ spectra above T_c, with or without pseudogap (see, e.g. Refs. [3, 4]) do not show a vHs either. Thermal broadening is more important there, but by far not sufficient: k_BT at room temperature is still an order of magnitude smaller than the broadening of the band structure discussed above.

A mode related to the (π, π) neutron resonance [45–52] may be consistent with our conclusions, but would require a rather large coupling to have an important effect on the spectral functions [58], even the more since the coupling cannot be enhanced by a *sharp* vHs [46]. It is worth noting that the broadening of the vHs implies that it does not play an important role in enhancing the T_c either.

An other important result of this work is the correspondence between experimental data and spectra calculated with a constant matrix element. On the assumption that c-axis tunnelling into low-energy states occurs via the Cu s orbital, one would expect tunnelling matrix elements to suppress spectral weight near the nodes of the gap function [29–31], giving a U-shape to the low-bias part of the spectra. From Fig. 4.5, we conclude that this is not the case. A constant matrix element matches the data much better.

There are several possibilities to explain why this is the case. The $\mathbf{k}$-dependence of the matrix element may be more complicated due to interference of the contributions of different atoms to the tunnel current. Since the wave function at neighbouring atoms differs by a phase vector $\exp(\pm ik)$ according to Bloch's theorem, wave vectors k_x, k_y with values near π will lead to destructive interference [59]. For the particular Fermi surface of HTSs, this has an effect opposing the matrix element based on tunnelling via the Cu s orbital, as discussed above. However, it also introduces a background which is much more asymmetric (states with low wave vectors, further below the Fermi level, are favoured) than what is observed experimentally. We have not managed to obtain a satisfactory simulation including this effect.

A more likely explanation is that one should include *all* interplane hopping integrals to obtain reasonable matrix elements, and not only those related to the Cu s. The interplane hopping integrals between the oxygen $p_{x,y}$ and between the Cu d orbitals of neighbouring CuO_2 planes contribute as well [29, 30]. Though they have smaller interplane hopping integrals than the Cu s, the band at the Fermi level has much more O $p_{x,y}$ and Cu d than Cu s character, making the former two more important close to the Fermi level. A closer

look at the eight-band model for the CuO_2 plane [29, 30] reveals that the interplane hopping integral does have a minimum along the (π, π) direction, as has been verified by ARPES experiments on BSCCO [42, 43]. However, the difference between the maximum and minimum tunnelling matrix elements near the Fermi level is only a factor $2 \sim 3$ (see Fig. 7 of Ref. [30]). Thus, in contrast to what is often assumed, the tunnelling matrix elements along the (π, π) direction do *not* go to zero.

4.5 Conclusion

We have reproduced the background in tunnelling spectra on BSCCO, using a broadened, realistic band structure. The lifetime of sup-gap quasiparticles in BSCCO is found to be extremely short. The coherence peaks, however, remain sharp, in agreement with ARPES results.

The vHs is identified in the spectra, between about 100 and 310 meV below the Fermi level, depending on the hole doping. As a result of the short quasiparticle lifetime, the vHs is heavily broadened. The broadening can be explained by interaction of the quasiparticles with a collective mode, using a model previously employed to describe photoemission data [33]. The mode can also be held responsible for the large size of the coherence peaks and the dip-hump structure.

However, the absence of a dip near the energy of the (broadened) vHs indicates that higher order perturbations should be taken into account to properly describe the effect of the collective mode on the DOS.

Finally, the shape of the spectra at low-bias voltage demonstrates that the tunnelling matrix element does not have a strong dependence on the (in-plane) wave vector $\mathbf{k}$. Tunnelling spectroscopy therefore probes states along the whole Fermi surface, including the diagonals of the Brillouin zone.

References

[1] Ch. Renner, B. Revaz, J.-Y. Genoud, and Ø. Fischer, J. Low Temp. Phys. **105**, 1083 (1994).

[2] E. L. Wolf, A. Chang, Z. Y. Rong, Y. M. Ivanchenko, and F. Lu, J. Supercond. **7**, 355 (1994).

[3] Ch. Renner and Ø. Fischer, Phys. Rev. B **51**, 9208 (1995).

[4] Ch. Renner, B. Revaz, J.-Y. Genoud, K. Kadowaki, and Ø. Fischer, Phys. Rev. Lett. **80**, 149 (1998).

[5] Y. DeWilde, N. Miyakawa, P. Guptasarma, M. Iavarone, L. Ozyuzer, J. F. Zasadzinski, P. Romano, D. G. Hinks, C. Kendziora, G. W. Crabtree, and K. E. Gray, Phys. Rev. Lett. **80**, 153 (1998).

[6] N. Miyakawa, P. Guptasarma, J. F. Zasadzinski, D. G. Hinks, and K. E. Gray, Phys. Rev. Lett. **80**, 157 (1998).

[7] S. Kaneko, N. Nishida, K. Mochiku, and K. Kadowaki, Physica C **298**, 105 (1998).

[8] S. Matsuura, T. Taneda, W. Yamaguchi, H. Sugawara, T. Hasegawa, and K. Kitazawa, Physica C **300**, 26 (1998).

[9] N. Miyakawa, J. F. Zasadzinski, L. Ozyuzer, P. Guptasarma, D. G. Hinks, C. Kendziora, and K. E. Gray, Phys. Rev. Lett. **83**, 1018 (1999).

[10] A. Matsuda, S. Sugita, and T. Watanabe, Phys. Rev. B **60**, 1377 (1999).

[11] Ch. Renner, B. Revaz, K. Kadowaki, I. Maggio-Aprile, and Ø. Fischer, Phys. Rev. Lett. **80**, 3606 (1998).

[12] B. W. Hoogenboom, Ch. Renner, B. Revaz, I. Maggio-Aprile, and Ø. Fischer, Physica C **332**, 440 (2000).

[13] S. H. Pan, E. W. Hudson, A. K. Gupta, K.-W. Ng, H. Eisaki, S. Uchida, and J. C. Davis, Phys. Rev. Lett. **85**, 1536 (2000).

[14] B. W. Hoogenboom, K. Kadowaki, B. Revaz, M. Li, Ch. Renner, and Ø. Fischer, Phys. Rev. Lett. **87**, 267001 (2001).

[15] A. Yazdani, C. M. Howald, C. P. Lutz, A. Kapitulnik, and D. M. Eigler, Phys. Rev. Lett. **83**, 176 (1999).

[16] E. W. Hudson, S. H. Pan, A. K. Gupta, K.-W. Ng., and J. C. Davis, Science **285**, 88 (1999).

[17] S. H. Pan, E. W. Hudson, K. M. Lang, H. Eisaki, S. Uchida, and J. C. Davis, Nature **403**, 746 (2000).

[18] Z.-X. Shen and D. S. Dessau, Phys. Rep. **253**, 1 (1995).

[19] J. R. Kirtley, Phys. Rev. B **41**, 7201 (1990).

[20] J. R. Kirtley and D. J. Scalapino, Phys. Rev. Lett. **65**, 798 (1990).

[21] K. Kouznetsov and L. Coffey, Phys. Rev. B **54**, 3617 (1996).

[22] J. Y. T. Wei, C. C. Tsuei, P. J. M. van Bentum, Q. Xiong, C. W. Chu, and M. K. Wu, Phys. Rev. B **57**, 3650 (1998).

[23] Z. Yusof, J. F. Zasadzinski, L. Coffey, and N. Miyakawa, Phys. Rev. B **58**, 514 (1998).

[24] M. Franz and Z. Tešanović, Phys. Rev. B **60**, 3581 (1999).

[25] J. Bok and J. Bouvier, Physica C **274**, 1 (1997).

[26] J. Halbritter, J. Supercond. **11**, 231 (1998).

[27] J. E. Hirsch, Phys. Rev. B **59**, 11962 (1999).

[28] T. Cren, D. Roditchev, W. Sacks, and J. Klein, Europhys. Lett. **52**, 203 (2000).

[29] O. K. Andersen, O. Jepsen, A. I. Liechtenstein, and I. I. Mazin, Phys. Rev. B **49**, 4145 (1994).

[30] O. K. Andersen, A. I. Liechtenstein, O. Jepsen, and F. Paulsen, J. Phys. Chem. Solids **56**, 1573 (1995).

[31] T. Xiang and J. M. Wheatley, Phys. Rev. Lett. **77**, 4632 (1996).

[32] M. R. Norman, H. Ding, H. Fretwell, M. Randeria, and J. C. Campuzano, Phys. Rev. B **60**, 7585 (1999).

[33] M. R. Norman and H. Ding, Phys. Rev. B **57**, R11089 (1998).

[34] J. Bardeen, Phys. Rev. Lett. **6**, 57 (1961).

[35] G. D. Mahan, *Many-Particle Physics*, 2nd. ed. (Plenum Press, New York, 1983).

[36] E. L. Wolf, *Principles of Electron Tunneling Spectroscopy* (Oxford University Press, New York, 1985).

[37] W. A. Harrison, Phys. Rev. **123**, 85 (1961).

[38] M. S. Hybertsen and L. F. Mattheiss, Phys. Rev. Lett. **60**, 1661 (1988).

[39] H. Krakauer and W. E. Pickett, Phys. Rev. Lett. **60**, 1665 (1988).

[40] S. Massidda, J. Yu, and A. J. Freeman, Physica C **152**, 251 (1988).

[41] L. F. Mattheiss and D. R. Hamann, Phys. Rev. B. **38**, 5012 (1988).

[42] D. L. Feng, N. P. Armitage, D. H. Lu, A. Damascelli, J. P. Hu, P. Bogdanov, A. Lanzara, F. Ronning, K. M. Shen, H. Eisaki, C. Kim, Z.-X. Shen, J. i. Shimoyama, and K. Kishio, Phys. Rev. Lett. **86**, 5550 (2001).

[43] Y.-D. Chuang, A. D. Gromko, A. Fedorov, Y. Aiura, K. Oka, Y. Ando, H. Eisaki, S. I. Uchida, and D. S. Dessau, Phys. Rev. Lett. **87**, 117002 (2001).

[44] R. C. Dynes, V. Narayanamurti, and J. P. Garno, Phys. Rev. Lett. **41**, 1509 (1978).

[45] J. C. Campuzano, H. Ding, M. R. Norman, H. M. Fretwell, M. Randeria, A. Kaminski, J. Mesot, T. Takeuchi, T. Sato, T. Yokoya, T. Takahashi, T. Mochiku, K. Kadowaki, P. Guptasarma, D. G. Hinks, Z. Konstantinovic, Z. Z. Li, and H. Raffy, Phys. Rev. Lett. **83**, 3709 (1999).

[46] M. Eschrig and M. R. Norman, Phys. Rev. Lett. **85**, 3261 (2000).

[47] T. Dahm, D. Manske, and L. Tewordt, Phys. Rev. B **58**, 12454 (1998).

[48] Ar. Abanov and A. V. Chubukov, Phys. Rev. B **61**, R9241 (2000).

[49] J.-X. Li, C.-Y. Mou, and T. K. Lee, Phys. Rev. B **62**, 640 (2000).

[50] J. F. Zasadzinski, L. Ozyuzer, N. Miyakawa, K. E. Gray, D. G. Hinks, and C. Kendziora, Phys. Rev. Lett. **87**, 67005 (2001).

[51] D. Manske, I. Eremin, and K. H. Bennemann, Phys. Rev. Lett. **87**, 177005 (2001).

[52] J. D. Lee and A. Fujimori, Phys. Rev. Lett. **87**, 167008 (2001).

[53] R. D. Parks, *Superconductivity* (Marcel Dekker, New York, 1969), Vol. 1.

[54] J. R. Schrieffer, *Theory of Superconductivity* (W. A. Benjamin, New York, 1964).

[55] M. R. Presland, J. L. Tallon, R. G. Buckley, R. S. Liu, and N. E. Flower, Physica C **176**, 95 (1991).

[56] J. L. Tallon, C. Bernard, H. Shaked, R. L. Hitterman, and J. D. Jorgensen, Phys. Rev. B **51**, 12911 (1995).

[57] M. R. Norman, H. Ding, J. C. Campuzano, T. Takeuchi, M. Randeria, T. Yokoya, T. Takahashi, T. Mochiku, and K. Kadowaki, Phys. Rev. Lett. **79**, 3506 (1997).

[58] H.-Y. Kee, S. A. Kivelson, and G. Aeppli, cond-mat/0110478.

[59] R. Koops, Ph.D. thesis, University of Groningen, 1992.

Chapter 5

Sample Preparation and Homogeneity

5.1 Introduction

One of the recent developments in condensed matter physics is the observation and quantitative study of electronic inhomogeneity in high-temperature superconductors (HTSs). Early scanning tunnelling microscopy (STM) experiments had shown spatial variations in the quasiparticle local density of $Bi_2Sr_2CaCu_2O_{8+\delta}$ (BSCCO) [1, 2]. However, experiments on *in-situ* cleaved BSCCO crystals demonstrated high spatial reproducibility [3], suggesting that the observed inhomogeneity was due to sample or surface preparation. During the last two years, several STM experiments have again demonstrated disorder in the electronic properties of BSCCO, at surfaces having been exposed to air [4, 5], on samples cleaved *in situ* at room temperature [6], and on samples cleaved in cryogenic vacuum [7, 8]. The disorder typically shows up as variations in the gap size and in the height of the coherence peaks in tunnelling spectra, over distances of a few nanometres on the surface.

The issue of inhomogeneity in HTSs is important for several reasons. First, if inhomogeneity is an intrinsic property of HTSs, it implies a re-interpretation of experiments which only measure an average of the electronic properties of the sample. It may explain, for instance, the correspondence between the spectral function at $(\pi, 0)$ *averaged* over the surface as measured in photoemission experiments, to the *local* density of states in tunnelling spectra [9]. Second, a certain degree of homogeneity is essential for the proper interpretation of STM studies on temperature dependence [10] and energy scaling in vortex cores [11]. Third, it can give information about the oxygen dopant distribution [12, 13], of which little is known so far. And fourth, the main reason why these measurements have caused such an excitement: an inhomogeneity may point at microscopic phase separation, an essential element of several theories for high-T_c superconductivity and for the pseudogap observed above T_c [14–16].

It is thus of extreme importance to investigate whether the observed electronic inhomogeneity is an intrinsic property of HTSs, or whether it is a characteristic of doped copper-oxides which is not essential for high-temperature superconductivity. One can take a first step to answering this question by unambiguously demonstrating whether or not long-range homogeneity can be obtained in HTSs at all. An other important

issue to be addressed is the question why different groups obtain different degrees of inhomogeneity in STM measurements on BSCCO [1–8].

In this study, we confirm that a large degree of homogeneity can be obtained in slightly overdoped BSCCO. In addition to previous detailed characterisation of vacuum tunnelling conditions and of reproducibility of tunnelling spectra by Renner and Fischer [3], we explicitly demonstrate that this homogeneity is obtained with an *atomically sharp* STM tip, and therefore cannot be an artefact resulting from low spatial resolution. Furthermore, our measurements suggest that long-range homogeneity is only obtained on samples with extremely sharp superconducting transition widths (less than 1% of T_c). An apparently small difference in the macroscopic transition width has large consequences on a nanometre scale. This can explain why STM measurements on seemingly similar crystals show such different results.

5.2 Sample preparation

Since it shows to be less difficult to obtain homogeneous samples in the overdoped than in the underdoped regime, we concentrate on slightly overdoped BSCCO single crystals. As-grown samples are annealed under oxygen pressure for at least a week, typically at 500 ^{o}C and 15 bar oxygen pressure [17]. At the end of the annealing period, the sample is rapidly cooled down (several degrees per second) in order to prevent diffusion of oxygen dopants. The transition temperature and width are determined by AC susceptibility measurements, shortly after the annealing procedure. The transition width ΔT_c is defined as the temperature difference between 10 and 90% of the superconducting transition. In Fig. 5.1(a) we show the transition for what we estimate to be a highly homogeneous sample, indicated by the narrow transition. Note that the transition width is less than 1% of the transition temperature. For comparison, we show the transition of an inhomogeneous sample in Fig. 5.1(b). The inhomogeneous sample is also overdoped, with a transition temperature some degrees lower than that of the homogeneous sample. In the following, we first discuss measurements taken on the homogeneous sample, and then compare them to spectroscopic data on the inhomogeneous sample.

Within a couple of days after annealing, the sample is cleaved *in situ* (10^{-9} mbar) at room temperature, directly inserted in the STM head, and cooled down to 4.2 K in pure helium exchange gas. When the time between annealing the sample and cooling it down in the STM is considerably more than a week, we generally find increased inhomogeneity. The tunnelling direction in our experiments is perpendicular to the CuO_2 planes, leading to $\mathrm{d}I/\mathrm{d}V$ spectra which represent the quasiparticle density of states in the plane at an energy eV. The bias voltage V is applied to the sample, such that negative and positive bias correspond to occupied and unoccupied states, respectively. More details about the experimental set-up can be found in chapter 2 and Ref. [18, 19].

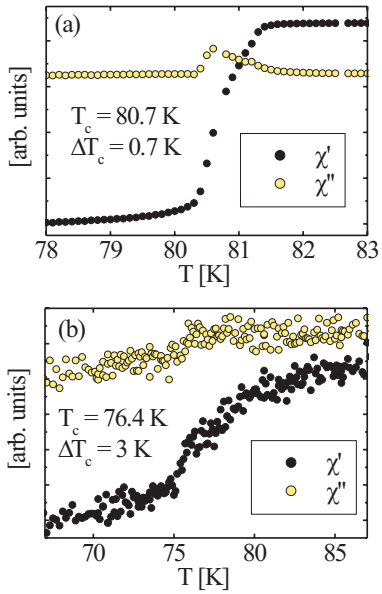

Figure 5.1: AC susceptibility measurements of the superconducting transition, with the real (χ') and the imaginary (χ") parts of the magnetic susceptibility. In (a) the transition of a slightly overdoped sample having undergone the annealing procedure described in the text, the transition width is less than 1% of the transition temperature. In (b) another overdoped sample, but less homogeneous. (Furthermore, a smaller sample size gives rise to a smaller signal to noise ratio.)

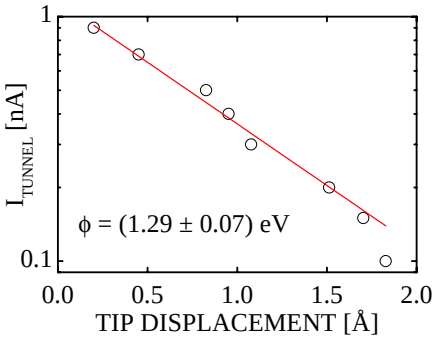

Figure 5.2: Verification of the vacuum tunnelling barrier. The current decays exponentially with the tip-sample distance (tip displacement) as expected.

5.3 Results and discussion

We first check that the tunnelling barrier is actually the vacuum, by establishing the exponential decay of the current with tip-sample distance (Eq. 3.1). The tunnelling current as function of tip displacement is shown in Fig. 5.2. The work function derived from this measurement is $\phi = (1.29 \pm 0.07)$ eV. The general shape of the spectra is independent of the tunnelling resistance within the regime measured during this experiment.

To verify the spatial resolution of the experiment, topographic images are recorded. In

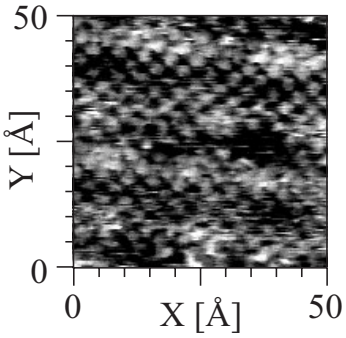

Figure 5.3: 50×50 Å topographic image with atomic resolution. $I_t = 0.2$ nA, $V = 1.0$ V.

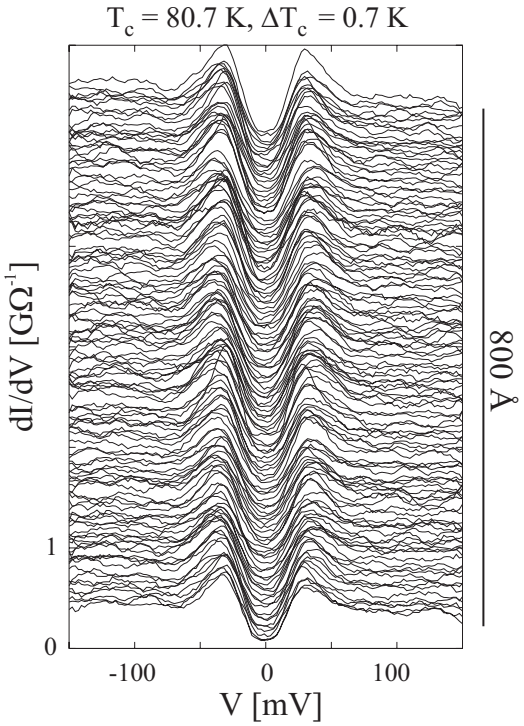

Figure 5.4: Numerical derivatives of $I - V$ spectra taken along a line of 800 Å on the surface of a homogeneous sample at 4.2 K.

Fig. 5.3 atomic resolution is demonstrated. The resolution is thus sufficient to observe any variations in the local density of states at a nanometre scale.

Having established proper tunnelling conditions and atomic resolution, we show tunnelling spectra taken along an 800 Å long trace on the surface. There is no sign of a pseudogap or semiconducting state at the surface. Furthermore, the coherence peaks persist all over the surface, and the gap width variations are $< 20\%$. The average gap (as determined from the energy of the coherence peaks) is $\Delta_p = (36 \pm 2)$ meV.

For comparison, we show a similar trace of spectra on a less homogeneous sample [the transition in Fig. 5.1(b)], in Fig. 5.5. The result of this measurement is completely different. The gap width varies between about 30 and 50 meV, due to a large scatter of the coherence peaks. Furthermore, several spectra have a pseudogap shape, com-

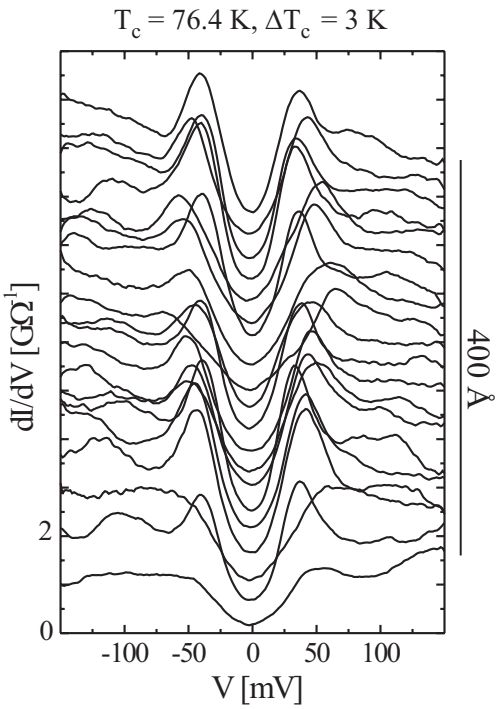

Figure 5.5: Numerical derivatives of $I - V$ spectra taken along a line of 400 Å on the surface of a less homogeneous sample at 4.2 K.

pletely lacking pronounced coherence peaks. Thus, in spite of a rather sharp transition ($\Delta T_c/T_c = 3/76.4 = 4\%$!), there is much more disorder than in the homogeneous sample. This resembles the observations of Refs. [4–8] The disorder may be due to variations of the local doping concentration on distances an order of magnitude shorter than the mean free path [7, 13], or even be the signature of true microscopic phase separation [8].

However, our results on the homogeneous sample indicate that this disorder or inhomogeneity is *not inherent* to high-T_c superconductivity, at least not to overdoped samples. Moreover, the observation of a pseudogap in similarly homogeneous samples [10] is rather difficult to reconcile with scenarios explaining the pseudogap as a combination of superconducting and normal domains [15, 16].

With the presently available experimental data, it is hard to be conclusive about inhomogeneity in underdoped samples. Measuring the broadening of the in-plane Cu-O bond-length distribution, neutron diffraction data on $La_{2-x}Sr_xCuO_4$ suggest that underdoping results in more disorder [20]. The most straightforward explanation follows from considering the doping concentration. For a larger amount of additional oxygen ions, the distances between them will become smaller than the coherence length ξ. Deviations from an ordered distribution will thus have a smaller effect on the homogeneity of the superconducting state for overdoped than for underdoped samples. Nevertheless, it remains to be verified if underdoped samples can be obtained with the same degree of homogeneity as in the overdoped sample presented here, or not.

5.4 Conclusion

In summary, it has been demonstrated that long-range homogeneity can be obtained in HTSs, in particular in overdoped BSCCO samples. It has also been found that large disorder at a nanometre scale leads to only a small variation in the macroscopic transition width. In other words: macroscopic superconductivity is rather insensitive to local inhomogeneity.

The large differences on a local scale resulting from minor changes in macroscopic properties can explain why different groups find different degrees of inhomogeneity on apparently very similar samples. This conclusion calls for extreme care with sample preparation.

Our results, in combination with previous results of Renner *et al.* [10], are in apparent disagreement with an explanation of the pseudogap invoking inhomogeneity as the driving factor. Since the STM has a relatively low time resolution, a dynamic manifestation of phase separation cannot be excluded. However, from this work it becomes clear that any static phase separation, *if inherent* to high-T_c superconductivity, has only minor effects on the local electronic properties of HTSs.

References

[1] J.-X. Liu, J.-C. Wan, A.-M. Goldman, Y. C. Chang, and P. Z. Jiang, Phys. Rev. Lett. **67**, 2195 (1991).

[2] A. Chang, Z. Y. Rong, Y. M. Ivanchenko, F. Lu, and E. L. Wolf, Phys. Rev. B **46**, 5692 (1992).

[3] Ch. Renner and Ø. Fischer, Phys. Rev. B **51**, 9208 (1995).

[4] T. Cren, D. Roditchev, W. Sacks, J. Klein, J.-B. Moussy, C. Deville-Cavellin, and M. Laguës, Phys. Rev. Lett. **84**, 147 (2000).

[5] T. Cren, D. Roditchev, W. Sacks, and J. Klein, Europhys. Lett. **54**, 84 (2001).

[6] C. Howald, P. Fournier, and A. Kapitulnik, Phys. Rev. B **64**, 100504 (2001).

[7] S. H. Pan, J. P. O'Neal, R. L. Badzey, C. Chamon, H. Ding, J. R. Engelbrecht, Z. Wang, H. Eisaki, S. Uchida, A. K. Gupta, K.-W. Ng, E. W. Hudson, K. M. Lang, and J. C. Davis, Nature **413**, 282 (2001).

[8] K. M. Lang, V. Madhavan, J. E. Hoffman, E. W. Hudson, H. Eisaki, and S. Uchida J. C. Davis, Nature **415**, 412 (2002).

[9] H. Ding, J. R. Engelbrecht, Z. Wang, J. C. Campuzano, S.-C. Wang, H.-B. Yang, R. Rogan, T. Takahashi, K. Kadowaki, and D. G. Hinks, Phys. Rev. Lett. **87**, 227001 (2001).

[10] Ch. Renner, B. Revaz, J.-Y. Genoud, K. Kadowaki, and Ø. Fischer, Phys. Rev. Lett. **80**, 149 (1998).

[11] B. W. Hoogenboom, K. Kadowaki, B. Revaz, M. Li, Ch. Renner, and Ø. Fischer, Phys. Rev. Lett. **87**, 267001 (2001).

[12] I. Martin and A. V. Balatsky, Physica C **357-360**, 46 (2001).

[13] Z. Wang, J. R. Engelbrecht, S. Wang, H. Ding, and S. H. Pan, Phys. Rev. B **65**, 64509 (2002).

[14] V. J. Emery, S. A. Kivelson, and H. Q. Lin, Phys. Rev. Lett. **64**, 475 (1990).

[15] Y. N. Ovchinnikov, S. A. Wolf, and V. Z. Kresin, Phys. Rev. B **63**, 64524 (2001).

[16] S. Chakravarty, R. B. Laughlin, D. K. Morr, and C. Nayak, Phys. Rev. B **63**, 94503 (2001).

[17] J.-Y. Genoud, Ph.D. thesis, University of Geneva, 1996, no 2826.

[18] Ch. Renner, Ph. Niedermann, A. D. Kent, and Ø. Fischer, J. Vac. Sci. Technol. A **8**, 330 (1990).

[19] A. D. Kent, Ch. Renner, Ph. Niedermann, J.-G. Bosch, and Ø. Fischer, Ultramicroscopy **42-44**, 1632 (1992).

[20] E. S. Božin, G. H Kwei, H. Takagi, and S. J. L. Billinge, Phys. Rev. Lett. **84**, 5856 (2000).

Chapter 6

Shape and Motion of Vortex Cores

6.1 Introduction

The study of the vortex phases in high temperature superconductors (HTSs) has lead to both theoretical predictions of several novel effects and experiments accompanied by challenging interpretations. The reasons are multiple. First, the unconventional symmetry of the order parameter – most likely $d_{x^2-y^2}$ – leads to the presence of low-lying quasiparticle excitations near the gap nodes, which in turn has inspired the predictions of a non-linear Meissner effect [1], of a $\sqrt{H}$ dependence of the density of states at the Fermi level near the vortex cores [$N(0,\mathbf{r})$] [2], and of a four-fold symmetry of the vortices [3–5]. However, the experimental evidence for the first two effects is still controversial [6–9], and scanning tunnelling spectroscopy (STS) measurements on vortex cores have not shown any clear signature of a $\sqrt{H}$ dependence of $N(0,\mathbf{r})$ [10, 11]. Concerning the four-fold symmetry, a tendency of square vortices was found in previous measurements [11], but inhomogeneities make it difficult to be decisive about it. Interestingly, a four-fold symmetry has been observed around single atom zinc impurities in $Bi_2Sr_2CaCu_2O_{8+\delta}$ (BSCCO), which are of a smaller size than the vortex cores [12].

A second reason is related to the interaction of vortices with pinning centres, responsible for the rich vortex phase diagram of the HTSs [13]. The pinning of vortices is mainly due to local fluctuations of the oxygen concentration [14–17], and facilitated by their highly 2D "pancake" character. In BSCCO the areal density of oxygen vacancies per CuO_2 double layer is in fact surprisingly large: 10^{17} m^{-2} [16], corresponding to an average distance between the oxygen vacancies of the order of 10 Å. This vortex pinning results for BSCCO in the absence of any regular flux line lattice at high fields, as demonstrated by both neutron diffraction [18] and STS [11] experiments. Moreover, since the distance between the oxygen vacancies is of the order of the vortex core size, one may expect that not only the vortex distribution, but also the vortex core shape will be dominated by pinning effects, and *not* by intrinsic symmetries like that of the order parameter. A detailed understanding of the interaction of vortices with pinning centres will thus be of importance to explain the lack of correspondence between theoretical predictions about the vortex shape and STS measurements.

Third, and again as a consequence of the anisotropy of the order parameter, low-energy

quasiparticles are not truly localised in the vortex core (in contrast to the situation in s-wave superconductors [19–21]). For pure d-wave superconductors these quasiparticles should be able to escape along the nodes of the superconducting gap. Thus in the vortex core spectra one expects a broad zero-bias peak of spatially extended quasiparticle states [5]. However, tunnelling spectra of the vortex cores in $YBa_2Cu_3O_{7-\delta}$ (YBCO) showed two clearly separated quasiparticle energy levels, which were interpreted as a signature of localised states [10]. In BSCCO two weak peaks have been observed in vortex core spectra [22–24], suggesting a certain similarity to the behaviour in YBCO. These features are subject of chapter 7 and 8. Another important characteristic of HTSs that follows from the STS studies mentioned above, is the extremely small size of the vortex cores in these materials. The large energy separation between the localised quasiparticle states indicates that the vortex cores in YBCO are of such a size that quantum effects dominate. This is even more true in BSCCO: not only the in-plane dimensions of the vortex cores are smaller than in YBCO and become of the order of the interatomic distances [11], but due to the extreme anisotropy of the material also their out-of-plane size is strongly reduced. This highly quantised character of vortices in HTSs is equally demonstrated by the non-vanishing magnetic relaxation rate in the limit of zero temperature, attributed to quantum tunnelling of vortices through the energy barriers between subsequent pinning centres [13].

In this chapter we present a detailed STS study of the shape of the vortices in BSCCO. We will show that this shape is influenced by inhomogeneities. The samples presented here, which we characterise as moderately homogeneous, are used to study the behaviour of vortex cores under these conditions. Apart from the vortex core shape, this also includes the evolution in time of the vortex distribution. We will show that both effects can be related to tunnelling of vortices between different pinning centres. This is another indication of the possible extreme quantum behaviour of vortex cores in HTSs. A corollary of this paper is that only extremely homogeneous samples will show intrinsic shapes of vortex cores.

6.2 Experimental details

The tunnelling spectroscopy was carried out using a scanning tunnelling microscope (STM) with an Ir tip mounted perpendicularly to the (001) surface of a BSCCO single crystal, grown by the floating zone method. The crystal was oxygen overdoped, with $T_c = 77$ K, and had a superconducting transition width of 1 K (determined by an AC susceptibility measurement). We cleaved *in situ*, at a pressure $< 10^{-8}$ mbar, at room temperature, just before cooling down the STM with the sample. The sharpness of the STM tip was verified by making topographic images with atomic resolution. Tunnelling current and sample bias voltage were typically 0.5 nA and 0.5 V, respectively. We performed the measurements at 4.2 K with a low temperature STM described in chapter 2 and Ref. [25, 26], and those at 2.5 K with a recently constructed ^{3}He STM [27, 28].* A magnetic field of 6 T parallel to the c-axis of the crystal was applied after having cooled down the sample. The measurements presented here were initiated 3 days after having switched on the field.

*The measurements at 2.5 K were performed by M. Kugler

The dI/dV spectra measured with the STM correspond to the quasiparticle local density of states (LDOS). In the superconducting state one observes two pronounced coherence peaks, centred around the Fermi level, at energies $\pm\Delta_p$. The gap size Δ_p varied from 30-50 meV. In the vortex cores the spectra are remarkably similar to those of the pseudogap in BSCCO measured above T_c [11], with a total disappearance of the coherence peak at negative bias, a slight increase of the zero bias conductivity, and a decrease and shift to higher energy of the coherence peak at positive bias. To map the vortex cores we define a grey scale using the ratio $\sigma(V_p)/\sigma(0)$, of the conductivity $\sigma(V_p) = \mathrm{d}I/\mathrm{d}V(V_p)$ at a negative sample voltage $V_p = -\Delta_p/e$ and the zero bias conductivity $\sigma(0) = \mathrm{d}I/\mathrm{d}V(0)$. Thus we obtain spectroscopic images, where vortex cores appear as dark spots. Since we measure variations of the LDOS, which occur at a much smaller scale (ξ) than the penetration depth λ, we can get vortex images at high fields. A tunnelling spectrum is taken on the time scale of seconds, spectroscopic images typically take several hours (about 12 hours for the images of 100x100 nm^2 presented below). The images therefore necessarily reflect a time-averaged vortex density.

In all large-scale images we have suppressed short length-scale noise by averaging each point over a disk of radius $\sim$ 20 Å. When zooming in to study the shape of individual vortices, we strictly used raw data. Further experimental details can be found in chapter 2 and previous publications [11, 29, 30].

6.3 Results

6.3.1 Vortex distribution

In Fig. 6.1 we show spectroscopic images of the surface of a BSCCO crystal, at different magnetic field strengths. The large dark structure, clearly visible at the right of Figs. 6.1(a) and (b), corresponds to a degraded region resulting from a large topographic structure. The presence of this structure allows an exact position determination throughout the whole experimental run. As can be seen in Fig. 6.1 in exactly the same region, the number of vortices at 6 and at 2 T scales very well with the expected number of flux quanta (Φ_0) at these field strengths. This clearly proves that the observed dark spots are directly related to vortex cores, and not to inhomogeneities, defects or any form of surface degradation. The large spot in the upper left corner of Fig. 6.1(c) forms an exception: it appeared after a sudden noise on the tunnel current while we were scanning on that position, showed semiconducting spectra (typical for degraded tunnelling conditions) afterwards, and remained even after having set the external field to 0 T. One should however not exclude that a vortex is pinned in this degraded zone. Finally, the size and density of the vortices are fully consistent with previous measurements [11, 23].

Instead of a well ordered vortex lattice, one observes patches of various sizes and shapes scattered over the surface. This clearly indicates the disordered nature of the vortex phase in BSCCO at high fields, again in consistency with previous STM studies [11, 23] and neutron scattering data [18], and stressing the importance of pinning for the vortex distribution.

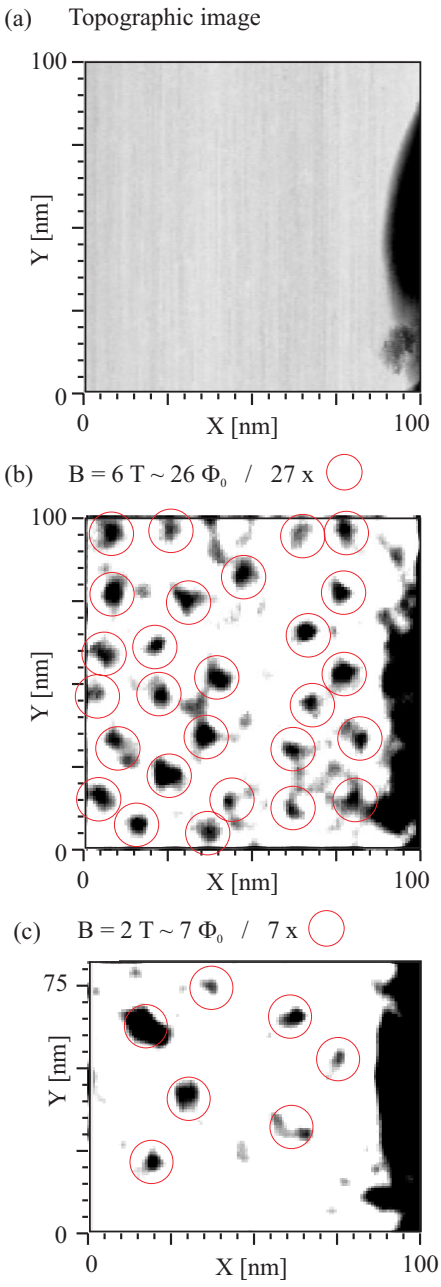

Figure 6.1: (a) Topography of a 100x100 nm^2 region of the BSCCO surface at 4.2 K and 6 T, with a large defect at the right. (b) Spectroscopic image of the region in (a), again at 4.2 K and 6 T. Dark spots correspond to vortex cores, the dark region at the right corresponds to the topographic defect in (a). For the surface excluding the defect one should expect 26 vortices, the image contains 27 (the circles around the vortex cores serve as a guide to the eye). (c) Part of the same region, at 2 T. The number of vortices in the image again perfectly corresponds to what one should expect for the given surface.

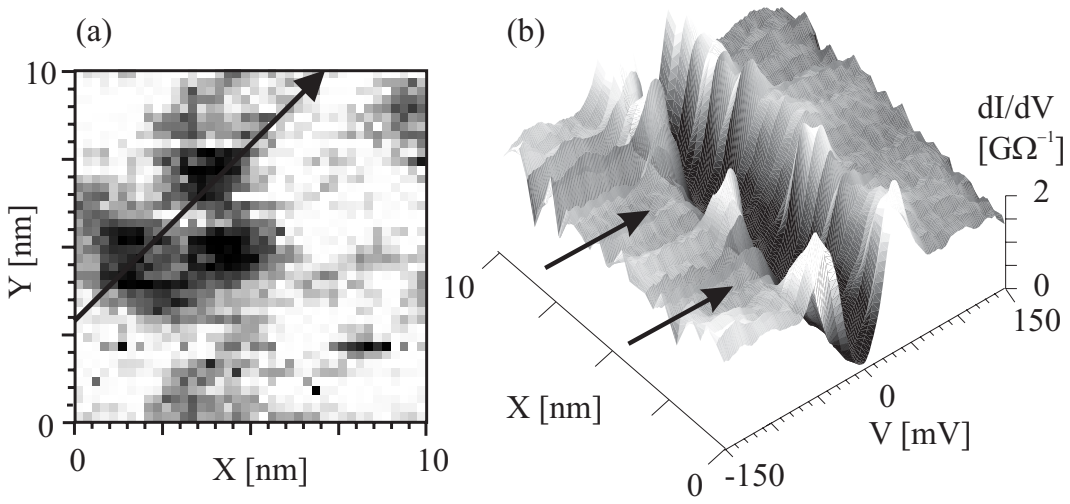

Figure 6.2: (a) Image of a vortex core consisting of several separate elements. ($B = 6$ T, $T = 4.2$ K.) (b) Spectra along a trace [the arrow in (a)] through the vortex core reveal that between regions with vortex core-like spectra (indicated by the two arrows) the superconducting coherence peaks come up again.

6.3.2 Vortex shape

As a next step we increase the spatial resolution to investigate individual vortex cores. Some vortices appear with square shapes, but most vortices in this study have irregular shapes. Closer inspection of the tunnelling spectra reveals small zones inside the vortex core that show superconducting behaviour. That is, when scanning through a vortex core one often observes (slightly suppressed) coherence peaks (Fig. 6.2), typical for the superconducting state, at some spots *inside* the vortex core. The latter is generally characterised by the *absence* of these peaks. In some cases, the vortex cores are even truly split into several smaller elements [Fig. 6.2(a)], totally separated by small zones showing the rise of coherence peaks. This has been verified by measuring the full spectra along lines through the vortex core, as in Fig. 6.2(b).

The smaller elements of a split vortex core cannot be related to separate vortices: first, the vortex-vortex repulsion makes it highly improbable that several vortex cores are so close to each other; second, counting all these elements as a flux quantum in Fig. 6.1(b), one finds a total flux through the surface that is far too large compared to the applied field. One should note here that the magnetic size of a flux line is of the order of the penetration depth $\lambda \sim 2500$ Å, much larger than the vortex *core* splitting observed here.

6.3.3 Vortex motion

With subsequent spectroscopic images like Fig. 6.1(b), one can also study the vortex distribution as a function of time. We expect the vortex motion to be negligible, since

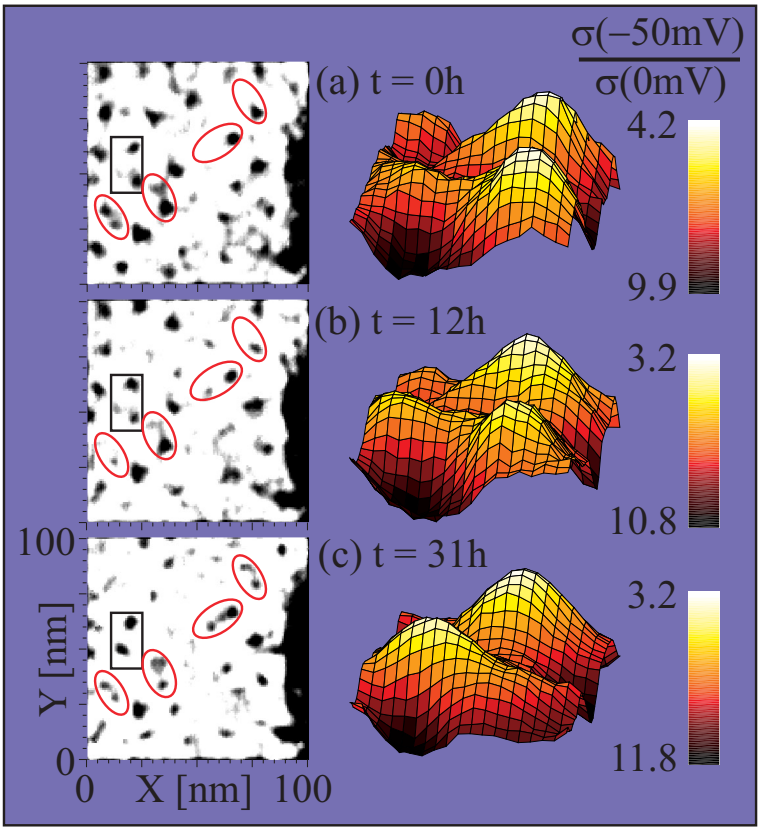

Figure 6.3: Sequence of images to study the behaviour of the vortex cores in time, $B = 6$ T, $T = 4.2$ K. (a) t = 0; (b) t = 12h; (c) t = 31h. Left: 2D representation, with the same grey scale. Right: 3D images of the zone marked by the rectangles in the 2D images. The vortex core seems to be split in (b), before it totally moves from one position in (a) to the other in (c).

we allowed the vortices to stabilise for more than 3 days [31]. However, in Fig. 6.3 one can see that many vortices still have not reached totally stable positions. Many of them roughly stay on the same positions over the time span of our measurement, but others move to neighbouring positions. Five different cases of moving vortices are indicated by the ellipses and the rectangle in Fig. 6.3.

In the panels on the left side the precise intensity of each point is difficult to read out directly. To investigate more quantitatively the time evolution of the vortex distribution, from one frame to the next, we show in the right part of Fig. 6.3 3D representations of the area marked by the rectangle in the 2D spectroscopic images. They give an idea of the grey scale used in the 2D images, and provide a detailed picture of the movement of the vortex core in front: from the right in Fig. 6.3(a) to the left in Fig. 6.3(c). The vortex core at the back does not move, and serves as a reference for the intensity. We remind that the intensity, or height in the 3D images, is a measure of the LDOS, which in a vortex core is different from the superconducting DOS. It is most interesting to see what happens in Fig. 6.3(b): the (moving) vortex core is *divided* between two positions. Thus, the vortex core moves from one position to the other, passing through an intermediate state where the vortex splits between the two positions. Note that these two positions do not correspond to two vortices. In fact, the split vortex is characterised by the lower intensity compared to the nearby (reference) vortex. This means that the coherence peak

at negative voltage does not completely disappear, as it should if we had a complete and stable vortex at each of these positions. Note also that the density of vortices around the rectangular area on the left side in Fig. 6.3 would clearly be too high if we counted the mentioned positions and all positions in the ellipses as individual flux quanta. The split vortex discussed here is not a unique example. Similar behaviour can be found for several other vortex cores, as indicated by the ellipses in Fig. 6.3. This gradual change of position is in striking contrast to the STS observations of moving vortices in $NbSe_2$ [32, 33]. In $NbSe_2$ the round vortices appear as ellipses when they slowly move.

6.3.4 Temperature dependence

We performed measurements both at 4.2 and at 2.5 K, on samples cut from the same batch of crystals. The data taken at 2.5 K [28] are fully consistent with the presented work at 4.2 K. In Fig. 6.4 we provide imags of the vortex cores at 2.5 T, including an analogue of the moving vortex core of Fig. 6.3. Though it is hard to obtain any quantitative data, one can conclude that the vortex cores roughly have the same size, similar irregular shapes, and examples of split vortex cores are easily found.

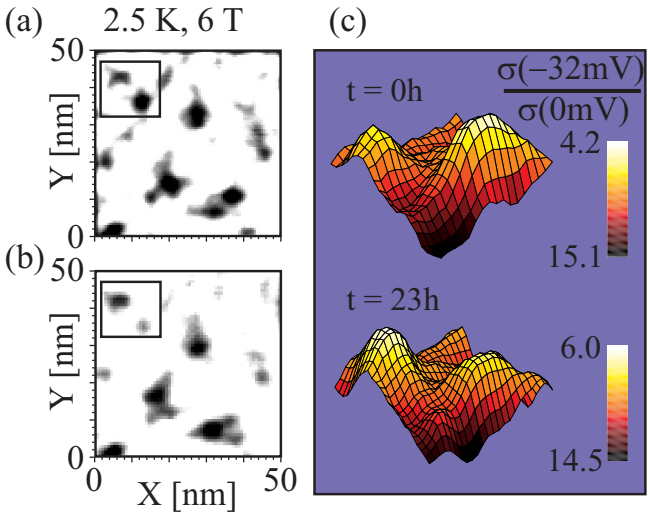

Figure 6.4: Subsequent images ((a) and (b)) at $B = 6$ T, $T = 2.5$ K. In (c) a 3D representation of the square marked in (a) and (b). At 2.5 K one observes the same phenomena as at 4.2 K in Fig. 6.2 and Fig. 6.3.

6.4 Discussion

6.4.1 Experimental considerations

The observation of such a highly irregular pattern of vortex cores, as presented above, requires a careful analysis of the experimental set-up. However, the fact that keeping exactly the same experimental conditions the number of vortex cores scales with the magnetic field, is a direct proof of the absence of artificial or noise-related structures in

the spectroscopic images. Furthermore, since topographic images showed atomic resolution, there is no doubt that the spatial resolution of the STM is sufficient for the analysis of vortex core shapes.

The stability of the magnetic field can be verified by counting the number of vortices in the subsequent images at 6 T (Fig. 6.3). Since, without double-counting the split vortices marked by the ellipses, this number is constant (26 ± 3), we can exclude any substantial long time-scale variation of the magnetic field. Some variation in the total black area from one image to the other can be related to the tunnelling conditions: a little more noise on the tunnel current will give a relatively large increase of the small zero-bias conductance. Since we divide by the zero-bias conductance to obtain the spectroscopic images, this may lead to some small variations in the integrated black area of the images.

6.4.2 Delocalisation

Keeping in mind the randomness of the vortex distribution at 6 T due to pinning of vortices, we now relate both the split vortex cores (Fig. 6.2) and the intermediate state between two positions (Figs. 6.3 and 6.4) to the same phenomenon: the vortex cores appear to be delocalised between different positions which correspond to pinning potential wells, and during the measurement hop back and forth with a frequency that is too high to be resolved in this experiment. According to this analysis not only the distribution, but also the observed shape of the vortex cores is strongly influenced by pinning.

The pinning sites most probably result from inhomogeneities in the oxygen doping, which are thought to be responsible for the variations of the gap size (see experimental details). The distance over which the vortices are split corresponds to the average spacing between oxygen vacancies ($10 - 100$ Å [16]). We did not observe any sign of resonant states related to impurities, as in recent STM experiments on BSCCO [34, 35]. The driving forces causing vortex movements in Figs. 6.3 and 6.4 are most probably due to a slow variation of the pinning potential, resulting from the overall rearrangement of vortices.

The vortex delocalisation and movement presented here can directly be connected to the vortex creep as measured in macroscopic experiments, like magnetic relaxation [13]. The main difference, of course, is that we do not observe whole bundles of vortices moving over relatively large distances, but only *single* vortex cores that are displaced over distances much smaller than the penetration depth λ. That is, it will not be necessary to displace whole groups of vortices, many of which might be pinned much stronger than the delocalised vortices we observe. A second difference is the absence of a uniform direction of the movements in the STM images, most probably because the Lorentz driving forces have been reduced to an extremely small value (which also follows from the very gradual changes in Figs. 6.3 and 6.4).

6.4.3 Thermal fluctuations versus quantum tunnelling

Regarding now the mechanism responsible for the vortex delocalisation, the main question is whether we are dealing with thermal fluctuations, or quantum tunnelling between pinning potential wells. Magnetic relaxation measurements on BSCCO show a crossover

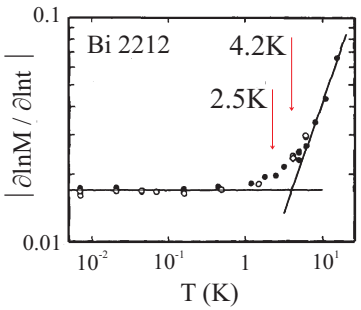

Figure 6.5: Normalised decay rates of the magnetisation, as a function of temperature in a double logarithmic scale. The transition between thermal creep and (temperature-independent) quantum creep occurs between 10 and 1 K. (Fig. from Aupke *et al.* [37].)

temperature from thermal to quantum creep of $2-5$ K [31, 36–38], which means that with STM measurements at 4.2 and 2.5 K we are on the limit between the two.

In the case of thermally induced motion, there is a finite probability for the vortex to jump *over* the energy barrier between the two potential wells. The vortex is continuously moving from one site to the other, with a frequency that is too high to be resolved by our measurements. In the case of quantum tunnelling, the vortex is truly delocalised. That is, the vortex can tunnel *through* the barrier, and there is a combination of two base states (i.e. positions), like in the quantum text book example of the ammonia molecule [39]. Thermal fluctuations will lead to a continuous dissipative motion [13, 40] between the two sites; quantum tunnelling gives a dissipationless state in which the vortex is *divided* between two positions.

An instantaneous observation of several base states of a quantum object would be impossible, since each measurement implies a collapse of the quantum wave function into one state. However, the STM gives only time averaged images, and with the tunnelling current in this experiment we typically detect one electron per nanosecond. If the vortex core relaxes back to its delocalised state on a time scale smaller than nanoseconds, the vortex can appear delocalised in the STM images. Moreover, it should be clear that the long time (12 hours) between the subsequent images in Figs. 6.3 and 6.4 has nothing to do with the vortex tunnelling time; it is tunnelling of the vortex that allows the intermediate state. The vortex core is in a superposition of states (positions), which results from the possibility of quantum tunnelling between these states. In this superposition of states the vortex core has a certain probability to be at one position, and a probability to be at the other. At each measurement (electron passing the tunnelling barrier) the vortex core is either at one position or at the other, relaxing back to the split state in between the measurements.

Thermally induced hopping between different pinning sites should be proportional to $\exp(-U/k_BT)$, where U is the effective pinning energy [13]. From magnetic relaxation measurements on BSCCO one can derive a value of about $10-10^3$ K for this quantity [16, 31, 36–38]. Assuming for the moment that this U determines the hopping of individual vortices, it should then be compared to the Euclidian action for quantum tunnelling, which from magnetic relaxation measurements is estimated to be $S_E/\hbar \sim 10^2$ [13]. The latter parameter plays a role like U/k_BT in the Boltzman distribution. For measurements presented here, it is important to note again that they were taken more

than 3 days after having increased the field from 0 to 6 T. Since for $B = 6$ T the induced current density j relaxes back to less than 0.01 of its initial value in about 10 seconds [31], we are clearly in the limit where j and thus the Lorentz driving forces (which reduce the energy barrier for vortex creep) approach zero. This means that the effective pinning potential U rises, if not to infinity like in isotropic materials, to a value which in principle is much higher than the one which determines vortex creep in magnetic relaxation measurements at comparable field strengths. Since quantum creep in the limit of vanishing dissipation is independent of this collective aspect of U, while the probability for thermal creep decreases as $\exp(-U/k_BT)$ [13], one can expect quantum creep to become more important than thermal creep when more time has passed after having changed the field.

However, the collective U may be higher than the pinning barriers for the individual vortex movements observed in our experiments. To find a lower bound for the latter, we estimate U for the moving vortices from our microscopic measurement. First we calculate the magnetic energy of a vortex due to the interaction with its nearest neighbours, using

$$E_{int} = d\frac{\Phi_0^2}{8\pi^2\lambda^2}\sum_i\{\ln[\frac{\lambda}{r_i}] + 0.12\}, \tag{6.1}$$

where d is the length of the vortex segment (here we assume pancake vortices and take $d = 15$ Å $\sim$ size of one double Cu-O layer), Φ_0 is the flux quantum, λ the in-plane penetration depth (~ 2500 Å) and r_i the distance to its ith neighbour [15]. Taking the vortex in Fig. 6.3(b), and determining the positions between which it is divided as well as the positions of the neighbouring vortices, one can find the difference between the magnetic interaction energies of the delocalised vortex at its two positions. We obtain $E_{int} \sim 120$ K. The absence of any vortex lattice indicates that the pinning potential wells are generally larger than the magnetic energy difference between the subsequent vortex positions, and Fig. 6.3(b) reflects a vortex state that is quite common in our measurements (Fig. 6.1). Following these arguments one can safely assume that the effective potential well pinning the vortex in Fig. 6.3 is larger than this difference: $U > E_{int} = 120$ K, in agreement with the estimates given above. So we obtain $U/k_BT > 10 - 10^2$ for temperatures around 4 K. In the limit of zero dissipation $S_E/\hbar \sim (k_F\xi)^2$. On the basis of STS experiments [10, 11] this can be estimated to be ≤ 10. Thus $S_E/\hbar$ is smaller than U/k_BT, and suggests that quantum tunnelling is dominant in our measurements [13].

The most direct evidence for quantum creep can be obtained from measurements at different temperatures. The hopping rate for thermally induced movements is given by $\omega_0 \exp(-U/k_BT)$, where U is the pinning potential, and ω_0 the characteristic frequency of thermal vortex vibration [15]. Assuming $U = 100$ K, and a conservatively large estimate of $\omega_0 \sim 10^{11}$ s^{-1}, the hopping rate should drop from 1 s^{-1} to 10^{-7} s^{-1} on cooling from 4.2 to 2.5 K. This gives a huge difference between the respective measurements at these temperatures. However, spectroscopic images at 4.2 and 2.5 K show the same pattern of moving and delocalised vortices. Following the same kind of estimations as above, the delocalised vortex at 2.5 K (Fig. 6.4) gave $U > 210$ K, which makes thermal creep even more unlikely here. Even if the frequency of the individual thermal vortex movements were too high to be resolved by our measurements *both* at 4.2 and at 2.5 K (this would mean a rather unrealistic characteristic frequency $\omega_0 > 10^{15}$), one would still expect to

see a difference. As a matter of fact, the driving force for the vortex movements results from an overall rearrangement of vortices. This means that the displacements of vortices will always depend on the hopping frequency. Thus when the hopping rate is reduced by a factor 10^7 (between 4.2 and 2.5 K), one should observe a reduction of the number of split or irregularly shaped vortices, even for very high characteristic frequencies.

6.5 Conclusion

We observed vortex cores delocalised over several pinning potential wells. Regardless of the exact mechanism (thermal hopping or quantum tunnelling) responsible for this delocalisation, our measurements point out that pinning effects not only dominate the distribution of the vortex cores, but also their shape. As a consequence intrinsic (possibly four-fold) symmetries of the vortex cores will be obscured in microscopic measurements. The delocalisation of the vortex cores implies that the vortex cores in this study appear larger than their actual – unperturbed – size, indicating a coherence length that is even smaller than was expected on the base of previous studies [11].

The analysis given above strongly favours an interpretation in terms of quantum tunnelling of vortex cores. This would not only mean the first microscopic signature of the vortex quantum tunnelling as derived from magnetic relaxation measurements, it is also a further indication [41] that objects of larger size and complexity than one or several atoms can appear as a superposition of different quantum states.

References

[1] S. K. Yip and J. A. Sauls, Phys. Rev. Lett. **69**, 2264 (1992).

[2] G. E. Volovik, Pis'ma Zh. Éksp. Teor. Fiz. **58**, 457 (1993), [JETP Lett. **58**, 1174 (1993)].

[3] A. J. Berlinsky, A. L. Fletter, M. Franz, C. Kallin, and P. I. Soininen, Phys. Rev. Lett. **75**, 2200 (1995).

[4] M. I. Salkola, A. V. Balatsky, and D. J. Scalapino, Phys. Rev. Lett. **77**, 1841 (1996).

[5] M. Franz and Z. Tešanović, Phys. Rev. Lett. **80**, 4763 (1998).

[6] K. A. Moler, D. J. Baar, J. S. Urbach, R. Liang, W. N. Hardy, and A. Kapitulnik, Phys. Rev. Lett. **73**, 2744 (1994).

[7] A. Maeda, Y. Lino, T. Hanaguri, N. Motohira, K. Kishio, and T. Fukase, Phys. Rev. Lett. **74**, 1202 (1995).

[8] B. Revaz, J.-Y. Jenoud, A. Junod, K. Neumaier, A. Erb, and E. Walker, Phys. Rev. Lett. **80**, 3364 (1998).

[9] M. H. S. Amin, I. Affleck, and M. Franz, Phys. Rev. B **58**, 5848 (1998).

[10] I. Maggio-Aprile, Ch. Renner, A. Erb, E. Walker, and Ø. Fischer, Phys. Rev. Lett. **75**, 2754 (1995).

[11] Ch. Renner, B. Revaz, K. Kadowaki, I. Maggio-Aprile, and Ø. Fischer, Phys. Rev. Lett. **80**, 3606 (1998).

[12] S. H. Pan, E. W. Hudson, K. M. Lang, H. Eisaki, S. Uchida, and J. C. Davis, Nature **403**, 746 (2000).

[13] G. Blatter, M. V. Feigel'man, V. B. Geschkenbein, A. I. Larkin, and V. M. Vinokur, Rev. Mod. Phys. **66**, 1125 (1994), and references therein.

[14] M. Tinkham, Helv. Phys. Acta **61**, 443 (1988).

[15] M. Tinkham, *Introduction to Superconductivity*, 2nd. ed. (McGraw-Hill, New York, 1996).

[16] T. W. Li, A. A. Menovsky, J. J. M. Franse, and P. H. Kes, Physica C **257**, 179 (1996).

[17] A. Erb, A. A. Manuel, M. Dhalle, F. Marti, J.-Y. Genoud, B. Revaz, A. Junod, D. Vasumathi, S. Ishibashi, A. Shukla, E. Walker, Ø. Fischer, R. Flükiger, R. Pozzi, M. Mali, and D. Brinkmann, Solid State Comm. **112**, 245 (1999).

[18] R. Cubitt, E. M. Morgan, G. Yang, S. L. Lee, D. Mck. Paul, H. A. Mook, M. Yethiraj, P. H. Kes, T. W. Li, A. A. Menovsky, Z. Tarnawski, and K. Mortensen, Nature **365**, 407 (1993).

[19] C. Caroli, P. G. de Gennes, and J. Matricon, Phys. Lett. **9**, 307 (1964).

[20] H. F. Hess, R. B. Robinson, R. C. Dynes, J. M. Valles, and J. V. Waszczak, Phys. Rev. Lett. **62**, 214 (1989).

[21] Ch. Renner, A. D. Kent, Ph. Niedermann, Ø. Fischer, and F. Lévy, Phys. Rev. Lett. **67**, 1650 (1991).

[22] B. W. Hoogenboom, Ch. Renner, B. Revaz, I. Maggio-Aprile, and Ø. Fischer, Physica C **332**, 440 (2000).

[23] S. H. Pan, E. W. Hudson, A. K. Gupta, K.-W. Ng, H. Eisaki, S. Uchida, and J. C. Davis, Phys. Rev. Lett. **85**, 1536 (2000).

[24] B. W. Hoogenboom, K. Kadowaki, B. Revaz, M. Li, Ch. Renner, and Ø. Fischer, Phys. Rev. Lett. **87**, 267001 (2001).

[25] Ch. Renner, Ph. Niedermann, A. D. Kent, and Ø. Fischer, J. Vac. Sci. Technol. A **8**, 330 (1990).

[26] A. D. Kent, Ch. Renner, Ph. Niedermann, J.-G. Bosch, and Ø. Fischer, Ultramicroscopy **42-44**, 1632 (1992).

[27] M. Kugler, Ch. Renner, V. Mikheev, G. Batey, and Ø. Fischer, Rev. Sci. Instrum. **71**, 1475 (2000).

[28] M. Kugler, Ph.D. thesis, University of Geneva, n° 3158 (2000).

[29] Ch. Renner, B. Revaz, J.-Y. Genoud, K. Kadowaki, and Ø. Fischer, Phys. Rev. Lett. **80**, 149 (1998).

[30] Ch. Renner and Ø. Fischer, Phys. Rev. B **51**, 9208 (1995).

[31] A. J. J. van Dalen, R. Griessen, and M. R. Koblischka, Physica C **257**, 271 (1996).

[32] Ch. Renner, Ph.D. thesis, University of Geneva, 1993, n° 2620.

[33] A. M. Troyanovski, J. Aarts, and P. H. Kes, Nature **399**, 665 (1999).

[34] A. Yazdani, C. M. Howald, C. P. Lutz, A. Kapitulnik, and D. M. Eigler, Phys. Rev. Lett. **83**, 176 (1999).

[35] E. W. Hudson, S. H. Pan, A. K. Gupta, K.-W. Ng., and J. C. Davis, Science **285**, 88 (1999).

[36] D. Prost, L. Fruchter, and I. A. Campbell, Phys. Rev. B **47**, 3457 (1993).

[37] K. Aupke, T. Teruzzi, P. Visani, A. Amann, A. C. Mota, and V. N. Zavaritsky, Physica C **209**, 255 (1993).

[38] D. Monier and L. Fruchter, Phys. Rev. B **58**, 8917 (1998).

[39] R. P. Feynman, R. B. Leighton, and M. Sands, *Lectures on Physics* (Addison-Wesley, Reading, Massachusetts, 1965), Vol. III.

[40] J. Bardeen and M. J. Stephen, Phys. Rev. **140**, A1197 (1965).

[41] M. Arndt, O. Nairz, J. Vos-Andreae, C. Keller, G. van der Zouw, and A. Zeilinger, Nature **401**, 680 (1999).

Chapter 7

Low-Energy Quasiparticle States in Vortex Cores

7.1 Introduction

Much interest of scanning tunnelling spectroscopy (STS) studies on high-temperature superconnductors (HTSs) follows from its ability to probe the electronic structure of the vortices. In particular, one can concentrate on quasiparticle vortex core states, which are of importance for the understanding of various static and dynamic properties of the mixed state. In conventional s-wave superconductors the vortex cores contain discrete quasiparticle excitations [1], which – because of their small energy spacing – show up as a broad continuum zero-bias conductance peak in the vortex cores in $NbSe_2$ [2, 3]. In HTSs the nature of the quasiparticle core states is not as easily understood, because of the anisotropy of the order parameter – most likely $d_{x^2-y^2}$ symmetry. Applying conventional BCS ideas to a d-wave superconductor, one would expect the quasiparticle core states to extend in the directions of the nodes of the gap function. This excludes the existence of truly localised states in the vortex core, and experimentally one would observe a broad structure at the Fermi level in the core. This picture was confirmed by numerical calculations [4].

However, in $YBa_2Cu_3O_{7-\delta}$ (YBCO) the vortex core spectra show two pronounced peaks, at ± 5.5 meV, which may correspond to only one localised state [5]. This not only disagrees with d-wave BCS predictions, it also shows that the vortex cores in YBCO are in the extreme quantum limit. Experiments on $Bi_2Sr_2CaCu_2O_{8+\delta}$ (BSCCO) gave an even more surprising result: the spectra in the vortex cores do not show any strong features expected for d- or s-wave BCS superconductors. Instead, they correspond to the pseudogap measured on the same crystals above T_c [6], strongly suggesting that the electronic excitations in the vortex core at low temperature are the same as in the pseudogap state above T_c. Furthermore, vortex cores in BSCCO are even smaller than those in YBCO, of a size approaching the interatomic distances.

The question of possible weak features at energies below the gap in the BSCCO vortex cores was left open in previous studies [6, 7]. In this paper we will concentrate on the low-energy part of the vortex core spectra in slightly overdoped BSCCO. We will analyse

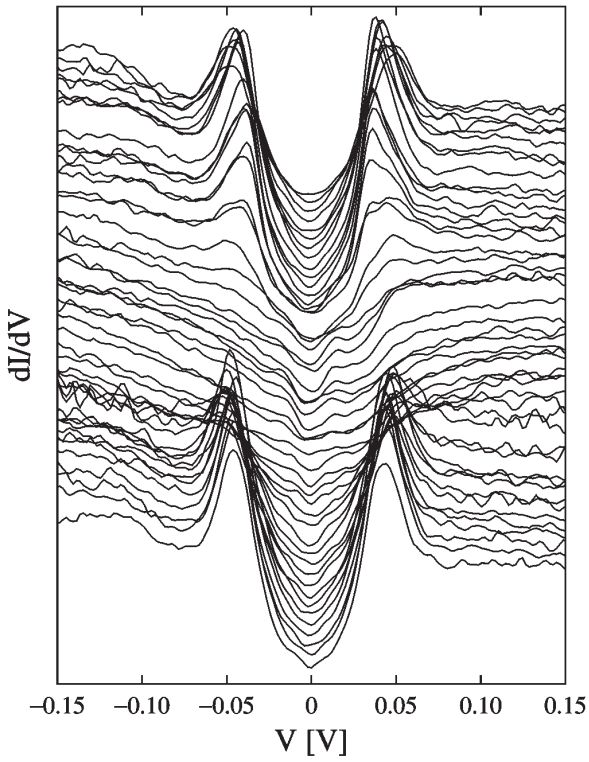

Figure 7.1: $\mathrm{d}I/\mathrm{d}V$ spectra along a trace of 100 Å through a vortex core. Subsequent spectra are vertically offset for clarity. The surrounding superconducting region (above and below) is characterised by clear coherence peaks; the vortex core (in the centre) by the suppression of these peaks and a slight increase of the zero-bias conductance. Note the small structures at ± 14 mV in the vortex core. The conductance scale can be found in Fig. 7.3.

weak structures observed between $|eV| = 5 - 20$ meV, and investigate whether or not they can be related to localised quasiparticle states.

To do so, we use the same experimental set-up as the one described in the previous chapters, measuring a sample with a critical temperature of 77 K.

7.2 Results and discussion

We obtained a mapping of the vortex cores by scanning over the surface while measuring both the conductance at an energy eV_p, corresponding to the coherence peak at negative bias in the superconducting spectra, and the conductance at zero bias V_0. As in previous measurements [6, 7], the vortex core spectra are characterised (compared to the superconducting spectra) by the disappearance of the coherence peak at negative bias (at V_p), a slight increase of the zero bias conductance (at V_0), and a decrease and shift to higher energy of the coherence peak at positive bias. Thus we obtain images of the vortex cores by determining $\frac{\mathrm{d}I/\mathrm{d}V(V_p)}{\mathrm{d}I/\mathrm{d}V(V_0)}$ as a function of the position on the surface. We define the gap value as the (absolute) energy Δ_p corresponding to the coherence peaks. The procedures

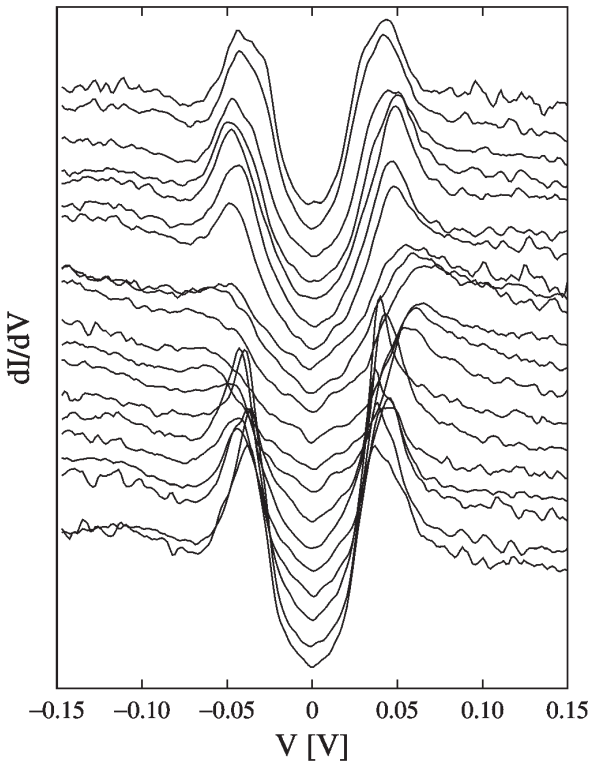

Figure 7.2: As in Fig. 7.1, but through a vortex core in a more proper region, as can be concluded from the presence of the *partly* suppressed and shifted peak at positive bias in the vortex core. The low-energy structures, though less clear, are still present.

to verify the correct interpretation of the measurements in terms of vortex cores, were the same as in chapter 6.

Additional spectral features, which were not observed in previous work, can be seen in the trace of spectra through a vortex core, shown in Fig. 7.1. On going from the superconducting region into the vortex core, the coherence peaks (at $\Delta_p = \pm 45$ meV) are suppressed, and one observes weak structures at ± 14 meV, which do not seem to disperse on moving out of the centre of the vortex core. Recently Pan and coworkers observed similar low-energy structures in BSCCO vortex cores (at ± 7 meV, with $\Delta_p = 32$ meV), and interpreted them as vortex core states [8].

A somewhat disturbing fact in the spectra in Fig. 7.1 is the absence of the typical asymmetric form characteristic of the vortex core spectrum, with the peak at positive bias partly suppressed [6, 7]. As was argued in a previous publication [9], a possible signature of a degraded surface is the suppression of the coherence peaks even at zero field. We think the same kind of (local) degradation is responsible for the absence of the asymmetric form mentioned above (and probably pins the vortex core). It is therefore of importance to verify that the observed low-energy structures are not due to this degradation.

To this end we plot in Fig. 7.2 a trace of spectra through a vortex that does include the peak at positive bias. Indeed we observe the same low-energy structures again,

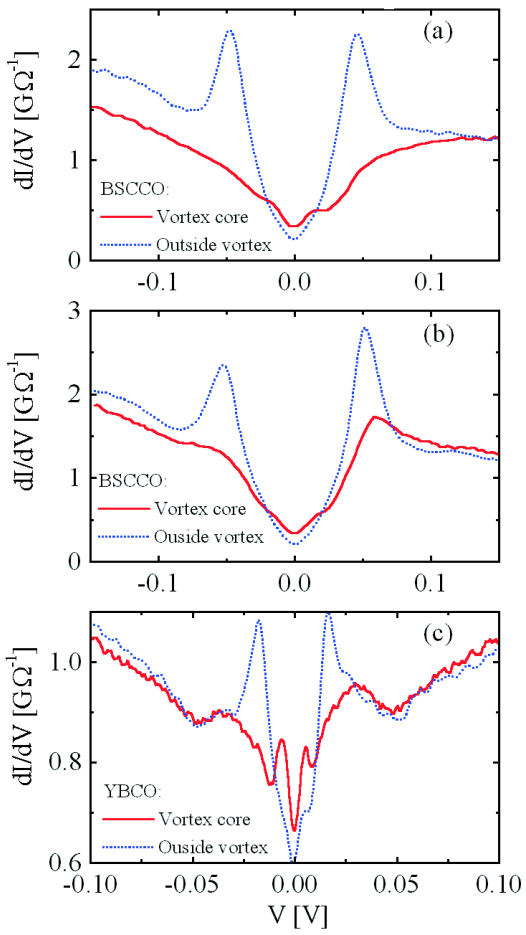

Figure 7.3: Averages of several spectra inside a vortex core (solid curves) and in the superconducting region surrounding it (dotted curves), (a) for the vortex in Fig. 7.1, (b) for a vortex in a region with a larger energy gap, and (c) for a vortex core in YBCO.

though less pronounced. Compared to the vortex in Fig. 7.1, the gap in the core is not as broad, and any low-energy feature may be washed out by the steeper slopes of the energy gap. Of course this is even more true in the superconducting spectra, with the very pronounced coherence peaks.

A detailed representation of vortex core and superconducting spectra is given in Fig. 7.3. In the same figure averages of several spectra inside and outside the vortex core are shown, for two regions with different gap sizes. The vortex core spectrum of YBCO is given for comparison. As can be seen on comparing Fig. 7.3(a) and (b), the low-energy structures follow the size of the superconducting gap. In BSCCO the gap can vary over the sample surface, depending on sample homogeneity. From the spectra of several vortex cores in regions with different gap sizes, one can derive that their energy is roughly proportional to the gap size, and does not follow the $\propto (\Delta_p)^2$ relation that can be expected for localised states in conventional superconductors [1]. This is indeed confirmed in the more detailed study presented in chapter 8.

From Fig. 7.3 it appears that the low-energy structures in BSCCO vortex cores are

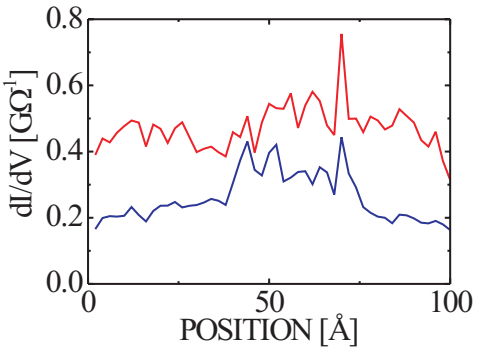

Figure 7.4: Conductance at 14 mV (upper curve) and at zero bias (lower curve), as a function of the position along the trace of Fig. 7.1. The vortex core lies between about 40 and 70 Å. The zero-bias conductance varies more than the conductance at the energy corresponding to the low-energy structures.

quite different from those in the YBCO vortex cores. In YBCO the localised quasiparticle excitations result in sharp and very pronounced peaks, as was also concluded from numerical calculations of Franz and Tešanović for a $d_{x^2-y^2} + id_{xy}$ vortex [4]. On the contrary, in BSCCO the low-energy structures in the vortex cores are very weak, and a slight degradation of the energy resolution was already sufficient to make them disappear from our spectra. A closer comparison with the YBCO spectra reveals that the low-energy structures in the BSCCO vortex cores resemble more the small humps inside the gap in the *superconducting* YBCO spectra than the YBCO vortex core states. However, in chapter 8 we will show that these low-energy structures in vortex core do have a very similar scaling with the superconducting gap for BSCCO and YBCO.

To investigate how the low-energy structures evolve on moving away from the centre of the vortex core, we plot the conductance at the energy corresponding to the hump at positive bias, as a function of position. As is clear from Fig. 7.4, and in contrast to the impression given by Figs. 7.1 and 7.2, the low-energy structures do not decrease considerably on leaving the vortex core. They may very well be present outside the vortex core as well, though hidden in the slope of the coherence peaks. In fact the increase of the zero-bias conductivity in the vortex core is more pronounced, and may as a consequence also push up the low-energy structures, thus making them show up more clearly inside than outside the vortex core.

As already stated above, the observed low-energy structures are weak compared to the other characteristic features of the spectra inside and outside the BSCCO vortex cores. This might be a reason why they were not seen in our previous measurements [6, 7]. Other reasons might be related to slight changes in the energy resolution and tunnelling conditions, or to small and so far unexplained sample-to-sample variations.

7.3 Conclusion

We report the observation of low-energy structures ($E < \Delta_p$) in the vortex cores of an oxygen overdoped BSCCO single crystal. These structures appear very weak for localised states, much weaker than the core states observed in YBCO. One of their characteristics is the absence of any energy dispersion as a function of position with respect to the centre of the vortex core. A detailed characterisation of the low-energy structures is required to be more decisive about their nature and their relation to the vortex states in YBCO. This characterisation, in particular their energy-dependence on the superconducting gap and their dependence on the magnetic field, is discussed in chapter 8.

References

[1] C. Caroli, P. G. de Gennes, and J. Matricon, Phys. Lett. **9**, 307 (1964).

[2] H. F. Hess, R. B. Robinson, R. C. Dynes, J. M. Valles, and J. V. Waszczak, Phys. Rev. Lett. **62**, 214 (1989).

[3] Ch. Renner, A. D. Kent, Ph. Niedermann, Ø. Fischer, and F. Lévy, Phys. Rev. Lett. **67**, 1650 (1991).

[4] M. Franz and Z. Tešanović, Phys. Rev. Lett. **80**, 4763 (1998).

[5] I. Maggio-Aprile, Ch. Renner, A. Erb, E. Walker, and Ø. Fischer, Phys. Rev. Lett. **75**, 2754 (1995).

[6] Ch. Renner, B. Revaz, K. Kadowaki, I. Maggio-Aprile, and Ø. Fischer, Phys. Rev. Lett. **80**, 3606 (1998).

[7] M. Kugler, Ph.D. thesis, University of Geneva, n° 3158 (2000).

[8] S. H. Pan, E. W. Hudson, A. K. Gupta, K.-W. Ng, H. Eisaki, S. Uchida, and J. C. Davis, Phys. Rev. Lett. **85**, 1536 (2000).

[9] Ch. Renner and Ø. Fischer, Phys. Rev. B **51**, 9208 (1995).

Chapter 8

Linear and Field-Independent Relation between Vortex Core States and Gap

8.1 Introduction

In conventional, s-wave superconductors, the suppression of the order parameter in a vortex core creates a potential well for low-energy quasiparticles, leading to the formation of localised states [1–3]. On the contrary, if the superconducting order parameter has nodes in it – as for $d_{x^2-y^2}$ symmetry in high-temperature superconductors (HTS) – one expects the low-energy quasiparticles states in a vortex to be extended along the nodes of the gap function, so to be delocalised. This would result in a broad peak at the Fermi level in the quasiparticle local density of states (LDOS) of a vortex core [4–6]. The observation of *discrete* vortex core states in $YBa_2Cu_3O_{7-\delta}$ (YBCO) [7] and $Bi_2Sr_2CaCu_2O_{8+\delta}$ (BSCCO) [8, 9] by scanning tunnelling spectroscopy (STS), as discussed in chapter 7, has come as a complete surprise. As a result, the nature of these states has been subject of increasing theoretical study [4–6, 10–16], leading to a range of possible scenarios for explaining the experimental data. The need for an understanding of the electronic structure of the vortices in HTSs has become even more pressing because of the antiferromagnetic fluctuations recently observed in vortex cores in $La_{2-x}Sr_xCuO_4$ [17].

To our knowledge, the most direct way to access the electronic structure of a vortex core is by using a scanning tunnelling microscope (STM). In a typical experimental set-up for studying vortex cores in HTSs (as well as in this study), the STM tip and tunnelling direction are perpendicular to the CuO_2 planes. The quasiparticle excitation spectrum then follows from the $\mathrm{d}I/\mathrm{d}V$ tunnelling spectra [18]. Experiments on HTSs have revealed the following characteristics of vortex cores. In YBCO the vortex core states appear as two clearly distinct, sub-gap excitations, which do not disperse on moving out of the vortex core, but rather transform into weak shoulders in the superconducting spectra (and sometimes also observed at zero magnetic field) [7]. In BSCCO the vortex core spectra reveal a remarkable resemblance to the pseudogap spectra observed above the critical temperature T_c [19]. In recent extensive studies, benefiting from more stable tunnelling conditions, vortex core states appear as weak shoulders in this pseudogap. They do not change in energy as a function of increasing distance from the vortex core centre [8] (see chapter 7), in contrast to the vortex core states in conventional

superconductors [2]. Though quite irregular shapes can be observed due to vortex motion (chapter 6) [20], the cores do not show the four-fold symmetry that may be expected for d-wave superconductors.

The main results of this chapter can be summarised as follows. First, the energy of the vortex core states scales with the superconducting gap outside the core, clearly distinguishing these states from localised vortex states ($E \propto \Delta^2/E_F$) in conventional superconductors [1]. Since in BSCCO the superconducting gap scales with the oxygen doping level [21–26], this directly gives the doping dependence of the vortex states as well. Second, the vortex core spectra do not show any significant dependence on the external magnetic field over a range from 1 to 6 T, which questions field-dependent scenarios for explaining the vortex core states.

8.2 Experimental details

A systematic study of vortex core spectra requires, apart from sufficient instrumental resolution, relatively high sample homogeneity. More precisely, in order to compare spectra inside a vortex core to those in the nearby superconducting region, (zero-field) spectral reproducibility over at least 100 Å is necessary. This condition can be met in BSCCO single crystals with transition widths $\Delta T_c \leq 1$ K (as measured by AC susceptibility, see chapter 5). Most of the data presented here were obtained on two different overdoped samples: (i) A sample with $T_c = 77.7$ K ($\Delta T_c = 0.4$ K), cooled down at 6 T, and after measurements at 6 T the field was reduced (at low temperature) to 4 and 1 T. (ii) A sample with $T_c = 77$ K ($\Delta T_c = 1$ K), zero-field cooled, measured at fields of subsequently 0, 6, 2, and 0 T. For the latter sample, lines of spectra in and near vortex cores can be found in chapter 7. Some additional data were taken on two other overdoped samples with $T_c = 76.1$ K ($\Delta T_c = 0.3$ K), and on an optimally doped sample with $T_c = 87.4$ K ($\Delta T_c = 1.0$ K). Samples were cleaved in ultra-high vacuum environment (10^{-9} mbar), shortly before cooling down STM and sample to 4.2 K in exchange gas ($\sim 10^{-2}$ mbar helium). The magnetic field and tunnelling direction were perpendicular to the CuO_2 planes [27–29].

The quasiparticle LDOS at an energy $E = eV$ on the surface of the sample was obtained by measuring the differential tunnelling conductance $\mathrm{d}I/\mathrm{d}V$ at sample bias V as a function of position, using a lock-in technique. In homogeneous BSCCO samples, the clearest vortex images were found by measuring the conductance at $V = -\Delta_p/e$, where Δ_p corresponded to the energy of the superconducting coherence peaks. We thus obtained maps of spots where superconductivity was suppressed. A comparison of the number of these spots per area to the magnetic flux for different fields, as well as their disappearance at zero field, justified the identification as vortex cores [19, 20].

8.3 Results

In Fig. 8.1 we show such maps of vortex cores at 1 and 6 T. As can be verified directly, the number of vortices (30 ± 2) in Fig. 8.1(b) corresponds to the average flux crossing

this area ($29\Phi_0$) at 6 T. In general, the density of vortices scales with the magnetic field as one should expect. We do not observe any systematic change in the size and shape of the vortex cores for the different applied fields.

$\mathrm{d}I/\mathrm{d}V$ spectra were taken in and around several of the thus imaged vortex cores. Spectra along a 200 Å trace through a vortex core are shown in Fig. 8.2(a). The spectra discussed hereafter were obtained by averaging the spectra just outside the core for the superconducting spectra and the spectra well inside the core for the typical vortex core spectra. An average spectrum outside the core consists of typically 5 to 10 spectra taken over a total distance of 20 to 40 Å, with pronounced coherence peaks, as above and below in Fig. 8.2(a). An average spectrum inside the core consists of typically 5 to 10 spectra taken over a distance of about 20 Å, without coherence peaks, as in the middle of Fig. 8.2(a). The averaged spectra can be found in Fig. 8.2(b-d), for vortex cores at 1 T and 6 T in BSCCO, as well as for a vortex core in YBCO [7]). More and similar spectroscopic information, of regions with larger gaps, has been given in chapter 7. Compared to the superconducting state, the LDOS in the vortex cores seems considerably reduced, with loss of spectral weight near the Fermi level. The characteristics of the vortex spectra in BSCCO, asymmetric pseudogap with weak shoulders at low bias, do not show any dependence on the field strength. We do not observe any change (due to the magnetic field) in the spectra outside the vortex core either. The spectra taken at different field strengths are in fact remarkably similar, both those inside, and those around vortices.

To study the dependence of the vortex core spectra on the superconducting energy gap (taken as the energy of the coherence peaks Δ_p), we measured vortex cores on different samples, and also made use of variations of the gap (inhomogeneity on a scale > 100 Å) in the samples, see the inset in Fig. 8.4. Δ_p has been determined from the average of spectra near the vortex core. The error in this Δ_p quantifies the variation of the gap width, due to inhomogeneity in the immediate neighbourhood of the core ($50 \sim 100$ Å from its centre). It was determined from traces of spectra as in Fig. 8.2.

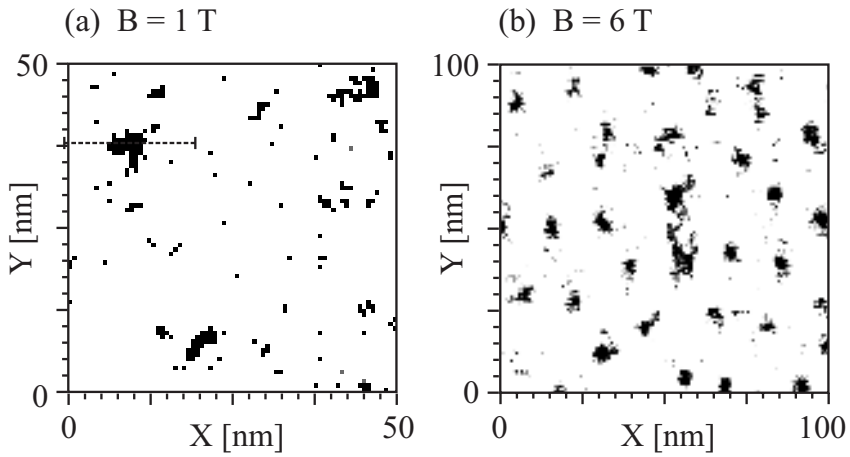

Figure 8.1: Images of vortex cores at (a) 1 T and (b) 6 T (field cooled measurement, see text). (a) $\mathrm{d}I/\mathrm{d}V$ at -40 mV, normalised to its value at -75 mV. The trace in Fig. 8.2 was taken at about $(10, 38)$ nm. (b) $\mathrm{d}I/\mathrm{d}V$ at -30 mV, normalised to its value at zero bias. Note the different scales in (a) and (b).

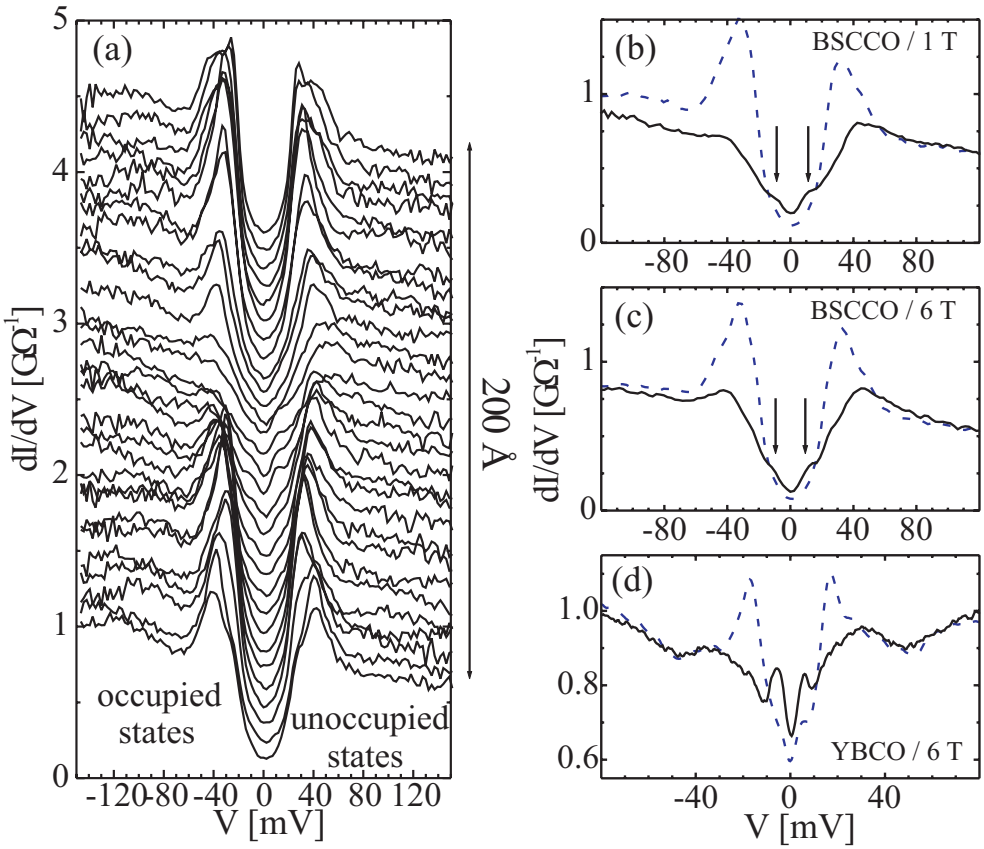

Figure 8.2: (a) Spectra at 1 T along the 200 Å trace indicated in Fig. 8.1(a). The vortex core is about halfway the trace. The spectra have been offset for clarity, and V is the sample bias. (b) Averaged spectrum in the centre of the core (solid line), and in its immediate vicinity (dashed line, superconducting gap). (c) For a vortex core in BSCCO, at 6 T. (d) For a vortex core in YBCO at 6 T. Note the different scales for the bias voltage.

The data can be represented more clearly by normalising the (low-bias part of) the spectra to the pseudogap background. The latter was determined by a smooth fit that follows the general shape of the spectra, but excludes the low-bias features. In practice this was achieved by a fifth order polynomial fit over a range $0.5\Delta_p < eV < 1.2\Delta_p$, forced to go through the zero-bias conductance. The results have been checked for robustness against variation of the fitting parameters and range, and have been plotted on a normalised energy scale in Fig. 8.3.

These data confirm the independence of the vortex states on the magnetic field, and show that their energy E_{core} directly scales with the superconducting gap. This scaling comes out even more clearly when E_{core} [as determined from raw data, e.g. Fig. 8.3(a)] is plotted as a function of Δ_p in Fig. 8.4. The dependence on Δ_p is certainly not square-like, as one would expect for conventional localised states in vortex cores [1]. It is roughly linear, with a slope of 0.30, as determined from a linear fit through all BSCCO data and restricted to go through the origin ($\chi^2 = 0.19$, correlation coefficient $r = 0.81$). An unrestricted fit would cut the vertical axis at (1.5 ± 3.7 meV), for a slope of 0.26 (χ^2 and r the same as before, within the given precision). For comparison, a linear fit to E_{core}/Δ_p as a function of Δ_p ($E_{core} \propto \Delta_p^2$, through the origin) yields $\chi^2 = 0.55$, and a

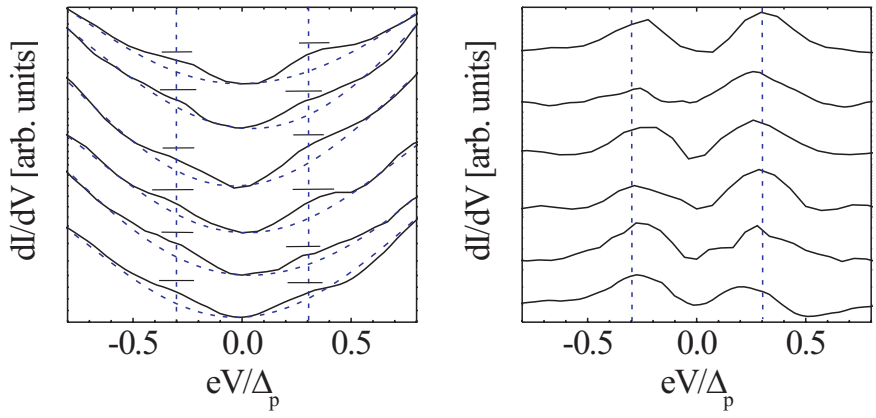

Figure 8.3: (a) Vortex core spectra (solid lines) for different fields and gaps. From top to bottom: B = 1, 2, 4, 6, 6, and 6 T; $\Delta_p = (32 \pm 2)$, (47 ± 5), (32 ± 1), (33 ± 2), (43 ± 2), and (52 ± 5) meV. The small horizontal lines indicate the errors in E_{core} used in Fig. 8.4. The vertical, dashed lines indicate $eV/\Delta_p = 0.3$, as follows for E_{core} from the fitting discussed below. (b) Normalised vortex core spectra, obtained by dividing the raw core spectra by fits to the pseudogap background [see text and dashed lines in (a)].

negative $r = -0.18$. This is an important result, because it proves that the vortex core states in BSCCO do not correspond to conventional localised states.

Since doping dependent tunnelling experiments on BSCCO show a roughly linear decrease of Δ_p with oxygen doping [21–26], we can directly read the horizontal scale as the (local) hole doping of the BSCCO samples, going from overdoped to underdoped. This indicates that the electronic nature of the vortex cores remains the same for a considerable doping range.

In Fig. 8.4 we have also included data obtained on YBCO, for comparison [7]. Though the vortex core states in YBCO appear much more pronounced than those in BSCCO (see Fig. 8.2), their energy scale shows a remarkable similarity, strongly suggesting a common origin. It is tempting, but rather speculative, to compare this to the energy scale of the antiferromagnetic fluctuations with an energy of $3 \sim 4$ meV, for a spin gap of 6.7 meV, as observed in $La_{2-x}Sr_xCuO_4$ [17]. A recent study of Pan *et al.* [9] indicated vortex core states in BSCCO at $E_{core} = 7$ meV, for a gap of $\Delta_p = 32$ meV, on samples with transition widths of $4 \sim 5$ K. Though the latter value implies that it may be difficult to obtain a uniform (at least over ~ 100 Å) Δ_p within error bars as indicated in Fig. 8.4, their results are consistent with our work (for a discussion on some small variations in the asymmetric pseudogap background see chapter 7).

8.4 Discussion

Our results, especially the linear scaling of E_{core} with Δ_p, rule out conventional localised states as an explanation for the vortex core states observed in HTSs (they would neither be consistent with the lack of dispersion of E_{core} as a function of position, see Fig. 8.2).

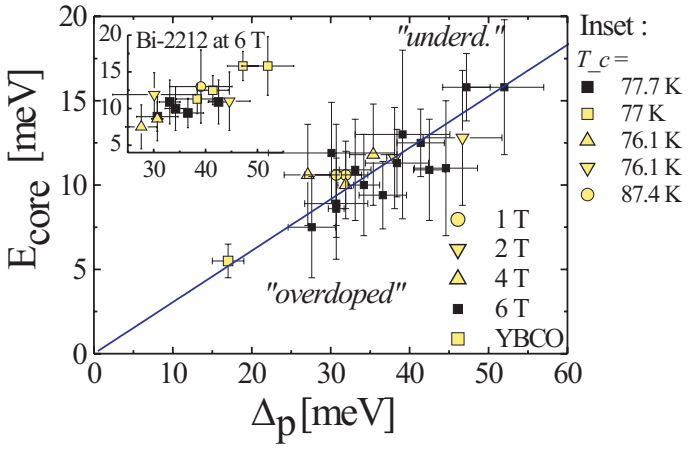

Figure 8.4: The energy of vortex core states E_{core} as a function of the superconducting gap (the energy of the coherence peaks) Δ_p. Plotted are data for different magnetic fields, and different BSCCO single crystals. At $\Delta_p = 17$ meV the value extracted from YBCO data. The straight line is a linear fit to all BSCCO data points, forced to go through the origin, with a slope of 0.30. In the inset again the BSCCO data at 6 T, distinguishing between the different samples (T_c).

Furthermore, they provide sufficient details to discuss other scenarios.

First of all, in a pure d-wave superconductor the vortex core states would appear as a broad zero-bias conductance peak [4–6], in clear disagreement with experiment. One may argue that the quasiparticle states from different vortex cores form bands, which would lead to the splitting of the zero-bias conductance peak into two different peaks. In that case, however, the energy gap between these peaks should depend on the magnetic field, which is inconsistent with the results presented above.

A possible explanation for the observed vortex core states is the symmetry breaking of the order parameter in the vicinity of a vortex core [10, 11]. This will lead to secondary (possibly imaginary) d_{xy} or s components of the order parameter, effectively blocking the nodes of the $d_{x^2-y^2}$ gap function, and allowing localised states [5]. Though in a simple BCS d-wave superconductor these components are too small to influence the spectra [6], they appear more important when the Coulomb interaction on the Cu sites is taken into account. Numerical calculations using the $t - J$ model estimate their size – strongly doping dependent – to be between 5 and 30% of the $\Delta_{x^2-y^2}$ order parameter [13, 15]. Our results imply that such a secondary component would scale with the $\Delta_{x^2-y^2}$ gap over a wide doping range and, in contrast to what one should expect [6, 16], would be independent of the magnetic field between 1 and 6 T.

The energy scaling and field independence of the core states suggest an other possibility, which is yet to be explored in more detail. Keeping in mind that the pseudogap above T_c (and in the vortex cores) scales with the superconducting gap as well [22, 25, 26, 30], one can speculate that the presence of the pseudogap leads to a splitting of the BCS d-wave zero bias conductance peak (ZBCP). Since the pseudogap does not fully suppress

the spectral weight at low energy [19], it can leave some traces of the originally very pronounced ZBCP in the vortex core. This idea has been elaborated in two very recent calculations, both independent of the magnetic field.

First, using the two-body Cooperon operator for modelling phase fluctuations, one obtains [31], in close agreement with experiment: (i) a roughly linear relation between vortex core state energy and the gap; (ii) no change in this energy as a function of position in the vortex core; and (iii) an exponential decay of the vortex core states outside the core. Furthermore, the difference between the pronounced vortex core states in YBCO and the weak shoulders in BSCCO is explained as follows. The pseudogap being much more dominant in BSCCO than in YBCO, it will suppress the low-energy core states in the former material much more than in the latter [31], in agreement with our observations (Fig. 8.2).

Second, the competition between anti-ferromagnetism and superconductivity has been modelled with a two-dimensional, mean-field Hubbard Hamiltonian, including a d-wave pair potential [32]. In this model, the anti-ferromagnetism is believed to be responsible for the pseudogap above T_c. In the vortex core, spin-density wave order leads to a splitting of the ZBCP. The splitting can be regarded as a Zeeman splitting due to the on-site Coulomb interaction. The existence of a anti-ferromagnetic spin density wave order in the core would be consistent with neutron scattering data [17].

More recently, a spatial modulation – a 'checkerboard' pattern – was observed in the integrated spectral weight of vortex core states [33], possibly related to the local presence of a spin density wave in the vortex core. So far, it is not clear how this modulation relates to the energy-dependent periodicity observed by the same group at zero-field [34].

8.5 Conclusion

In conclusion, we have measured vortex core quasiparticle states as a function of the superconducting gap and the magnetic field. Their energy dependence on the superconducting gap near the vortex core is approximately linear, with a slope of about 0.3. This is in disagreement with the behaviour expected for conventional (BCS) localised vortex core states. It is consistent, however, with recent theories including the effects of correlations [31, 32], as explained above. The vortex core states do not show any dependence on the applied magnetic field in the range from 1 to 6 T. Our results suggest a common origin for vortex core states in YBCO and BSCCO. The linear energy scaling of these states with the superconducting gap, the lack of any variation (dispersion) of E_{core} as a function of distance from the vortex core centre, and the suppression of LDOS in the core compared to the superconducting state further underline the non-BCS behaviour of HTSs, and of their vortex cores in particular.

References

[1] C. Caroli, P. G. de Gennes, and J. Matricon, Phys. Lett. **9**, 307 (1964).

[2] H. F. Hess, R. B. Robinson, R. C. Dynes, J. M. Valles, and J. V. Waszczak, Phys. Rev. Lett. **62**, 214 (1989).

[3] Ch. Renner, A. D. Kent, Ph. Niedermann, Ø. Fischer, and F. Lévy, Phys. Rev. Lett. **67**, 1650 (1991).

[4] Y. Wang and A. H. MacDonald, Phys. Rev. B **52**, R3876 (1995).

[5] M. Franz and Z. Tešanović, Phys. Rev. Lett. **80**, 4763 (1998).

[6] K. Yasui and T. Kita, Phys. Rev. Lett. **83**, 4168 (1999).

[7] I. Maggio-Aprile, Ch. Renner, A. Erb, E. Walker, and Ø. Fischer, Phys. Rev. Lett. **75**, 2754 (1995).

[8] B. W. Hoogenboom, Ch. Renner, B. Revaz, I. Maggio-Aprile, and Ø. Fischer, Physica C **332**, 440 (2000).

[9] S. H. Pan, E. W. Hudson, A. K. Gupta, K.-W. Ng, H. Eisaki, S. Uchida, and J. C. Davis, Phys. Rev. Lett. **85**, 1536 (2000).

[10] G. E. Volovik, Pis'ma Zh. Éksp. Teor. Fiz. **58**, 457 (1993), [JETP Lett. **58**, 1174 (1993)].

[11] P. I. Soininen, C. Kallin, and A. J. Berlinsky, Phys. Rev. B **50**, 13883 (1994).

[12] Y. Morita, M. Kohmoto, and K. Maki, Phys. Rev. Lett. **78**, 4841 (1997).

[13] A. Himeda, M. Ogata, Y. Tanaka, and S. Kashiwaya, J. Phys. Soc. Jpn. **66**, 3367 (1997).

[14] M. Franz and Z. Tešanović, Phys. Rev. Lett. **84**, 554 (2000).

[15] J. H. Han and D.-H. Lee, Phys. Rev. Lett. **85**, 1100 (2000).

[16] A. V. Balatsky, Phys. Rev. B **61**, 6940 (2000).

[17] B. Lake, G. Aeppli, K. N. Claussen, D. F. McMorrow, K. Lefmann, N. E. Hussey, N. Mangkorntong, M. Nohara, H. Takagi, T. E. Mason, and A. Schröder, Science **291**, 1759 (2001).

[18] E. L. Wolf, *Principles of Electron Tunneling Spectroscopy* (Oxford University Press, New York, 1985).

[19] Ch. Renner, B. Revaz, K. Kadowaki, I. Maggio-Aprile, and Ø. Fischer, Phys. Rev. Lett. **80**, 3606 (1998).

[20] B. W. Hoogenboom, M. Kugler, B. Revaz, I. Maggio-Aprile, Ø. Fischer, and Ch. Renner, Phys. Rev. B **62**, 9179 (2000).

[21] M. Oda, K. Hoya, R. Kubota, C. Manabe, N. Momono, T. Nakano, and M. Ido, Physica C **282-287**, 1499 (1997).

[22] Ch. Renner, B. Revaz, J.-Y. Genoud, K. Kadowaki, and Ø. Fischer, Phys. Rev. Lett. **80**, 149 (1998).

[23] Y. DeWilde, N. Miyakawa, P. Guptasarma, M. Iavarone, L. Ozyuzer, J. F. Zasadzinski, P. Romano, D. G. Hinks, C. Kendziora, G. W. Crabtree, and K. E. Gray, Phys. Rev. Lett. **80**, 153 (1998).

[24] N. Miyakawa, P. Guptasarma, J. F. Zasadzinski, D. G. Hinks, and K. E. Gray, Phys. Rev. Lett. **80**, 157 (1998).

[25] N. Miyakawa, J. F. Zasadzinski, L. Ozyuzer, P. Guptasarma, D. G. Hinks, C. Kendziora, and K. E. Gray, Phys. Rev. Lett. **83**, 1018 (1999).

[26] A. Matsuda, S. Sugita, and T. Watanabe, Phys. Rev. B **60**, 1377 (1999).

[27] Ch. Renner, Ph. Niedermann, A. D. Kent, and Ø. Fischer, J. Vac. Sci. Technol. A **8**, 330 (1990).

[28] A. D. Kent, Ch. Renner, Ph. Niedermann, J.-G. Bosch, and Ø. Fischer, Ultramicroscopy **42-44**, 1632 (1992).

[29] Ch. Renner and Ø. Fischer, Phys. Rev. B **51**, 9208 (1995).

[30] M. Kugler, Ø. Fischer, Ch. Renner, S. Ono, and Y. Ando, Phys. Rev. Lett. **86**, 4911 (2001).

[31] C. Berthod and B. Giovannini, Phys. Rev. Lett. **87**, 277002 (2001).

[32] J.-X. Zhu and C. S. Ting, Phys. Rev. Lett. **87**, 147002 (2001).

[33] J. E. Hoffman, E. W. Hudson, K. M. Lang, V. Madhavan, S. H. Pan, H. Eisaki, S. Uchida, and J. C. Davis, Science **295**, 466 (2002).

[34] J. C. Davis, EPS meeting in Brighton (2002).

Chapter 9

Conclusion and Perspectives

The work described in this thesis has led to several new insights in high-temperature superconductivity. More specifically, it has resulted in experimental facts revealing novel phenomena in the behaviour of vortex cores in $Bi_2Sr_2CaCu_2O_{8+\delta}$ (BSCCO). It has also revealed new problems and challenges, both instrumental and physical. The main results of this thesis are summarised below.

Chapter 2. The existing instrumentation for low-temperature scanning tunnelling microscope (STM) experiments has been considerably improved. First, a low-temperature STM in exchange gas [1] has been equipped with a fast-entry load-lock and a manipulation platform for sample and tip exchange in ultra-high vacuum (UHV). The second main result is a novel STM design for measurements in UHV, at temperatures between 1.5 and 300 K, and (simultaneously) at magnetic fields up to 6 T. For the new design, we have built and extensively tested a ^{4}He insert with STM, a UHV manipulation platform, and a UHV chamber.

Chapter 3 and 4. Doping dependent tunnelling measurements on BSCCO [2] are reproduced numerically, using a realistic band structure [3, 4]. The numerical simulations provide further evidence for the extremely short lifetime of the quasiparticles above the superconducting gap [5]. This short lifetime, in coexistence with sharp coherence peaks, is explained in terms of quasiparticle interaction with a collective mode [6]. Furthermore, it is demonstrated that the tunnelling matrix elements near the Fermi level are essentially independent of the in-plane wave-vector.

Chapter 5. In BSCCO, electronic disorder at nanometre scale has a small effect on the width of the macroscopic transition between the normal and the superconducting state. Electronic homogeneity is only observed in well annealed samples, with transition widths below 1% of T_c (as measured by AC susceptibility). This result indicates that (static) electronic disorder or inhomogeneity [7–13] is not inherent to high-temperature superconductivity.

Chapter 6. Vortex images at 6 T do not show any sign of an ordered lattice. This is explained by the highly two-dimensional character of vortices in BSCCO, which allows them to be easily pinned by defects (possibly oxygen vacancies) [14]. The shape of vortex cores is influenced by pinning as well. Many vortex cores appear to be split into separate elements (an effect which is more pronounced in zero-field cooled experiments). This

split state can be explained in terms of quantum tunnelling between different pinning sites [15, 16].

Chapter 7. For the first time, low-energy quasiparticle excitations (vortex core states) are identified in the vortex cores of BSCCO [17, 18]. In contrast to theoretical predictions based on BCS theory [19–21], the excitations are clearly separated in energy. They are considerably less pronounced than vortex core states in $YBa_2Cu_3O_{7-\delta}$ (YBCO) [22], and have an energy independent of their position with respect to the centre of the vortex.

Chapter 8. Vortex core states in BSCCO are independent of the applied magnetic field between 1 and 6 T. This considerably limits the number of possibilities to explain their separate (discrete) appearance. The linear relation between the energy of the vortex core states and the superconducting gap [23] clearly distinguishes them from vortex core states in conventional superconductors [24]. Furthermore, it is compatible with a scenario invoking the pseudogap to explain vortex core states in BSCCO [25, 26].

Perspectives. Several possible improvements of the actual STM equipment have been proposed in chapter 2, concerning mainly the STM head and the vibration isolation. A new type of STM head is currently being constructed.

To get a more detailed understanding of the effect of the collective mode on the spectra (chapter 4), we are considering auto-consistent calculations.

Though our results point out that electronic inhomogeneity in BSCCO is not inherent to superconductivity (chapter 5), a systematic study on samples from the homogeneous to the inhomogeneous limit still has to be performed. This may provide very useful information for theories based on phase separation [27–29].

It will require measurements below 1 K to rigorously prove that the vortex motion in chapter 6 is indeed due to quantum tunnelling (in contrast to thermal fluctuations). Similar experiments with deliberately created pinning sites would form an ideal playground to study vortex dynamics [14] on a local scale (using the STM tip to create defects on the surface).

The nature of vortex core states in high-temperature superconductors (HTSs) still needs much clarification (chapter 7). Though the results in chapter 8 strongly suggest a generic behaviour for YBCO and BSCCO, it would certainly be worthwhile to verify other HTSs. The relation between vortex core states and antiferromagnetic fluctuations in $La_{2-x}Sr_xCuO_4$ vortex cores [30] is still to be established, as well as the weak spatial modulation recently observed for vortex cores states in BSCCO [31].

References

[1] A. D. Kent, Ch. Renner, Ph. Niedermann, J.-G. Bosch, and Ø. Fischer, Ultramicroscopy **42-44**, 1632 (1992).

[2] Ch. Renner, B. Revaz, J.-Y. Genoud, K. Kadowaki, and Ø. Fischer, Phys. Rev. Lett. **80**, 149 (1998).

[3] O. K. Andersen, O. Jepsen, A. I. Liechtenstein, and I. I. Mazin, Phys. Rev. B **49**, 4145 (1994).

[4] O. K. Andersen, A. I. Liechtenstein, O. Jepsen, and F. Paulsen, J. Phys. Chem. Solids **56**, 1573 (1995).

[5] M. R. Norman, H. Ding, H. Fretwell, M. Randeria, and J. C. Campuzano, Phys. Rev. B **60**, 7585 (1999).

[6] M. R. Norman and H. Ding, Phys. Rev. B **57**, R11089 (1998).

[7] J.-X. Liu, J.-C. Wan, A.-M. Goldman, Y. C. Chang, and P. Z. Jiang, Phys. Rev. Lett. **67**, 2195 (1991).

[8] A. Chang, Z. Y. Rong, Y. M. Ivanchenko, F. Lu, and E. L. Wolf, Phys. Rev. B **46**, 5692 (1992).

[9] T. Cren, D. Roditchev, W. Sacks, J. Klein, J.-B. Moussy, C. Deville-Cavellin, and M. Laguës, Phys. Rev. Lett. **84**, 147 (2000).

[10] T. Cren, D. Roditchev, W. Sacks, and J. Klein, Europhys. Lett. **54**, 84 (2001).

[11] C. Howald, P. Fournier, and A. Kapitulnik, Phys. Rev. B **64**, 100504 (2001).

[12] S. H. Pan, J. P. O'Neal, R. L. Badzey, C. Chamon, H. Ding, J. R. Engelbrecht, Z. Wang, H. Eisaki, S. Uchida, A. K. Gupta, K.-W. Ng, E. W. Hudson, K. M. Lang, and J. C. Davis, Nature **413**, 282 (2001).

[13] K. M. Lang, V. Madhavan, J. E. Hoffman, E. W. Hudson, H. Eisaki, and S. Uchida J. C. Davis, Nature **415**, 412 (2002).

[14] G. Blatter, M. V. Feigel'man, V. B. Geschkenbein, A. I. Larkin, and V. M. Vinokur, Rev. Mod. Phys. **66**, 1125 (1994), and references therein.

[15] B. W. Hoogenboom, M. Kugler, B. Revaz, I. Maggio-Aprile, Ø. Fischer, and Ch. Renner, Phys. Rev. B **62**, 9179 (2000).

[16] B. W. Hoogenboom, Ch. Renner, I. Maggio-Aprile, and Ø. Fischer, in *Vortices in Unconventional Superconductors and Superfluids*, Vol. 132 of *Series in Solid-State Science*, edited by R. P. Huebener, N. Schophohl, and G. E. Volovik (Springer, Berlin Heidelberg, 2002), pp. 269–282.

[17] B. W. Hoogenboom, Ch. Renner, B. Revaz, I. Maggio-Aprile, and Ø. Fischer, Physica C **332**, 440 (2000).

[18] S. H. Pan, E. W. Hudson, A. K. Gupta, K.-W. Ng, H. Eisaki, S. Uchida, and J. C. Davis, Phys. Rev. Lett. **85**, 1536 (2000).

[19] Y. Wang and A. H. MacDonald, Phys. Rev. B **52**, R3876 (1995).

[20] M. Franz and Z. Tešanović, Phys. Rev. Lett. **80**, 4763 (1998).

[21] K. Yasui and T. Kita, Phys. Rev. Lett. **83**, 4168 (1999).

[22] I. Maggio-Aprile, Ch. Renner, A. Erb, E. Walker, and Ø. Fischer, Phys. Rev. Lett. **75**, 2754 (1995).

[23] B. W. Hoogenboom, K. Kadowaki, B. Revaz, M. Li, Ch. Renner, and Ø. Fischer, Phys. Rev. Lett. **87**, 267001 (2001).

[24] C. Caroli, P. G. de Gennes, and J. Matricon, Phys. Lett. **9**, 307 (1964).

[25] C. Berthod and B. Giovannini, Phys. Rev. Lett. **87**, 277002 (2001).

[26] J.-X. Zhu and C. S. Ting, Phys. Rev. Lett. **87**, 147002 (2001).

[27] V. J. Emery, S. A. Kivelson, and H. Q. Lin, Phys. Rev. Lett. **64**, 475 (1990).

[28] Y. N. Ovchinnikov, S. A. Wolf, and V. Z. Kresin, Phys. Rev. B **63**, 64524 (2001).

[29] S. Chakravarty, R. B. Laughlin, D. K. Morr, and C. Nayak, Phys. Rev. B **63**, 94503 (2001).

[30] B. Lake, G. Aeppli, K. N. Claussen, D. F. McMorrow, K. Lefmann, N. E. Hussey, N. Mangkorntong, M. Nohara, H. Takagi, T. E. Mason, and A. Schröder, Science **291**, 1759 (2001).

[31] J. E. Hoffman, E. W. Hudson, K. M. Lang, V. Madhavan, S. H. Pan, H. Eisaki, S. Uchida, and J. C. Davis, Science **295**, 466 (2002).

Acknowledgements
Remerciements

Tout d'abord, je tiens à remercier le professeur Øystein Fischer pour m'avoir accueilli dans son groupe, et pour la confiance, l'enthousiasme et l'optimisme qu'il m'a témoignés pendant ce travail de thèse.

Je remercie également le professeur Bernard Giovannini de l'Université de Genève et le Docteur Jan Aarts de l'Université de Leiden d'avoir accepté de faire partie du jury de cette thèse.

La spectroscopie à effet tunnel est une technique compliquée, et je suis très heureux d'avoir bénéficié de l'expérience de Christophe Renner pour m'y guider pendant ma première année de thèse.

Que ce soit pour le développement d'un nouveau microscope à effet tunnel ou pour les négociations avec nos amis d'Angleterre, j'ai toujours pu compter sur le support de Martin Kugler, capitaine du Titanic.

Les autres *STM boys* ont chacun contribué de plusieurs manières au bon déroulement de ce travail. D'abord en partageant les plaisirs et les frustrations de la recherche, mais aussi en donnant des coups de main avec des mesures, des modifications techniques, de l'électronique, des transferts d'hélium, des ordinateurs en panne, des corrections de manuscripts, le transport d'instruments lourds, et en me montrant d'autres types d'expériences. Pour tout cela, et pour toute autre chose que j'ai oubliée momentanément, je suis très reconnaissant à Akihiko Tagaki, Benjamin Grévin, Cédric Dubois, Isabelle Joumard, Ivan Maggio-Aprile, Morten Eskildsen, Olivier Kuffer, et Shukichi Tanaka.

J'ai eu la chance de pouvoir mesurer les monocristaux de Bernard Revaz de Genève, de Kazuo Kadowaki de Tsukuba, et de Ming Li de Leiden. La connaissance de la préparation d'échantillons à Genève a été très importante pour cette thèse, et j'en remercie en particulier Bernard Revaz et Jean-Yves Genoud.

Je remercie Christophe Berthod et Martin Peter pour les discussions plutôt théoriques. Alfred Manuel nous a écrit un *state of the art* programme d'acquisition de données. Les assistants techniques du groupe, Paul-Emile Bisson, Gaby Bosch, et Arthur Stettler m'ont aidé à développer, modifier, et tester de l'instrumentation. Sans la bonne volonté et les compétences de toute l'équipe de l'atelier de mécanique, il aurait été beaucoup plus difficile de développer quoi que ce soit en physique expérimentale à Genève. L'équipe de Spyros Zanos m'a fourni de l'hélium liquide indispensable à mes expériences.

Je remercie également toutes les autres personnes qui ont contribué directement ou indirectement à mon travail de thèse. Il s'agit notament de Mesdames les secrétaires et beaucoup d'autres habitants de l'Ecole de physique, que je m'abstiens de mentionner explicitement par peur d'oublier quelqu'un.

Une personne que je tiens à remercier encore en particulier est Hao Tjeng. Pendant mon travail de diplôme à Groningen il m'a montré l'enthousiasme et l'esprit critique qu'il faut pour la recherche, et est ainsi pour une bonne partie responsable de ma décision de commencer le doctorat.

Finalement, j'exprime ma reconnaissance à mes parents pour leur soutien tout au long de mes études, et à Arturo et Marilena pour m'avoir donné le sentiment d'avoir une vraie famille en Suisse aussi. E per Emilie: mi mancano le parole per spiegarti come sei stata importante per me durante gli ùltimi anni, e come lo sei ancora.

Ce travail a bénéficié en partie du soutien financier du Fonds national suisse de la recherche scientifique.

List of Publications

- ⋆ B. W. Hoogenboom, C. Berthod, M. Peter, Ø. Fischer, and A. A. Kordyuk, *Modeling Scanning Tunneling Spectra of $Bi_2Sr_2CaCu_2O_{8+\delta}$*, in preparation.
- ⋆ B. W. Hoogenboom, K. Kadowaki, B. Revaz, and Ø. Fischer, *Homogeneous Samples of $Bi_2Sr_2CaCu_2O_{8+\delta}$*, in preparation.
- ⋆ B. W. Hoogenboom, Ch. Renner, I. Maggio-Aprile, and Ø. Fischer, in *Vortices in Unconventional Superconductors and Superfluids*, Vol. 132 of *Series in Solid-State Science*, edited by R. P. Huebener, N. Schophohl, and G. E. Volovik (Springer, Berlin Heidelberg, 2002), pp. 269–282.
- ⋆ B. W. Hoogenboom, K. Kadowaki, B. Revaz, M. Li, Ch. Renner, and Ø. Fischer, *Linear and Field-Independent Relation between Vortex Core State Energy and Gap in $Bi_2Sr_2CaCu_2O_{8+\delta}$*, Phys. Rev. Lett. **87**, 267001 (2001).
- ⋆ B. W. Hoogenboom, M. Kugler, B. Revaz, I. Maggio-Aprile, Ø. Fischer, and Ch. Renner, *Shape and Motion of Vortex Cores in $Bi_2Sr_2CaCu_2O_{8+\delta}$*, Phys. Rev. B **62**, 9179 (2000).
- ⋆ B. W. Hoogenboom, Ch. Renner, B. Revaz, I. Maggio-Aprile, and Ø. Fischer, *Low-Energy Structures in Vortex Core Tunneling Spectra in $Bi_2Sr_2CaCu_2O_{8+\delta}$*, Physica C **332**, 440 (2000), proceedings of the First Euroconference on Vortex Matter in Superconductors at Extreme Scales and Conditions, Crete, September 1999.
- ⋆ C. Neumann, B. W. Hoogenboom, A. Rogalev, and J. B. Goedkoop, *Crystal Field Effects in the L_{23} XMCD of Rare Earth Insulators*, Solid State Comm. **110**, 375 (1999).
- ⋆ B. W. Hoogenboom, R. Hesper, L. H. Tjeng, and G. A. Sawatzky, *Charge Transfer and Doping-Dependent Hybridization of C_{60} on Noble Metals*, Phys. Rev. B **57**, 11939 (1998).